ELECTRONIC AND OPTOELECTRONIC PROPERTIES OF TWO-DIMENSIONAL TRANSITION METAL DICHALCOGENIDES AND THEIR HETEROSTRUCTURES

WANG SHUNFENG

(B.Eng., HUST)

A THESIS SUBMITTED

FOR THE DEGREE OF DOCTOR OF

PHILOSOPHY

DEPARTMENT OF PHYSICS

NATIONAL UNIVERSITY OF SINGAPORE

2016

DECLARATION

I hereby declare that this thesis is my original work and it has been written by me in its entirety. I have duly acknowledged all the sources of information which have been used in the thesis.

This thesis has also not been submitted for any degree in any university previously.

Wang Shunfeng

____

Wang Shunfeng

6 August 2016

Dedicated to my beloved family

ACKNOWLEDGEMENT

First and foremost, I would like to express my deep gratitude to my supervisor, Asst. Professor Eda Goki for providing me the opportunity and platform to pursue my scientific dreams. Throughout my four years' study, Dr. Eda continuously influenced me with his high-standard altitude towards science. I cannot acknowledge him more for the constant support and patient guidance he offered these years.

I would also like to thank all the seniors and juniors in our group for their company. I would especially like to thank Dr. Zhao Weijie and Mr. Wang Junyong for their useful assistance and intellectual advice. They offered me wonderful consultation on optics, which made my life much easier. Dr. Chu Leiqiang, Dr. Ivan Verzhbitskiy, Dr. Li Shisheng and Mr. Zhang Qi also shared their useful experience with me, which really benefited me a lot. I enjoyed the pleasant memories with these scientists.

My appreciation also goes to the staffs and core members of CA2DM (Center for advanced two dimensional materials). Especially, in the first two years, Mr. Tan Jun You shared with me many valuable experimental techniques. I also had wonderful and exciting discussions with other members, like Dr. Liu Yanpeng, Dr. Li Linjun, Dr. Liu Bo, Dr. Han Cheng, Ms. Wang Zhuo just to name a few.

My heartfelt thanks also go to National University of Singapore and Ministry of Education for providing Research Scholarships and resourceful platforms. I would also like to acknowledge my previous university – Huazhong University of Science and Technology for building my solid

fundamentals. In addition, I enjoyed the joyful activities with my alumni as a core member of HUST Singapore Association.

Eternally, I am grateful to my family for their constant love and physical as well as spiritual supports. Their love is always the source of my power and motivation. I appreciate it that Mom and Dad offer me the freedom to do everything I like.

TABLE OF CONTENTS

DECLARATION ..... **I**

ACKNOWLEDGEMENT ..... **III**

TABLE OF CONTENTS ..... **V**

ABSTRACT ..... **VII**

TABLE OF FIGURES ..... **VIII**

LIST OF ABBREVATIONS ..... **XIX**

1 INTRODUCTION TO TRANSITION METAL DICHALCOGENIDES **1**

1.1 STRUCTURAL, ELECTRONIC AND OPTICAL PROPERTIES OF TMDS 3

1.2 SYNTHESIS AND GROWTH OF TMDS CRYSTALS AND LAYERS 7

1.3 ELECTRICAL TRANSPORT PROPERTIES 10

1.4 LUMINESCENCE IN MONOLAYER TMDS 14

1.5 HETEROSTRUCTURE AND THEIR APPLICATIONS 19

1.6 LIGHT EMITTING DEVICES 32

1.7 SUMMARY 38

2 EFFECT OF OXYGEN AND OZONE ON P-TYPE DOPING OF ULTRA-THIN WSE_2 AND $MOSE_2$ FETS **39**

2.1 INTRODUCTION 39

2.2 METHODS AND EXPERIMENTAL DETAILS 41

2.3 RESULTS AND DISCUSSION 42

2.3.1 Effects of ambient air *42*

2.3.2 Doping effects of ozone *43*

2.3.3 Reversibility of ozone doping *46*

2.3.4 The change of R_c and R_{sh} after ozone treatment *47*

2.3.5 Charge transfer between TMDs and O_3/H_2O redox couple *50*

2.4 CONCLUSION 54

3 PHOTOVOLTAIC EFFECTS IN LAYERED TMDS-BASED HETEROJUNCTIONS 55

3.1 INTRODUCTION 55

3.2 METHODS 58

3.3 RESULTS AND DISCUSSIONS 60

3.3.1 PL mapping of 1L MoS_2-1L WSe_2 heterojunction *60*

3.3.2 "Anti-ambipolar" behavior of hetero-multilayer *61*

3.3.3 Hetero-multilayer solar cell with a modified structure *64*

3.4 CONCLUSION 73

4 HIGHLY EFFICIENT ELECTROLUMINESCENCE FROM ULTRATHIN FIELD EMISSION DIODES 74

4.1 INTRODUCTION 74

4.2 MATERIALS AND METHODS 77

4.3 RESULTS AND DISCUSSION 79

4.3.1 Basic electrical and optical characterization *79*

4.3.2 Highly efficient electroluminescence *82*

4.3.3 Impact ionization *87*

4.4 CONCLUSION 92

5 CONCLUSION AND OUTLOOK 93

6 BIBLIOGRAPHY 96

ABSTRACT

Layered transition metal dichalcogenides are a category of semiconductor with layer-dependent electronic structures in the two dimensional limit. The reduced dimension and dielectric screening strongly enhance the Coulomb interaction, leading to pronounced excitonic effects in the direct band gap monolayers. However, the atomic thickness has rendered the thin layers sensitive to extrinsic circumstance, such as substrate and air.

We first investigated the effect of air to the performance of WSe_2 transistors and explored the feasibility of efficient P-doping by the adsorption of ozone. The layer-dependent band structures together with the diversity of different chalcogenides provide more possibility to create structures with desirable properties by hetero-stacking. In our work, we took advantage of type II band alignment between MoS_2 and WSe_2 and fabricated heterojunctions showing excellent rectification and solar energy conversion efficiency. Given the remarkable excitonic effects in monolayers, we further designed a light emitting WS_2/BN/Graphite hetero-structure with high quantum efficiency, where the injection of carriers are realized by tunneling. Our results support that two dimensional TMDs are of great potential for future electronics and optoelectronics.

TABLE OF FIGURES

Figure 1.1 (a) Schematics of crystal structure of 2H phase transition metal dischalcogenides. Atoms in monolayer arrange in the trigonal prismatic coordination and layers stack in the order of hexagonal symmetry.[7] (b) Calculated band structure of MoS_2 evolving with different thickness. The band gap changes from indirect in bulk to direct in monolayer. {Splendiani, 2010 #419} (c) Photoluminescence spectrum of monolayer and bilayer MoS_2. The PL intensity of monolayer is much higher than that of bilayer. The inset shows the PL quantum yield as a function of layer number. (d) Peak frequency of A_{1g} and E_{2g} as a function of layer thickness in MoS_2. As the layer number increases, peak frequency of A_{1g} blue shifts, while that of E_{2g} red shifts.........3

Figure 1.2 (a) Schematic depiction of the experimental setup of chemical vapor transport method. Transport agents evaporate at the high temperature end (T2) and carry the precursors to the low temperature end (T1). (b) Single crystal of molybdenum disulfide (MoS_2) - Large 15x20mm, grown by "2D Semiconductors"..7

Figure 1.3 (a) Optical image of a CVD-grown triangular monolayer MoS_2 flake grown by using ultra clean substrate and fresh precursors. The triangle is 120um in length from tip to tip.[22] (b) color plot of sheet conductance as a function of gate voltage and temperature, indicating transition from insulating phase to metallic phase at high gate voltage.[23] (c) electron mobility as a function of gate voltage at different temperatures.[23] 8

Figure 1.4 (a) Temperature-dependent mobility in multilayer MoS_2. Four carrier scattering have been considered: homopolar phonon scattering, polar optical phonon scattering, charged impurities scattering and transverse and longitudinal acoustic phonon scattering. (b) Monolayer MoS_2 transistor covered with ALD-deposited HfO_2 and top gate. Room temperature back gate sweep at a fixed bias (V_{ds}=10mV and top gate electrode is disconnected). [38]. 11

Figure 1.5 (a) temperature dependence of electron mobility in BN encapsulated MoS_2 with layer number from 1L to 6L. The inset is a 3D drawing of the as-prepared device. (b) Calculated mobility as a function of presumed carrier density with a decent model considering impurities and short-range scattering centers at the interface. The filled circles are experimentally collected data.[42] 12

Figure 1.6 (a) Relative external quantum efficiency and internal quantum efficiency in monolayer MoS_2 as a function of generation rate under different temperatures. (b) temperature-dependent PL spectra of monolayer WSe_2. (c) Comparison of normalized PL intensity in 1L MoS_2 and WSe_2 as a function of temperature. 15

Figure 1.7 (a) Photoluminescence spectrum at room temperature with back gate varying form -70V to 80V. (b) The formation of a negative (positive) trion when neutral exciton binds an extra electron (hole). (c) Gate dependent photoluminescence in monolayer $MoSe_2$ at 30K. (d) Emission intensity of neutral exciton and trion at various gate voltages........ 17

Figure 1.8 (a) J-V characteristic curve of MoS2/P-Si hetero-structure under illumination. The inset shows the band alignment between monolayer MoS_2

and P-Si based on UPS analysis.[50] With a proper light shining on the device, photo-generated holes in MoS_2 would shift to lower energy band in P-Si. Likewise, electrons in P-Si would flow to the conduction band of MoS_2, which builds a potential across the interface. (b) J-V characteristic curve of solar cell with and without a SiO_2 buffer layer under illumination of 15mW cm^{-2}.the inset plots out a simple band diagram of MoS_2/SiO_2/p-Si. 20

Figure 1.9 (a) Theoretical calculated band diagrams of monolayer TMDs. Solid lines are obtained by PBE, and dashed lines are obtained by HSE06.[52] (b) Band diagram of monolayer MoS_2 and WSe_2 on HOPG determined by STS. The valence band offset is determined to be 0.83eV.[53] (c) optical images of a large area MoS_2-WS_2 hetero-structure, prepared by PDMS-based wet transfer of CVD-grown WS_2 and MoS_2. The scale bar is 10um.[54] (d) i Schematic illustration of charge transfer between MoS_2 and WS_2 and Photoluminescence quench in the heterostructure. When the A-exciton of MoS_2 is optically excited, the holes in MoS_2 would transfer to WS_2 due to the valence band offset. ii transient absorption spectra for MoS_2-WS_2 heterostructure and isolated MoS_2 at 77K as a function of pump-probe delay time. Positive value means pump induced decrease of absorption. iii transient absorption spectra at a delay time of 1ps and 20ps for MoS_2-WS_2 heterostructure and isolated MoS_2. iv linear absorption of MoS_2 and WS_2 respectively.[55] (e) Photoluminescence of WS_2-MoS_2 heterostructure in response to thermal annealing. Both emission peak and emission intensity evolves with annealing duration.[54] (f) Atomistic illustration of MoS_2/NL-hBN/WSe_2 heterostructure. The interlayer transition between MoS_2 and WSe_2 changes with the layer number of intercalated hBN.[56] 22

Figure 1.10 (a) Optical image of 1L MoS_2/WSe_2 device with source drain contact. (b) Energy band profile in the lateral direction from electrostatic simulation. MoS_2 and WSe_2 forms a staggered gap. Electrons and holes are separated by the large band offset. (c) Photocurrent mapping under 532nm laser excitation on the same device as (a). The overlapping junction area shows the highest photo response. (d) IV characteristics as a function of gate voltage. The inset shows the transfer curves of isolated MoS_2 and WS_2 FET plotted in the same frame. (e) J-V characteristic curve under illumination as a function of gate voltage. [58] 27

Figure 1.11 (a) Optical image of PN diode consisting of N-type multilayer MoS_2 and P-type monolayer WSe_2. (b) False color of electroluminescence image from the same device as (a). The emission is localized at the overlapping area close to the electrode. (c) Spectra of electroluminescence as a function of current.[60] 28

Figure 1.12 (a) Schematic of the dual-gated tunnel diode. (b) NDR at a fixed $V_{gate-MoS2}$ and varying $V_{gate-WSe2}$. (c) Band alignment at the NDR peak and valley. 30

Figure 1.13 Transistor (a) and PN diode (b) made up of all two dimensional layered materials.[62] 31

Figure 1.14 (a) absorption, EL and PL spectra from the same 1L MoS_2 device in one X axis. The inset indicates the false color image of electroluminescence in the Schottky diode around the junction area. [64] (b) EL spectrum acquired under a forward bias of 15V and a current of 1.8uA. Three emission peaks (A exciton, B exciton and A^- trion) are labelled by a multiple peak Lorentzian

fitting. The insets present the false color image of EL and band alignment under positive bias.[66] 33

Figure 1.15 (a) schematic of electroluminescence in bipolar WS_2 transistor. (b) Optical image of WS_2 device under a bias of 2.9V (V_g=0.1V). The red dot indicates strong light emission. (c) Comparison of normalized EL and PL spectra of WS_2 transistor.[69] (d) Schematic of electroluminescence in local gated WSe_2 PN junction. (e) Optical image, (f) PL mapping and (g) PL peak energy mapping of the local gated WSe_2 junction. (h) Comparison of normalized EL and PL of WSe_2 PN junction. (i) Optical image of light emission, superimposed on the image of the device.[70] 35

Figure 1.16 (a) schematic and (b) optical image of a single quantum well device. (c) Illustration of carrier distribution and working mechanism of QW device. (d) Optical image of an electrical excited quantum well under sufficient bias. (e) PL spectra and (f) EL spectra as a function of bias. The white line demonstrates the current-voltage characteristic. 37

Figure 2.1 $I_{ds} – V_{gs}$ relationships of (a) monolayer WSe_2, (b) bilayer WSe_2 and multilayer WSe_2 after thermal annealing in N_2 filled glovebox at different temperatures. 43

Figure 2.2 (a) Schematic diagram of WSe_2 transistor exposed to a mixture of oxygen and ozone molecules. (b) Conductance of a bilayer WSe_2 device at V_g = -80 V as a function of air and ozone exposure time. (c-e) Transfer (upper panels) and output (lower panels) curves of a bilayer WSe_2 device in its intrinsic state (c), after air exposure for 12 hours (d), and after subsequent ozone exposure for 11 minutes (e). 44

Figure 2.3 (a) Transfer curve of monolayer WSe_2 before and after step by step ozone exposure. At each exposure step, the device was illuminated with UV light for 1 minute and left in the chamber for 10 minutes to allow ozone molecules to adsorb on the surface. Transfer curves of monolayer (b) and multilayer (c) $MoSe_2$ before and after ozone exposure. 45

Figure 2.4 Photoluminescence (PL) of monolayer WSe_2 after air exposure for several days (a) and after subsequent ozone exposure for 11 mins (b). The spectra were fitted with exciton, trion and localized states emission peaks. The spectra were obtained in nitrogen atmosphere at liquid nitrogen temperature (77K). 46

Figure 2.5 On-state conductance of a bilayer device at V_g = -100 V after exposure to ozone and annealing over multiple cycles. The device shows consistent undoped and doped conductance of ~2 μS and ~40 μS, respectively. 47

Figure 2.6 (a,b) Total resistance of multilayer WSe_2 devices as a function of channel length at different gate voltages before (a) and after (b) ozone exposure. The insets show output curves at gate voltages ranging between -60 and -100 V in 10 V steps. (c,d) Extracted values of (c) R_c and (d) ρ_{sh} as a function of gate voltages for deivces before and after ozone exposure. The dashed line in (c) is a fit according to Eq (1). (e) Schematic band diagram of WSe_2 transistor with Pd source and drain contacts. The dashed line indicates the Fermi level (E_F). In a weakly doped device, current injection is limited by the Schottky barrier at the contact. After doping, the Schottky barrier becomes narrower and thermionic tunneling of holes is facilitated. 49

Figure 2.7 (a) Schematic showing the scheme for studying the role of water in oxygen and ozone doping. The water adlayer was removed by annealing the device enclosed in a quartz tube and cooling it over a temperature gradient to condense moisture on the inner walls of the quartz. Ozone is subsequently introduced by UV light exposure. (b) Transfer characteristics of the device in the conditions as illustrated in (a). (c) Schematic energy diagram showing the DOS of WSe_2 (left) relative to that of O_3/H_2O (or O_2/H_2O) redox system (right). Electrons transfer from WSe_2 to the redox system driven by the difference in E_F and E_{redox}. 52

Figure 3.1 (a) Schematic of a multilayer WSe_2-MoS_2 heterojunction; (b) optical image of an hBN encapsulated WSe_2-MoS_2 heterojunction; WSe_2 flake is highlighted with the dark blue line, while the violet line indicates the position of MoS_2 flakes. The entire junction is encapsulated with hBN marked by the light blue line. The scale bar is 10um. 58

Figure 3.2 (a) PL mapping of a 1L MoS_2-1L WSe_2 heterojunction excited by a 473nm laser. The inset shows the optical image of the device. 1L MoS_2 and 1L WSe_2 are marked by the violet and blue line, respectively. (b) PL spectrum at the interface of heterojunction. Two main peaks are ascribed to exciton emission of single WSe_2 and MoS_2, a lower energy peak is probably due to indirect transition of majorities in separate layers. The inset shows the typical photo-generated carrier transfer process in a type II heterojunction. 61

Figure 3.3 (a) Transfer curves of single MoS_2 transistor (blue), single WSe_2 transistor (red) and the MoS_2-WSe_2 heterojunction (black). V_{ds} is fixed at 1V. (b) Illustration of a Nn zone and np zone based on the interpretation of gate

dependence. (c) I_{ds}-V_{ds} under different gate voltages in the dark. (d) Photovoltaic effect of the hetero-multilayer as a function of gate voltage under the excitation with a 5μW green laser. 62

Figure 3.4 (a) the red frame highlights the gate-dependent resistance which limits the current density of the heterojunction (b) Modification of device structure. A thick layer of MoS_2 is utilized to contact the bilayer MoS_2. (c) Optical image of a heterojunction with the modified structure. 64

Figure 3.5 (a) $I_{ds} - V_{gs}$ relationship (V_{ds} = 1V). The ambipolar-like gate dependence demonstrates the formation of nn and pn junction at different gate voltages. (b) IV curve at the pn regime with a gate voltage ranging from -60V to -100V. (c) IV curve at the nn regime with a gate voltage ranging from 0V to -60V. 66

Figure 3.6 (a) IV curves of the device at a gate voltage of -100V in the dark and under illumination. The excitation power is 7.9μW. The inset shows the P_{el} as a function of V_{ds}. (b) Photo response as different excitation powers when the device is negatively biased. The inset plots out the relationship of photocurrent as a function of incident power. 68

Figure 3.7 (a) Short circuit current and (b) open circuit voltage as a function of incident power. (c) P_{el} as a function of V_{ds} under different excitation power. (d) Power conversion efficiency (PCE) as a function of P_{in}. The inset shows the FF as a function of P_{in} 69

Figure 3.8 (a) IV characteristics at different gate voltages with the excitation of a 665μW green laser. The inset shows the zoom-in picture around the

original point. (b) Filling factor as a function of gate voltage. (c) Shunt resistance of the hetero-multilayer as a function of gate voltage under different excitation power. The inset shows that R_{sh} decreases with increasing P_{in}. (d) Series resistance as a function of gate voltage under the excitation of 665μW green laser. 71

Figure 4.1 (a) Schematic view of FLG/hBN/WS_2 light emitting diode. (b) I_d-V_d characteristic at V_g = 40 V. The inset shows the plot of tunneling current as a function of V_g and V_d. (c) EL spectra of the MIS diode at different V_d and I_d at 100 K. (d) Bright-field optical image of the device and image of EL at an injection current of 100 nA at an accumulation time of 2 s. The emission area is ~ 66 μm^2. 80

Figure 4.2 (a)Diode current (I_d) vs time (t) plot of a device during increasing steps of applied bias (V_d). The bias was increased from 5.1 V to 6.0 V at 0.1 V step at ~ 20 s interval. EL spectra at different current levels are shown at each step. The background current was ~ 100 pA for this device. EL emerges immediately above the threshold voltage of 5.1 V, at current of ~ 200 pA. The active area of this device is 37 μm^2. (b) EL spectra under different bias. 81

Figure 4.3 Typical transfer characteristics of monolayer WS_2 device at room temperature measured in N_2 atmosphere. 82

Figure 4.4 PLE spectra of a FLG/h-BN/WS_2/SiO_2/Si heterostack. (a) PLE intensity map and (b) relative PLE spectra based on the integrated intensity of the A peak in the PL spectra at each excitation energy; the excitation laser we used (473 nm) has also been labeled in this figure. 83

Figure 4.5 (a) Comparison of EL and PL spectra measured at similar $G_{e\text{-}h}$ at 100 K. EL was collected at $I_d = 0.9$ nA, $V_d = 8.4$ V and $V_g = 80$ V. The device area is 16 μm^2. PL was obtained at excitation energy and power of 2.6 eV and 1.7 nW. PL was measured at $V_g = 80$ V and $V_d = 0$ V. $G_{e\text{-}h}$ for EL and PL are 1.8×10^{16} cm^{-2}s^{-1} and 1.9×10^{16} cm^{-2}s^{-1}, respectively. (b) Comparison of the relative QY of PL and EL over a wide range of electron-hole pair generation rates. S1 and S2 are two different devices measured at 100 K and 77 K, respectively. 84

Figure 4.6 PL and EL intensity as a function of V_g and V_d. Left and middle columns show changes in the integrated PL intensity (upper panel) and color-coded spectrum (lower panel) as a function of V_g at $V_d = 0$ (left column) and as a function of V_d at $V_g = 80$ V (middle column). PL was measured at the excitation energy and power of 2.6 eV and 5μW. X^I and X^- denote emission due to impurities/defects and negative trions, respectively. Right column shows the evolution of EL integrated intensity (upper panel) and spectrum (lower panel) as a function of V_d at $V_g = 0$ V. 85

Figure 4.7 PL spectrum as a function of diode bias voltage. The measurements were made below and above the EL threshold $V_{th} = 6.5$ V. For $V_d > V_{th}$, the spectrum comprises of both the PL and EL signals. Note that there is no evidence of discontinuity in PL QY around V_{th}, indicating that the decay dynamics of ground excitons is neither altered by the diode bias nor current. Note that the PL intensity is greater than the EL intensity due to high optical excitation power (159 W/cm^2) used in this experiment. PL is predominantly

due to negative trions, whereas EL is both due to negative trions as well as impurity emission..86

Figure 4.8 EL spectrum of a device exhibiting peaks due to neutral exciton, negative trion, as well as impurity emission...87

Figure 4.9 (a) Fowler-Nordheim plot of I_d-V_d relationship at temperatures ranging from 77 to 240 K. The turning point in the plot coincides with the threshold voltage (Vth) for light emission. (b) EL spectrum at a high bias voltage ($V_d = 7$ V). A and B denote emission due to A and B excitons arising from spin-orbit-split valence bands as shown in the inset. (c) Band diagram of the FLG/hBN/WS_2 heterostructure for $V_d = 0$ and $V_d > V_{th}$............................89

Figure 4.10 Exciton generation mechanisms in n-type WS_2 monolayer. (a) Generation of a single trion and emission following absorption of a photon having energy slightly greater than the semiconductor band gap. (b) Impact ionization by an energetic electron followed by generation of a single trion. (c) Impact ionization by an energetic hole followed by generation of two trions. 91

LIST OF ABBREVATIONS

1L	Monolayer
2D	Two Dimension(al)
2DEG	Two Dimensional Electron Gas
Au	Gold
CBM	Conduction Band Minimum
Cr	Chromium
CVD	Chemical Vapor deposition
CVT	Chemical Vapor Transport
DOS	Density of States
e-h	electron-hole
EBL	Electron Beam Lithography
EL	Electroluminescence
EQE	External Quantum Efficiency
FET	Field Effect Transistor
FF	Filling Factor
FLG	Few Layer Graphene
F-N	Fowler-Nordheim

hBN	Hexagonal Boron Nitride
H_2O	Water
HfO_2	Hafnium Dioxide
HOPG	Highly Oriented Pyrolytic Graphite
IQE	Internal Quantum Efficiency
LED	Light Emitting Diode(Device)
MBE	Molecular Beam Epitaxy
MIS	Metal Insulator Semiconductor
MIT	Metal Insulator Transition
MoO_3	Molybdenum Trioxide
MoS_2	Molybdenum Disulphide
$MoSe_2$	Molybdenum Diselenide
$MoTe_2$	Molybdenum Ditelluride
MQW	Multiple Quantum Wells
MX_2	Transition Metal Dichalcogenide
NDR	Negative Differential Resistance
NL	Multilayer
O_2	Oxygen
O_3	Ozone
PCE	Power Conversion Efficiency

Pd	Palladium
PL	Photoluminescence
PMMA	Polymethyl Methacrylate
PDMS	Polydimethylsiloxane
QY	Quantum Yield
RT	Room Temperature
Si	Silicon
SiO_2	Silicon Dioxide
TLM	Transfer Length Method
TMDs	Transition Metal Dichalcogenides
UV	Ultraviolet
VBM	Valence Band Maximum
vdW	van der Waals
WS_2	Tungsten Disulphide
WSe_2	Tungsten Diselenide

1 Introduction to Transition Metal Dichalcogenides

As the feature size of integrated circuits scales down according to Moore's law, short channel effects play an increasingly dominant role in limiting device performance. An effective way to reduce the leakage due to extremely short gate length is to thin down the channel body accordingly. Ultrathin body transistor necessitates the fabrication of silicon thin films that are less than 10nm on a SiO_2, which is a great challenge to the present top-down semiconductor process technologies. The discovery of atomically thin semiconductors therefore sparked tremendous interest in the electronics community.

In 2004,[1] the discovery of single monolayer graphene with a thickness of several angstroms sent shock waves throughout the material community. Thanks to its linear electronic spectrum $E = \hbar v_F k$, charge carriers in monolayer graphene, the thinnest and strongest material, exhibit zero effective mass and hence giant intrinsic mobility.[2, 3, 4] On the other hand, desirable attributes for logic circuits include not only high conductivity and carrier mobility for high-speed operation, but also large on-off ratios and low off-current for effective switching and low stand-by power consumption. Graphene and graphene nanoribbons lack a sufficiently large band gap, which results in significant off-state current, limiting its application in digital logic transistors.[4] Therefore, there is an incentive to seek two dimensional materials beyond graphene. In this regards, layered transition metal dichalcogenides (TMDs), particularly those with a sizable band gap, have received significant interest.

Analogous to graphite, transition metal dichalogenides are a group of materials with van der Waals layered structure and strong intralayer covalent bonds. The bulk form of layered TMDs, possessing a variety of electronic and optical properties, have been extensively studied for decades.[5, 6] Recently, the advances of mechanical exfoliation, chemical vapor deposition, optical identification and manipulation techniques developed for graphene research facilitated rapid progress in understanding the physical characteristics of monolayer TMDs. Despite the structural similarity with graphene, semiconducting TMDs possess sizable band gap, which is required for effective switching when used as a channel material of a transistor. Moreover, as the layer number decreases, quantum effects becomes dominant, giving rise to layer-dependent properties.

In this chapter, basic properties of group VI TMDs will be briefly introduced first, followed by deeper reviews on the recent progress of synthesis, electrical and optical properties of monolayers and heterostructures and their potential applications.

1.1 Structural, electronic and optical properties of TMDs

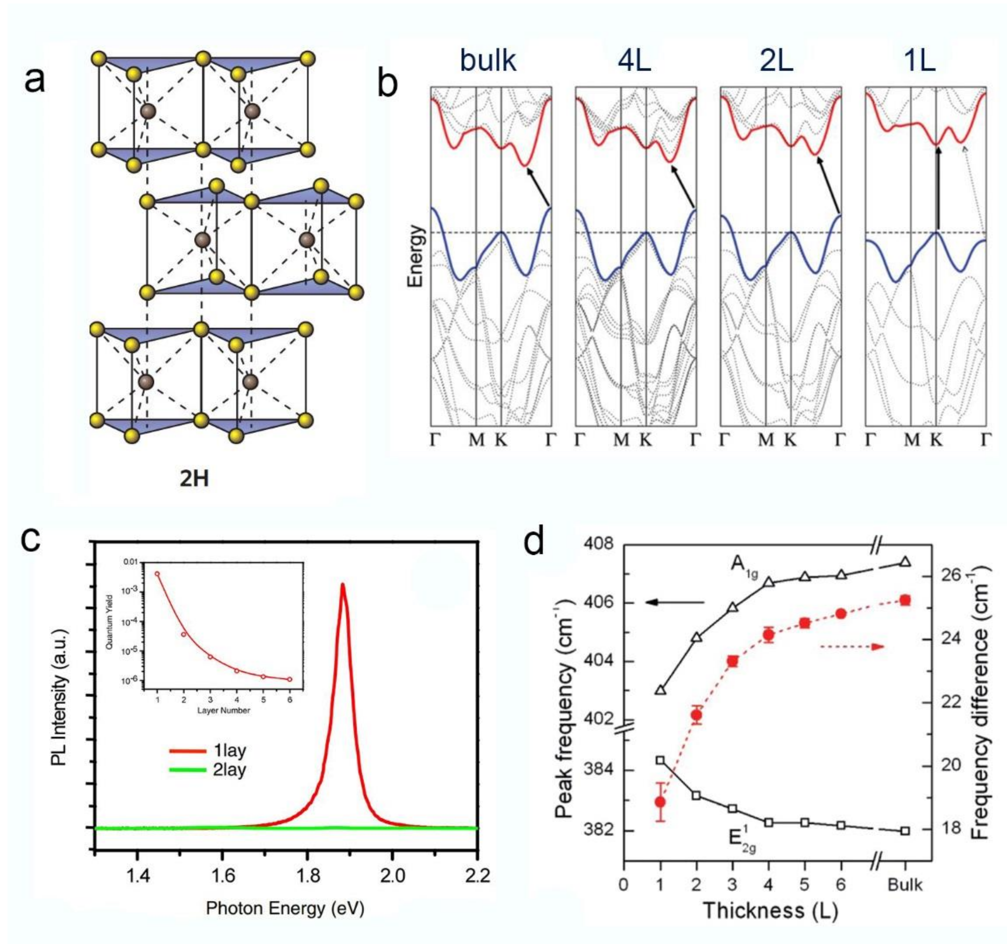

Figure 1.1 (a) Schematics of crystal structure of 2H phase transition metal dischalcogenides. Atoms in monolayer arrange in the trigonal prismatic coordination and layers stack in the order of hexagonal symmetry.[7, 8] (b) Calculated band structure of MoS_2 evolving with different thickness. The band gap changes from indirect in bulk to direct in monolayer.[9] Reprinted with permission from ref 9. (c) Photoluminescence spectrum of monolayer and bilayer MoS_2. The PL intensity of monolayer is much higher than that of bilayer. The inset shows the PL quantum yield as a function of layer number.[10] (d) Peak frequency of A_{1g} and E_{2g} as a function of layer thickness in MoS_2. As the layer number increases, peak frequency of A_{1g} blue shifts, while that of E_{2g} red shifts.[10]

Transition metal dichalcogenides are a group of materials with transition metal (M) and chalcogen (X) forming MX_2. They often exhibit several different phases, depending on the growth condition. Here, we will

focus on the 2H phase compounds containing Mo/W and S/Se, since they are semiconductors and found to be more stable. The layered 2H structure is characterized by the stacking of the fundamental building block in the order of hexagonal symmetry via weak van der Waals force. The thinnest limit, namely monolayer, consists of a hexagonal plane of transition metal atoms, sandwiched by two hexagonal chalcogen atoms via ionic-covalent bonding in trigonal prismatic coordination, as depicted in Fig 1.1 (a). [7]

The 2H phase transition metal dichalcogenides exhibits layer-dependent electronic and optical properties. In general, the band gap increase with the decreasing number of layers due to quantum confinement effects. First-principle calculation predicts that the band gap of MoS_2 changes from an indirect band gap in multilayer to a direct band gap in monolayer, as exhibited in Fig 1.1(b).[11] For indirect band gap, the valence band maximum (VBM) and conduction band minimum (CBM) are located at the Γ point and in between Γ and K point in the Brillouin zone, respectively. Both CBM and VBM of monolayer MoS_2 are located at the K point.[9] According to the projected density of states, states around the Γ point and the CBM can be ascribed to a linear combination of d orbitals on Mo atoms and antibonding p_z orbitals on sulfur atoms.[9] These states are strongly affected by interlayer coupling and quantum confinement. On the other hand, conduction band states at the K point mainly originates from strongly localized d orbitals on molybdenum atoms.[9] Since molybdenum atoms are surrounded by two planes of sulfur, these states are less likely to be layer dependent. Hence, the band gap at K point barely changes with layer number. As the number of layers decrease, the indirect band gap significantly increases due to quantum confinement, while

the direct band gap remains nearly unchanged. At the limit of monolayer, the indirect band gap surpass the direct band gap (E_{indi}>E_{di}), leading to an indirect-direct-gap crossover. Such indirect-direct-gap crossover also occurs other group VI TMDs such as WS_2, WSe_2 and $MoSe_2$[12, 13, 14, 15]

Photoluminescence is a versatile technique to probe the intrinsic electronic properties of a material. Optically excited electron-hole pairs relax through interband recombination process. For indirect transition in TMDs, phonons are needed to compensate the momentum difference of the electrons and the holes and satisfy momentum conservation. Since phonon-mediated emission is a second order process, the QY of the process is typically very low.[9] Therefore, a direct band gap semiconductor is desirable for light emitting devices. It is experimentally shown that the quantum yield of photoluminescence increases by a factor of 10^4, when bulk MoS_2, an indirect band gap semiconductor is thinned down to a monolayer, as shown in Fig 1.1(c).[10] Similar enhancement of photoluminescence has also been observed in WS_2 and WSe_2.[14] The direct band gap of monolayer TMDs makes them attractive for a variety of optoelectronic applications, where the ultrathin body of the active area offers advantages over conventional direct gap materials.

It has been found that vibration modes are also sensitive to the number of layers. In MoS_2, the frequency of two dominant Raman modes, out-of-plane A_{1g} and in-plane E_{2g}, vary with the thickness of the flake. In principle, both E_{2g} and A_{1g} are expected to blue-shift since the interlayer van der Waals interaction enhance the effective restoring forces acting on the atoms as the number of layer increases. However, experimental investigation revealed that in-plane E_{2g} mode unexpectedly blue-shift with decreasing thickness.[16] This

anomalous trend was then clarified by first principle calculations which shows that the absence of adjacent layers enhances surface force constants for Mo-S intra-layer interactions in thin flakes of MoS_2.[17] As a result, the competition between interlayer and intra-layer interaction determines the vibration dynamics of MoS_2 and other layered materials. These layer-dependent lattice dynamics of TMDs in return offer a convenient fingerprint for identifying the number of layer.

1.2 Synthesis and growth of TMDs crystals and layers

MoS_2, the only TMD existing in nature as molybdenite, exhibits a range of unique and attractive electronic properties. Therefore, controllable synthesis of large and high-quality TMDs, including MoS_2, in the form of both single crystal and thin layers is crucial for the implementation of advanced devices.

It is commonly accepted that chemical vapor transport (CVT) allows for the synthesis of high quality crystalline solids[18]. During the process, solid precursors are volatilized and transferred with the assistance of the transport agent and deposited in the lower temperature zone in the form of single crystal, as depicted in Figure 1.2. CVT has been widely used to grow bulk TMDs with desired chemical compositions.

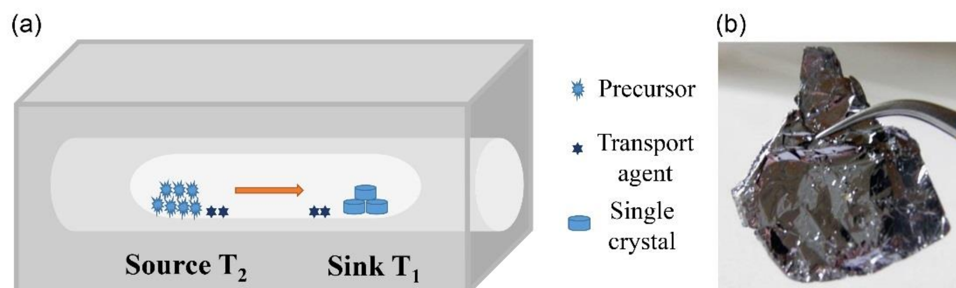

Figure 1.2 (a) Schematic depiction of the experimental setup of chemical vapor transport method. Transport agents evaporate at the high temperature end (T2) and carry the precursors to the low temperature end (T1). (b) Single crystal of molybdenum disulfide (MoS_2) - Large 15x20mm, grown by “2D Semiconductors”.

Mechanical exfoliation of bulk crystal has commonly been recognized as an effective method to produce high quality atomically thin TMDs. The process involves repeated peeling with an adhesive tape. The samples are ideal

for studying fundamental properties of the material. Nevertheless, this top-down approach is not suitable for large-scale and uniform production of thin layers. On the other hand, bottom-up chemical vapor deposition (CVD) and MBE offer a versatile route to achieving wafer-scale TMDs.[19]

There have been attempts to synthesize wafer-scale thin TMDs by simple sulfurization or selenization of Mo/W metal or their oxides[20, 21, 22] Despite its simplicity, the as-prepared TMDs are mostly polycrystalline with small grain sizes, which inhibits fabrication of high-performance devices.

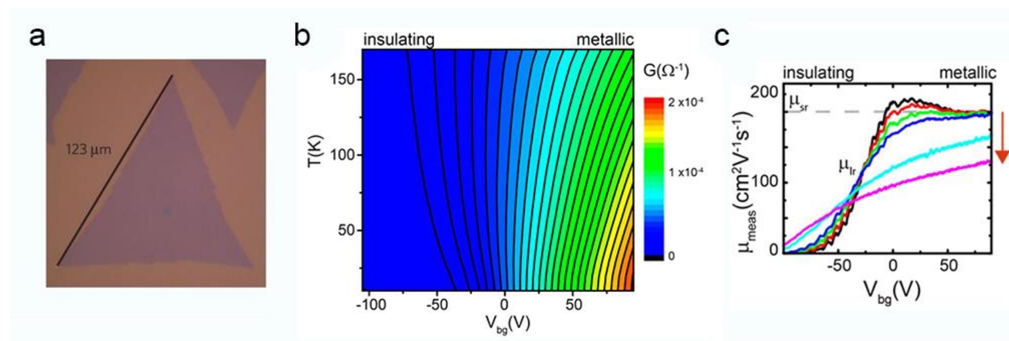

Figure 1.3 (a) Optical image of a CVD-grown triangular monolayer MoS_2 flake grown by using ultra clean substrate and fresh precursors. The triangle is 120um in length from tip to tip.[23] (b) color plot of sheet conductance as a function of gate voltage and temperature, indicating transition from insulating phase to metallic phase at high gate voltage.[24] (c) electron mobility as a function of gate voltage at different temperatures.[24] Reprinted with permission from ref 24.

Chemical vapor deposition (CVD), based on vapor phase reaction of MoO_3 and S powders, allows growth of MoS_2 monolayers with large grain sizes (1~100um) on arbitrary substrates via the proper control of nucleation density. There has been many efforts in growing MoS_2,[25, 26] WS_2[27, 28], $MoSe_2$[29] and WSe_2[30, 31] through CVD. Van der Zande[23] showed that large single

crystalline MoS_2 monolayer up to 120um in lateral size could be produced by using ultra-clean substrates and minimizing the exposure of fresh precursors to air, as shown in Figure 1.3(a).

In our recent work,[24] our research group succeeded in growing large triangles of MoS_2 and found that the electronic transport properties of CVD-grown MoS_2 could be comparable to that of as-exfoliated samples. Electron mobilities at low temperature reaches up to 500 $cm^2/V{\cdot}s$, and the devices exhibit band transport at high doping regime, as shown in Figure 1.3(b) and (c). Besides CVD, direct evaporation of MoS_2 powder has also been reported to be effective in the growing of high-quality trigonal monolayer MoS_2 on a variety of standard insulating substrates.[32]

1.3 Electrical transport properties

Conventional 2D electron gas (2DEG) forms at the interface between bulk semiconductors, whereas 2D materials offers a natural dwelling for 2D electron gas. There have been extensive investigations on the two dimensional electronic transport properties of monolayer and few-layer TMDs on an insulating surface.

According to quantum transport simulation, [33] an ideal monolayer MoS_2 transistor is predicted to exhibit on-off ratio up to 10^{10} , outstanding short channel behavior (drain induced barrier lowering ~ 10mV/V) and efficient switching (subthreshold swing ~ 60mV/decade) . Recent demonstration of integrated circuits based on monolayer[34] and bilayer[35] MoS_2 and high-gain inverter based on WSe_2[36] highlight that they are competent candidates for next generation electronics.

On the other hand, carrier mobility of TMDs at room temperature, a key figure of merit for field effect transistors, is greatly limited by electron-phonon interaction at room temperature. According to first principle calculations,[37] phonon scattering limits the room temperature mobility of monolayer MoS_2 to ~ 410 $cm^2V^{-1}S^{-1}$, whilst at low temperatures the mobility increases with decreasing temperature following $\mu = T^{-1.69}$. Besides electron-phonon interaction, Coulomb scattering by charged impurities, defects and roughness also has strong impact on the carrier mobility particularly especially for monolayer materials.

S. Kim et al[38] introduced the semi-classical Boltzmann transport equation under the relaxation time approximation to estimate the T-

dependence of electron mobility of few-layer MoS_2, as shown in Figure 1.4(a). Fitting analysis reveals that the mobility is dominated by charged impurity scattering at low temperatures, while phonon scattering dominates at high temperature and limits the carrier mobility.

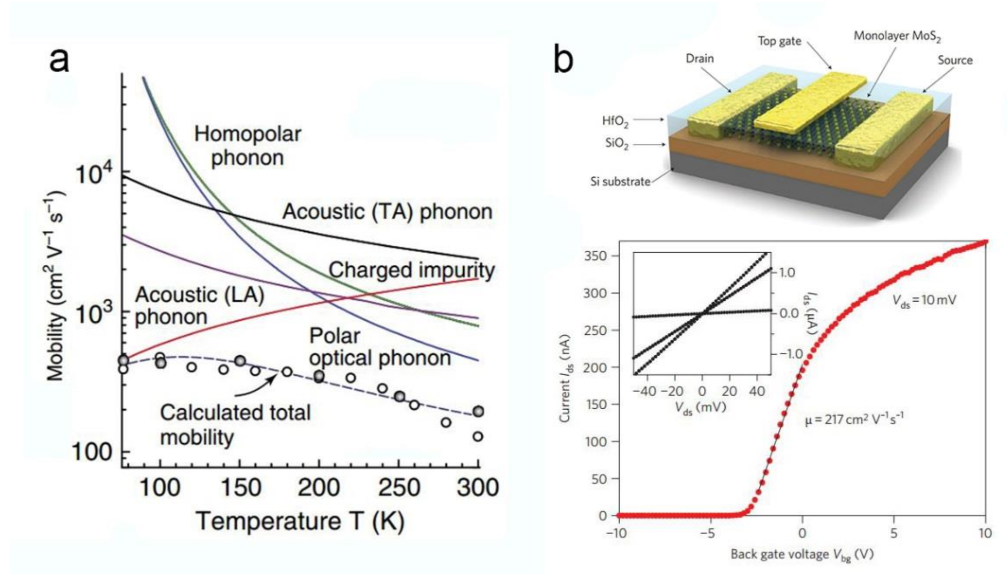

Figure 1.4 (a) Temperature-dependent mobility in multilayer MoS_2. Four carrier scattering have been considered: homopolar phonon scattering, polar optical phonon scattering, charged impurities scattering and transverse and longitudinal acoustic phonon scattering.[38] (b) Monolayer MoS_2 transistor covered with ALD-deposited HfO_2 and top gate. Room temperature back gate sweep at a fixed bias (V_{ds}=10mV and top gate electrode is disconnected). [39]

While the general trends of temperature-dependent carrier mobility is understood, experiments show that device mobility still falls far short of theoretical predications. It is reported that a high-K dielectric interfaced with a 2D semiconductors dampens the out-of-plane phonon vibrations of MX_2 and therefore improves phonon-limited mobility.[38] Also, high-K dielectric is both theoretically and experimentally found to be able to suppress Coulomb scattering induced by charged impurities. [39, 40] A field effect mobility of around 200 $cm^2V^{-1}s^{-1}$ was obtained in dual-gated transistor with high-K top

gate, which is much higher than the values measured for devices having ordinary dielectric materials [39, 41]. Large mobilities were also measured in dual-gated monolayer WSe_2.[42] However, the experimentally measured field effect mobility at present is still far below phonon scattering limited value. This suggests that defects and impurities severely limit carrier transport in 2D systems.

One way to circumvent the effects of impurities and band edge disorder is high carrier density doping. We showed that MoS_2 is intrinsically N-doped in Figure 1.3. The devices exhibits high electron mobility at low temperature and a signature of insulator-metal crossover when sufficient amount of carriers are injected electrostatically and sources of hole-dopant are driven away by annealing[24].

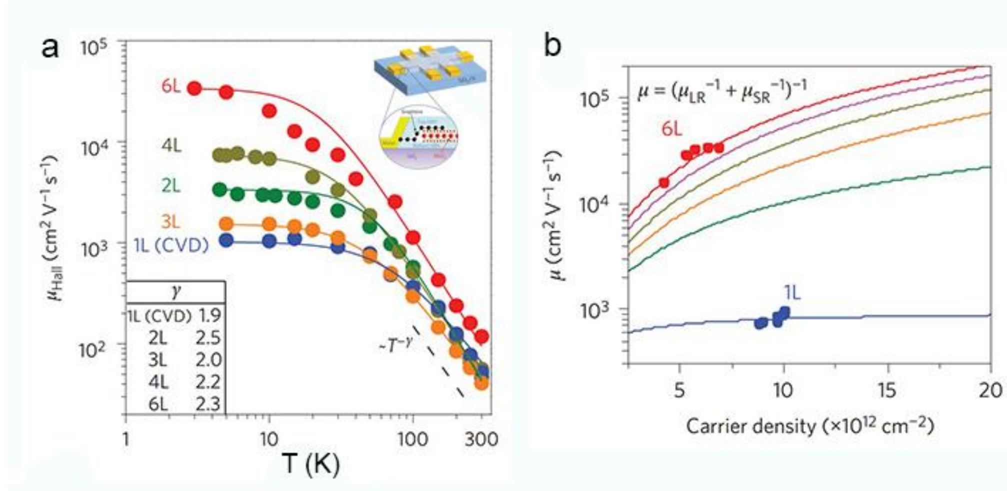

Figure 1.5 (a) temperature dependence of electron mobility in BN encapsulated MoS_2 with layer number from 1L to 6L. The inset is a 3D drawing of the as-prepared device. (b) Calculated mobility as a function of presumed carrier density with a decent model considering impurities and short-range scattering centers at the interface. The filled circles are experimentally collected data.[43]

Recently, Cui et al succeeded in further improving mobility by encapsulating MoS_2 with atomically flat hexagonal boron nitride layers hBN, as shown in Figure 1.5.[43] The large enhancement implies that degrading effects introduced by SiO_2 substrate can be nullified by the hBN layers. Meanwhile, carrier density and temperature scaling behavior shown in Figure 1.5(b) reveals that interfacial impurities and short range scatterers are responsible for the large difference in mobility between monolayer and multilayer samples. S. Xu et al, demonstrated that electron and hole mobilities of WSe_2 can also be improved with the same approach.[44]

The insight into scattering mechanism not only sheds clear light upon inherent electronic properties of TMDs, but also highlights ways by which mobilities can be further improved.

1.4 Luminescence in monolayer TMDs

To understand light emission from 2D materials, it is necessary to have an insight into excitonic effects that dominate the optical properties of these materials. The excitons are strongly bound and exhibit Bohr radius that is nearly equal to its thickness.[45] An exciton is an electrically neutral quasi-particle composed of an electron-hole pair bonded by electrostatic Coulomb force. In the 2D materials, Coulomb interaction is dramatically enhanced due to the spatial quantum confinement of charge carriers. Further, reduced dielectric screening and large effective mass in a monolayer also enhance Coulomb interaction, resulting in large exciton binding energies ranging from 0.32 to 0.7eV, which is one order of magnitude higher than those of conventional group III-V compounds. [46] Pronounced excitonic effects in monolayers can be experimentally observed at room temperature because the exciton binding energy is significantly larger than the thermal fluctuations.

Salehzadeh et al. reported that strong Coulomb interactions in monolayers leads to enhanced non-radiative and radiative recombination rates that are nearly 6 and 3 orders higher than those of bulk semiconductors, respectively.[47] Figure 1.6 (a) illustrate the relative EQE and IQE of A excitons in 1L MoS_2 as a function of generation rate (G) at different temperatures. In general, there are two dominating non-radiative recombination, namely Shockley-Read-Hall (SRH) recombination and Auger recombination. It is claimed that the saturation of SRH recombination gives rise to an increase of quantum efficiency at lower carrier injection, while the efficiency droop at higher generation rate reflects the enhanced indirect Auger recombination, which is considered as the main limiting factor in GaN LEDs. This suggests

that better quantum efficiency could be realized at extremely low carrier injection. Recently, Ali Javey's group showed that an appropriate chemical treatment could eliminate defect-mediated non-radiative recombination and lead to a near unity quantum yield at low generation rate.[48]

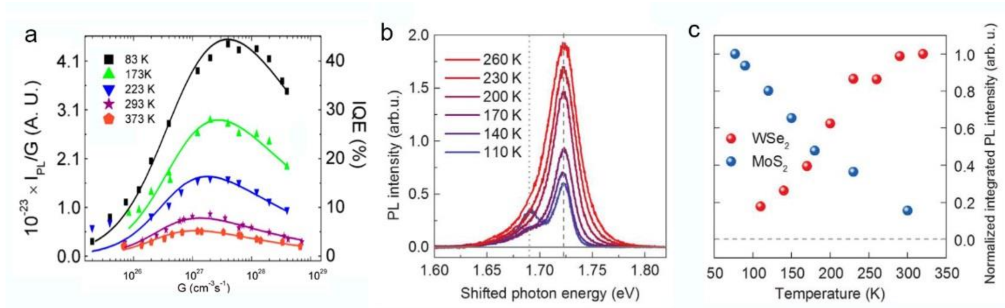

Figure 1.6 (a) Relative external quantum efficiency and internal quantum efficiency in monolayer MoS_2 as a function of generation rate under different temperatures. Reprinted with permission from ref 47. (b) temperature-dependent PL spectra of monolayer WSe_2. (c) Comparison of normalized PL intensity in 1L MoS_2 and WSe_2 as a function of temperature.

In addition, Figure 1.6 (a) shows that the PL intensity of monolayer MoS_2 increases steadily with temperature, which is believed to result from exciton dissociation. However, the temperature dependence seems to be inconsistent in other TMD monolayers. For instance, Figure 1.6(b) shows an opposite trend in monolayer WSe_2, as interpreted from the negative T-dependent PL intensity.[49] It is explained that the existence of optically dark ground excitonic states results in lower PL QY at low temperature.

Besides the generation rate and temperature dependence, the gate dependence of PL spectrum in monolayer MoX_2 also offers rich information on the electronic properties of the material. As shown in Figure 1.7 (a),[50] The changes in PL intensity of monolayer MoS_2 as a function of gate voltage reflects that carrier density strongly influences the quantum yield. In addition, A emission peak emerges at lower energy when electron density is increased.

The new peak is ascribed to the radiative recombination of negative trions, labelled as A^-.

Figure 1.7(b) presents the generation of a negative (positive) trion. When a neutral exciton binds with an extra electron (hole), it forms a charged quasiparticle labelled as a trion.[51] Similar to neutral exciton, the trion has a ground singlet state and a triplet state, but with spin equal to 1/2 and 3/2. The intriguing half integer spin value opens the door to new phenomena. In conventional semiconductors, it is difficult to observe trions, because of their small binding energy. However, the trions of TMDs are stable even at room temperature due to enhanced Coulomb interaction and its large effective mass in monolayer.

In the case of MoS_2, at low carrier densities (V_{gs} = -70V), neutral excitons dominate the PL spectrum. An increase of electron density facilitates the exchange of exciton into trion. Therefore, as the gate voltage increases, the PL spectra gradually evolves from exciton-dominant strong emission to trion-dominant weak emission. In principle, the total intensity should be conversed. However, the trion emission is much weaker than exciton emission and demonstrates no clear increase with electron density. This might be ascribed to the thermal dissociation of trion at room temperature, since thermal energy at 300K is 26meV, a little bit higher than the trion binding energy of monolayer MoS_2. To conclude, it is possible to tune the ratio of neutral and charged excitons via electrostatic gating.

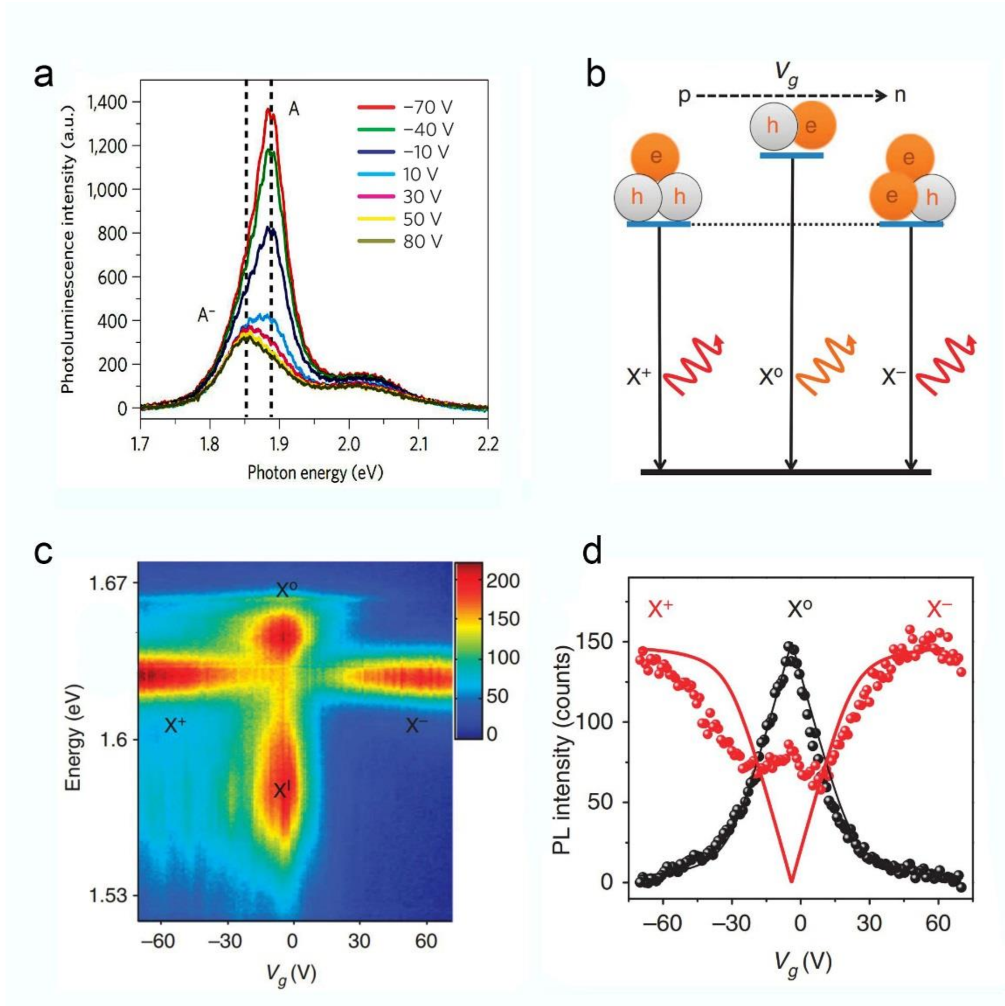

Figure 1.7 (a) Photoluminescence spectrum at room temperature with back gate varying form -70V to 80V. (b) The formation of a negative (positive) trion when neutral exciton binds an extra electron (hole). (c) Gate dependent photoluminescence in monolayer $MoSe_2$ at 30K. (d) Emission intensity of neutral exciton and trion at various gate voltages.

Ross et al[51] have also experimentally investigated the charging effects of exciton in monolayer molybdenum disulfide at low temperature via photoluminescence. The reversible tunability of charging was achieved by electrostatic gating in a back-gated $MoSe_2$ transistor. Gate dependence photoluminescence of monolayer $MoSe_2$ at 30K is illustrated in Figure 1.7(c). As can be seen, emission peaks of neutral excitons and impurity bound excitons appear at zero gate, indicating electrical neutrality. When a gate

voltage with either sign is applied, the strong emission of both neutral exciton and impurity-bound excitons are quenched and a trion emission peak emerges. The intensity of exciton and trion emission is summarized as a function of gate voltage in Figure 1.7 (d). In contrast to the case of MoS_2 at room temperature, the total emission intensity is nearly conserved at all gate voltages. As the gate voltage controls the distribution of carriers in $MoSe_2$, the accumulation of electrons (holes) facilitate the binding of electrons (holes) to neutral exciton and form negative (positive) exciton, while total amount of emission does not change with gate. The investigation on gate-dependent PL reveals the dynamics of many-body particles and provides useful guide to the electronic properties of the.

1.5 Heterostructure and their applications

Operation mechanism of semiconductor devices typically rely on effects that occur at interfaces and junctions. For instance, a p-n junction is a fundamental building block for diodes and photovoltaic cells. These devices rely on the built-in electrical field at the junction. The conventional semiconductor technology offers two common approaches to the creation of an interface with large built-in field: making homo-junction with separate N-type and P-type region by sequential doping or building heterostructure with desirable band structure. However, the former approach is not viable for 2D TMD materials. It is difficult to achieve adequate and stable doping without harming the intrinsic properties. Presently, techniques to substitutionally dope MX2 with spatial control is lacking. This makes fabrication of conventional PN junction using existing approach challenging. On the other hand, atomically flat van der Waals surface of 2D materials allows fabrication of heterojunctions significantly more versatile. This is because 2D materials form electronically coupled junctions without lattice matching requirements. The large family of layered TMDs offers numerous choices of materials to realize desired electronic heterojunctions.

Tsai et al[52] have made use of p-doped silicon to form a PN junction with N-type monolayer MoS_2. The authors utilized ultraviolet photoemission spectroscopy (UPS) to investigate the work function and energy difference of P-Si and monolayer MoS_2. The corresponding band diagram is shown in the inset of Figure 1.8(a). As can be seen, monolayer MoS_2 formed a staggered type II gap with P-Si. The J-V curve is shown in Figure 1.8(a) with an open circuit voltage above 0.4V, giving a power conservation efficiency of 5.23%.

Further, it is found that insertion of a thin buffer layer between Si and MoS_2 could improve the open-circuit voltage and thus power conversion efficiency.[53] The authors speculate that the insulating SiO_2 layer inhibits carrier recombination at the interface and at the same time effectively enhance the built-in field.

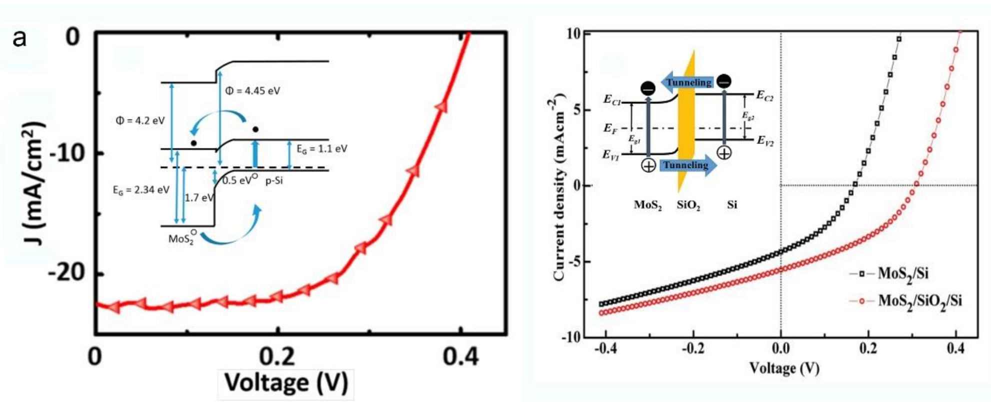

Figure 1.8 (a) J-V characteristic curve of MoS2/P-Si hetero-structure under illumination. The inset shows the band alignment between monolayer MoS_2 and P-Si based on UPS analysis.[52] With a proper light shining on the device, photo-generated holes in MoS_2 would shift to lower energy band in P-Si. Likewise, electrons in P-Si would flow to the conduction band of MoS_2, which builds a potential across the interface. Reprinted with permission from ref 52. (b) J-V characteristic curve of solar cell with and without a SiO_2 buffer layer under illumination of 15mW cm^{-2}.the inset plots out a simple band diagram of MoS_2/SiO_2/p-Si.

Below, heterojunctions formed by 2D TMDs are discussed. The huge family of layered materials allows for large flexibility of band engineering for building functional heterojunctions. Figure 1.9 (a) presents the calculated band structure of monolayer TMDs.[54] Hetero-stacking of materials with special band alignment could give birth to new functionalities. As it is commonly noted that a heterojunction with a straddling gap (type I band alignment) is advantageous for applications of light down conversion and the material with narrower gap is used as the emission layer. On the other hand, the photovoltaic

effect is expected across a staggered gap (type II band alignment). Considering the band alignment in the given diagram, the combination of MoS_2 and WSe_2 is suitable for photovoltaic cell due to type II band alignment, while the type I heterojunction may be formed by $MoTe_2$ and WSe_2. Here, we discuss recent reports on the type II heterojunction based on MoS_2, WS_2, $MoSe_2$ and WSe_2.

Band alignment between different MX2 upon physical contact has been investigated by several groups. Energy levels of monolayer WSe_2 and MoS_2 on HOPG has been studied by a combination of STS and UPS/XPS. The relative positions of bands are shown in Figure 1.9(b). The valence band offset between MoS_2 and WSe_2 is found to be around 0.83eV. Given the measurements of bandgaps of MoS_2 and WSe_2, the conduction band offset is calculated to be around 0.76eV. These values are in close accordance with the theoretical values.

Optical image of a typical MoS_2-WS_2 heterostructure is shown in Figure 1.9(c). This heterostructure was prepared by transferring CVD-grown monolayer WS_2 on top of CVD-grown monolayer MoS_2. It is evident from the image that the two layers conform to each other without forming structure disorders that are visible at optical wavelength.

As introduced previously, band structure and optical properties of bilayer MoS_2 in which two monolayers are stacked in the hexagonal symmetry, is quite different with those of monolayer, since the energy states near the conduction band minimum strongly relies on interlayer coupling and quantum confinement.[9] While weaker interlayer coupling is expected for a hetero-bilayer consisting of two dissimilar 2D layers, it is important to investigate the subtle modification of electronic structure when stacking monolayer MoS_2 and

WS_2 together. In the following, we will introduce recent reports on the optical and electrical properties of type II heterojunctions.

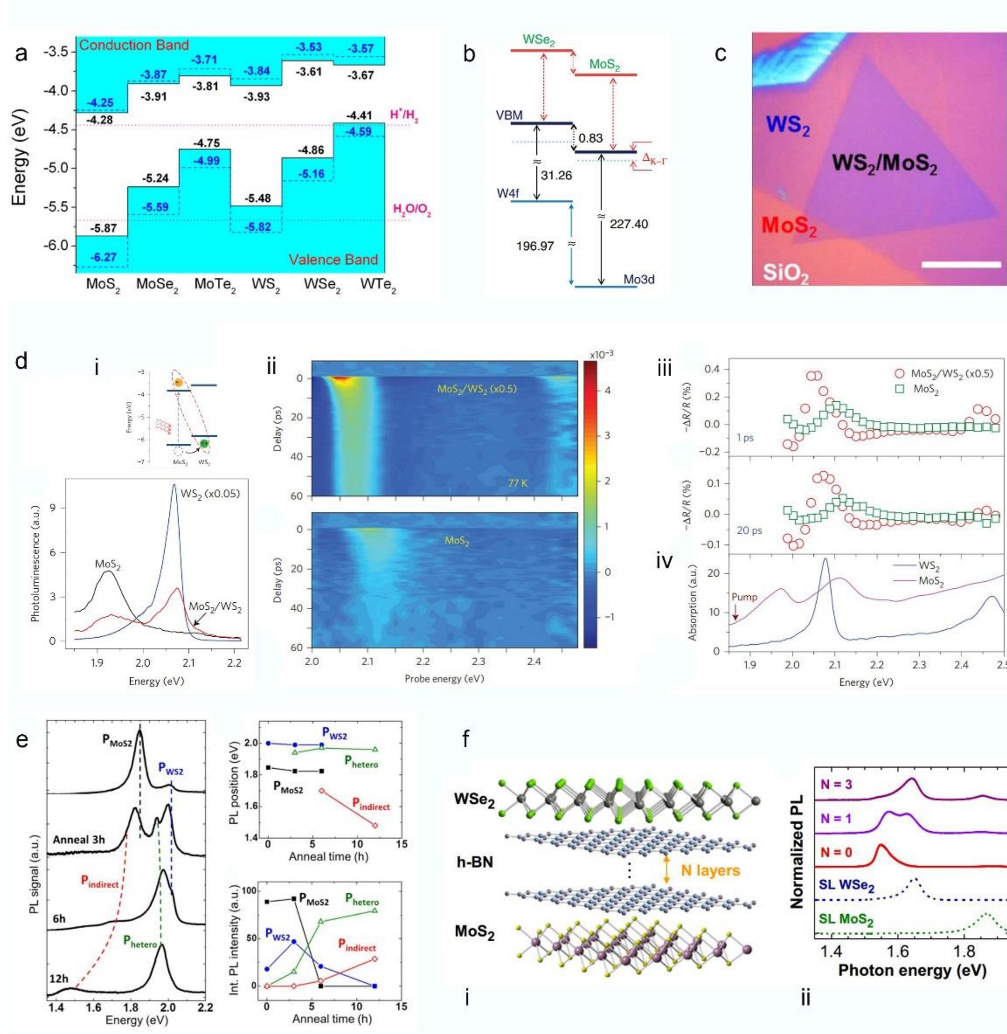

Figure 1.9 (a) Theoretical calculated band diagrams of monolayer TMDs. Solid lines are obtained by PBE, and dashed lines are obtained by HSE06.[54] (b) Band diagram of monolayer MoS_2 and WSe_2 on HOPG determined by STS. The valence band offset is determined to be 0.83eV.[55] (c) optical images of a large area MoS_2-WS_2 hetero-structure, prepared by PDMS-based wet transfer of CVD-grown WS_2 and MoS_2. The scale bar is 10um.[56] Reprinted with permission from ref 56. (d) i Schematic illustration of charge transfer between MoS_2 and WS_2 and Photoluminescence quench in the heterostructure. When the A-exciton of MoS_2 is optically excited, the holes in MoS_2 would transfer to WS_2 due to the valence band offset. ii transient absorption spectra for MoS_2-WS_2 heterostructure and isolated MoS_2 at 77K as a function of pump-probe delay time. Positive value means pump induced decrease of absorption. iii transient absorption spectra at a delay time of 1ps and 20ps for MoS_2-WS_2 heterostructure and isolated MoS_2. iv linear absorption of MoS_2 and WS_2 respectively.[57] (e) Photoluminescence of WS_2-MoS_2 heterostructure in

response to thermal annealing. Both emission peak and emission intensity evolves with annealing duration.[56] Reprinted with permission from ref 56. (f) Atomistic illustration of MoS_2/NL-hBN/WSe_2 heterostructure. The interlayer transition between MoS_2 and WSe_2 changes with the layer number of intercalated hBN.[58]

In a type II heterojunction, the VBM and CBM reside in two separate layers. When the heterostructure is optically excited, photo-generated electrons will relax to the layer with the lower CBM, whilst photo-generated holes will relax to the VBM of the other layer, as shown in Figure 1.9(d) i. However, it is unclear how the large binding energy of interlayer excitons influence this charge transfer process, since the band offset is typically smaller than the exciton binding energy, which is of the order of ~ 300meV.

Hong et al studied the dynamics of ultrafast charge transfer in atomically thin MoS_2-WS_2 heterostructure using combined PL mapping and femtosecond pump-probe spectroscopy.[57] PL spectra of isolated MoS_2, WS_2 and their heterostructure are shown in Figure 1.9(d) i. As can be seen, the emission of both A-exciton in MoS_2 and A-exciton in WS_2 becomes weaker in the heterostructure. This result is in accordance with the prediction of type II band alignment, because in type I heterojunction, PL of the narrower gap material is enhanced, whilst PL of the wider gap material is quenched. Further, ultrafast interlayer transfer dynamics of carriers in the staggered gap is confirmed by Pump-probe spectroscopy. As depicted in the transient absorption spectra Figure 1.9 (d) ii and iii, when only A-exciton of MoS_2 is excited, a large resonance feature is observed, which is ascribed to the A-exciton of WS_2 according to the linear spectra. Given that WS_2 has a larger optical gap than MoS_2, the strong transient absorption signal from WS_2

unambiguously implies modification of exciton transition in WS_2 by optical excitation of MoS_2. These results indicate that upon excitation, holes generated in MoS_2 quickly transfer to the VBM of WS_2 in time scales less that 100fs, resulting PL quenching in MoS_2. Similar phenomena have been observed in other hetero-structures such as MoS_2-$MoSe_2$ heterostructures.[59] The observation of ultrafast charge separation in TMDs-based heterojunction offers positive prospects for solar energy conservation.

In addition to the charge transfer phenomenon, S. Tongay et al [56]reported their findings on the strong interlayer coupling in MoS_2-WS_2 layer via PL spectroscopy. In a freshly prepared heterostructure, the PL spectrum shows characteristic peaks of MoS_2 and WS_2 monolayers. The authors find that the emission spectrum evolves with thermal annealing. Figure 1.9(e) shows the evolution of PL spectrum with the duration of annealing. Most importantly, a new peak appears at 1.75eV, which is lower than A exciton energy of both MoS_2 and WS_2, and gradually shift to 1.5eV with longer annealing. The emergence of this new peak could be attributed to interlayer interband transition across the staggered gap. Additionally, the gap between MoS_2 and transferred WS_2 also drops with annealing, from 1.6nm initially to 0.8nm. Note that 0.8nm is the typical interlayer separation in a multilayer. The reduced physical gap space implies enhanced interlayer coupling. As we discussed above, the CBM in MoS_2 is sensitive to interlayer coupling and quantum confinement. As vacuum annealing enhances interlayer coupling, the CBM in MoS_2 shifts from the K point, such that an indirect band gap is formed between the conduction band minimum in MoS_2 and valence band maximum in WS_2.

As the interlayer separation has a large impact on interlayer coupling, the band structure of heterostructure and its optical properties could be controlled by an insulating dielectric material in between the two layers. H. Fang et al[58] reported tunable interlayer coupling in van der Waals hetero-structures by inserting thin layers of hBN between WSe_2 and MoS_2. Figure 1.9 (f) shows the PL spectra dependent on the number of hBN layers. When there is no hBN layers, the interlayer transition peak dominates the PL spectrum and emission from intralayer excitons in both MoS_2 and WS_2 is negligible due to ultrafast charge transfer. The intercalation of hBN increases the gap distance and reduce interlayer coupling, so that the indirect interlayer emission is quenched and intralayer exciton emission becomes dominant. Interestingly, the interlayer emission persists up to three layers of hBN, suggesting that interlayer Coulomb forces are non-negligible at such separations. The tunability of interlayer coupling by insertion of dielectric layer represents unique approaches to controlling electronic properties of van der Waal heterostructure.

Now we review the recent reports investigating the electronic properties of van der Waals heterojunctions. Electrical performance of hetero-epitaxial bulk TMDs diodes have been studies decades ago. Early studies investigated PN diodes consisting of N-type $MoSe_2$ and P-type WSe_2 and good rectification behavior were observed.[6] Recently, Lee et al[60] reported gate tunable rectification behaviors and photovoltaic effects from an atomically thin PN junction made of monolayer MoS_2 and WSe_2 (Figure 1.10(a)). Figure 1.10(b) shows the band structure of the hetero-bilayer.

Upon contact, the system equilibrate by redistributing the carriers, driving electrons and holes and modifying the band offset. Therefore, electrons and holes are separated and confined in MoS_2 and WSe_2 as the majority carriers, respectively. Figure 1.10(c) shows the photo response under 532nm laser excitation. The authors find that much stronger response occurs at the hetero-bilayer compared to the individual monolayer region, which supports that the type II band alignment facilitates fast charge separation across the junction, leading to photovoltaic effect.

The IV curves at various gate voltages are shown in Figure 1.10(d). In comparison with the transfer characteristics of individual monolayer given in the inset, finite current is observed only when the two layers are in the “on-state”. Since 2D layers are too thin to support depletion, when the diode is positive biased, most of the voltage drops across the van der Waals gap. The results suggests the current under positive voltage i.e. forward bias is ascribed to the recombination of majority carriers, namely electrons in MoS_2 and holes in WSe_2. Two possible recombination mechanisms are proposed: Shockley-Read-Hall recombination by inelastic tunneling of majority carriers into trap states in the gap and Langevin recombination by Coulomb interaction. Higher bias raises the interlayer recombination rate and therefore results in diode-like behavior.

As the stacking is random, the momentum mismatch between MoS_2 and WS_2 leads to long recombination lifetime, which is favorable for solar energy conversion. The J-V curves under illumination is plotted as a function of gate voltage in Figure 1.10(e). The gate dependence of both J_{sc} and V_{oc} is

reported to be associated with the change of carrier density. Similar findings have also been reported by Furchi et al.[61]

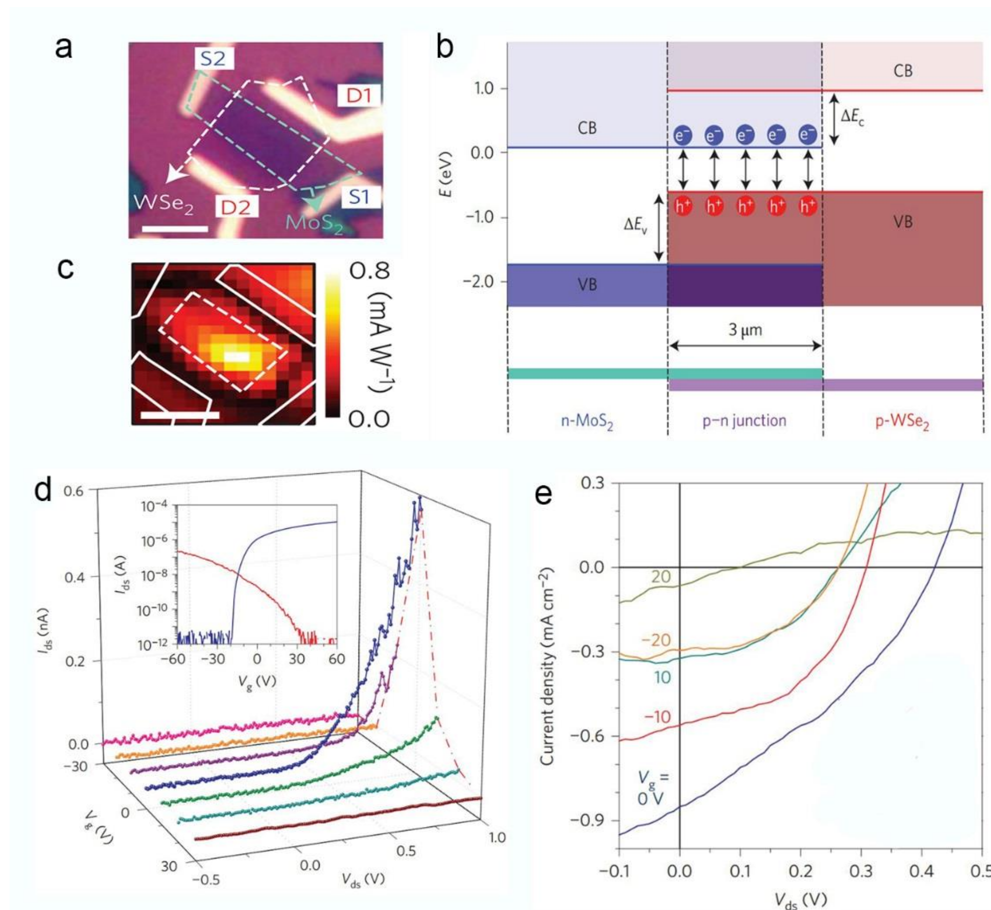

Figure 1.10 (a) Optical image of 1L MoS_2/WSe_2 device with source drain contact. (b) Energy band profile in the lateral direction from electrostatic simulation. MoS_2 and WSe_2 forms a staggered gap. Electrons and holes are separated by the large band offset. (c) Photocurrent mapping under 532nm laser excitation on the same device as (a). The overlapping junction area shows the highest photo response. (d) IV characteristics as a function of gate voltage. The inset shows the transfer curves of isolated MoS_2 and WS_2 FET plotted in the same frame. (e) J-V characteristic curve under illumination as a function of gate voltage. [60]

Electroluminescence, which is a reverse process of photovoltaic effect, has also been observed in van der Waals heterostructures. However, the

current of the monolayer MoS_2-WSe_2 hetero-structure is often limited by the small carrier density of individual layers. Cheng et al[62] took advantage of mechanically exfoliated multilayer MoS_2 with high electron density to form a LED with synthetic P-type monolayer WSe_2 (Figure 1.11(a)). Here, the multilayer plays the role of electron sources and monolayer WSe_2 act as the emission layer and provides holes for the formation of excitons. A sufficient positive bias breaks the balance between drift current and diffusion current and forces electrons to diffuse into WSe_2 and radiatively recombine with the majority holes and emit light, as illustrated in Figure 1.11(b). The EL emission spectra are shown in Figure 1.11(c). As can be seen, the EL spectra reflects emission from A, A' and B' excitons of WSe_2 as expected and the intensity increase linearly with current. More specific discussions on light emitting device will be covered in the section 1.6.

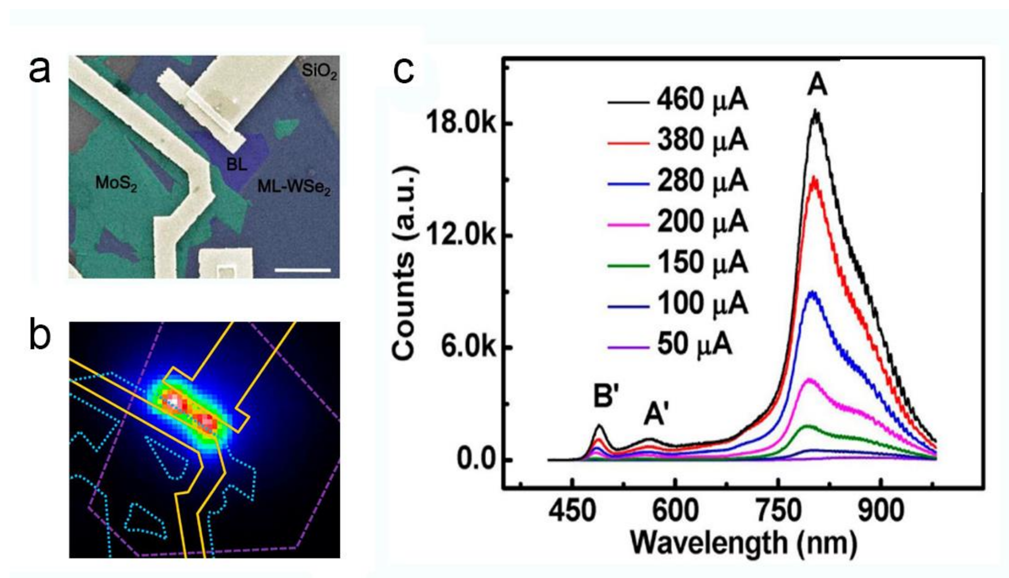

Figure 1.11 (a) Optical image of PN diode consisting of N-type multilayer MoS_2 and P-type monolayer WSe_2. (b) False color of electroluminescence image from the same device as (a). The emission is localized at the overlapping area close to the electrode. (c) Spectra of electroluminescence as a function of current.[62] Reprinted with permission from ref 62.

Despite the intrinsic type II band alignment between MoS_2 and WSe_2, Roy et al [63] reported the possibility of band alignment modulation by bias and electrostatic doping. In conventional heterostructures, strong covalent bonding maintains the band continuity at the interface regardless of the doping level, unless a dielectric buffer layer is inserted. However, in atomically heterostructures, most of the voltage drop across the van der Waal gap. This gap, as an insulating buffer layer, allows for band shifting under bias.

In another work, a dual-gated MoS_2-WSe_2 tunnel diode (Figure 1.12(a)) was fabricated to study electrically tunable band alignment. Here both multilayer MoS_2 and WSe_2 were heavily doped independently with bottom and top gate, respectively.[63] This allows crossover from type II to type III band alignment. In the type III band alignment regime, the diode exhibits negative differential resistance (NDR) similar to an Esaki diode (Figure 1.12(b)). As can be seen in Figure 1.12(c), the NDR peak arises due to band-to-band tunneling, when the VBM of WSe_2 aligns with the CBM of MoS_2. With further increase of the diode bias, the band gap is changed to type II alignment. The NDR peak shifts with gate bias, indicating that the relative band alignment is systematically modified.

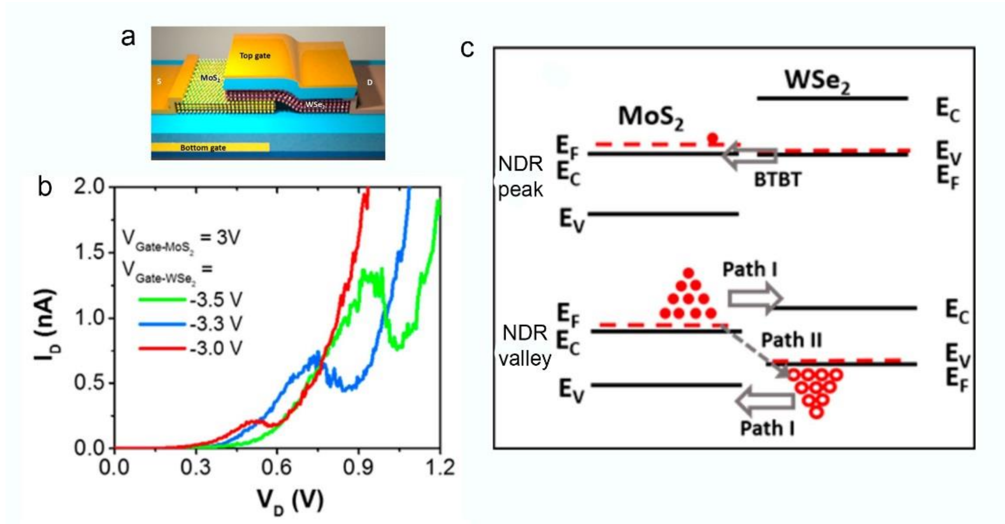

Figure 1.12 (a) Schematic of the dual-gated tunnel diode. (b) NDR at a fixed $V_{gate\text{-}MoS2}$ and varying $V_{gate\text{-}WSe2}$. (c) Band alignment at the NDR peak and valley. Reprinted with permission from ref 63.

Semiconducting 2D TMDs can be integrated together with metallic and insulating 2D materials to realize fully flexible 2D integrated electronic and optoelectronic devices. To this, graphene/graphite is suitable as electrode material whereas hBN is an excellent gate dielectric material due to its large breakdown voltage. Combination of these materials could produce a wide range of devices. Roy et al[64] demonstrated fabrication of TMDs-based transistors and diodes using graphene and hBN as the electrode and a dielectric layer, respectively. These devices were found to exhibit mobility and on-off ratios, comparable to those of conventional devices. Furthermore, Lee et al demonstrated to fabricate MoS_2 transistors with graphene electrode and hBN gate dielectric on flexible and transparent polymer substrate. [65]

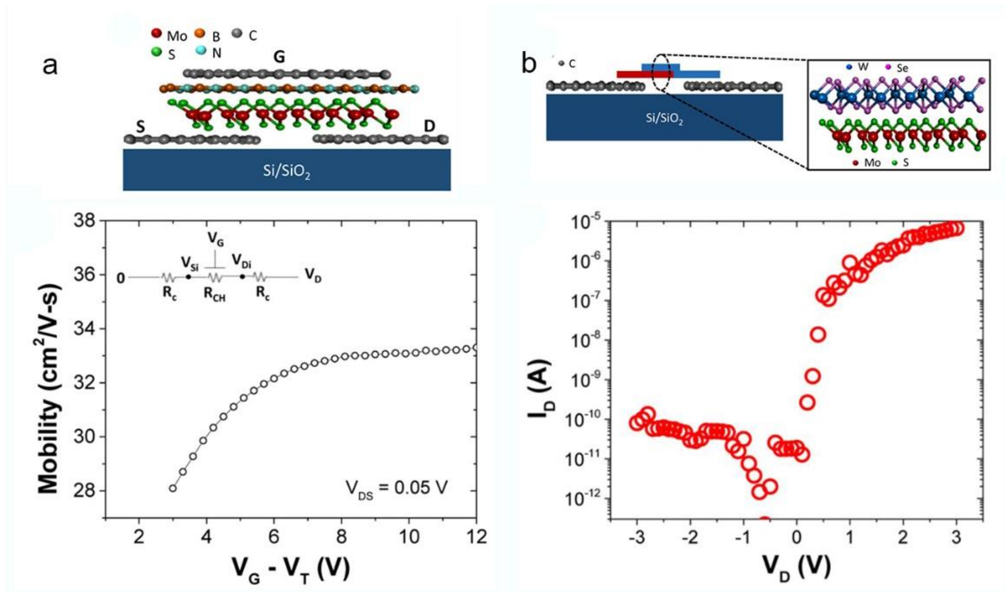

Figure 1.13 Transistor (a) and PN diode (b) made up of all two dimensional layered materials.[64]

1.6 Light emitting devices

Efficient electrically driven excitonic luminescence is key to develop electro-optic devices based on TMDs. Electroluminescence in monolayer MoS_2 was first reported in a metal-semiconductor junction consisting of 1L MoS_2 and Au.[66] It is demonstrated that Schottky junction can generate large local electric field. Therefore, carriers can gain sufficient energy and trigger impact excitation above a certain threshold energy.[67] Here, near the MoS_2-Au interface forms a strong band bending, which accelerates electrons injected under high bias and leads to production of electron-hole pair via impact ionization. The authors observed light emission near the contact at a large bias of 15V as shown in the inset of Figure 1.14(a). Figure 1.14(a) shows the absorption, PL and EL spectra. The emission peak of EL coincides with the PL of A exciton emission of PL, indicating that A exciton is generated due to impact ionization. The small shift, around 10nm, between absorption and EL could be attributed to inhomogeneous dielectric environment. However, the external quantum efficiency (EQE) of this Schottky diode is low $\sim 10^{-5}$, most likely due to the high threshold thermal energy for the production of excitons. It is commonly noted that quantum efficiency could be enhanced in a PN diode. In an effort to improve the EL EQE, heterojunction devices based on 2D TMDs have been tested by several research groups.

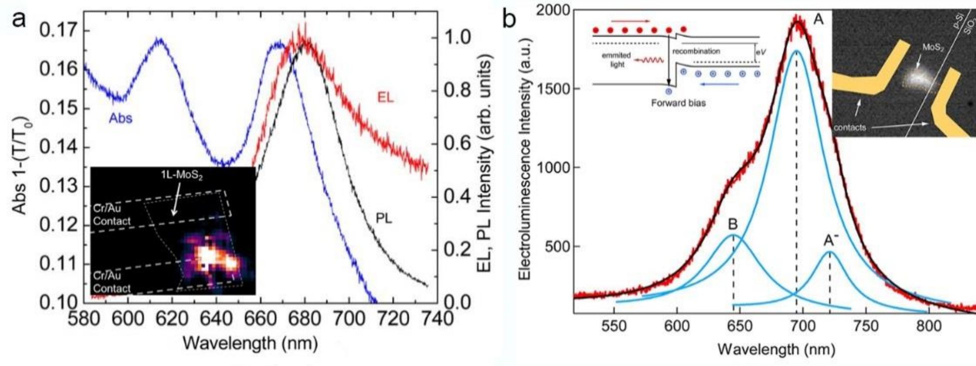

Figure 1.14 (a) absorption, EL and PL spectra from the same 1L MoS_2 device in one X axis. The inset indicates the false color image of electroluminescence in the Schottky diode around the junction area. [66] Reprinted with permission from ref 66. (b) EL spectrum acquired under a forward bias of 15V and a current of 1.8uA. Three emission peaks (A exciton, B exciton and A^- trion) are labelled by a multiple peak Lorentzian fitting. The insets present the false color image of EL and band alignment under positive bias.[68]

One of the main challenges in realizing monolayer MoS_2 based PN junction is the injection of holes. As MoS_2 is intrinsically N-type conduction behavior, it is challenging to realize P-type conduction by electrostatic doping due to the large band gap, while efficient substitutional doping of MoS_2 modifies its electronic structures. An alternate approach is to achieve hole injection from a P-doped material in a heterojunction. Kis' group reported fabrication of light emitting diode by transferring a monolayer MoS_2 on a P-doped silicon wafer. When a positive bias is applied, electrons and holes diffuse under the concentration gradient. Once a hole from P-Si transports through the hetero-interface, it recombines with an electron in MoS_2, yielding a photon at a certain probability (Figure 1.14(b)). The spectrum of EL under a forward bias of 15V is plotted in Figure 1.14(b). By multiple peak Lorentzian fitting, three emission peak are identified, corresponding to A exciton, B exciton and A^- trion. The emergence of B exciton implies the injection of hot carriers under high bias. In contrast to the case of Schottky diode, the entire

junction area is luminescent. On the other hand, recombination is also expected to occur in P-Si. Because interband transition in Si involves a phonon to satisfy conservation of momentum, non-radiative recombination dominates in silicon, yielding no significant luminescence. According to the I-V characteristics of heterojunction, the ratio of electron and hole current is proportional to $\exp(\Delta E_g/k_B T)$, where ΔE_g is the band gap difference, k_B is Boltzmann constant and T is temperature. Consequently, in the MoS_2-Si heterojunction, electron current far surpasses hole current. Thus, the majority of current fails to contribute to the luminescence. An alternative approach is to replace Si with a material with similar E_f as MoS_2 such that ΔE_g is small and the e-h current is balanced. In order to improve EQE, it is also important to avoid indirect SRH recombination, which is a non-radiative transition.

Except monolayer MoS_2, monolayer WS_2[69] and WSe_2[70] transistors demonstrate adjustable ambipolar behavior by ionic liquid or ultrathin dielectric gating. The feasibility of both N-type and P-type conduction by electrostatic doping offers another route to achieving light emitting devices from TMDs. Figure 1.15(a) illustrates an example of achieving light emission using ionic liquid gating.[71] Ionic liquid is well known for its extremely large capacitance induced by the electrical double layer. When the gate voltage satisfies: (1) $V_{gd}>V_{th}^e$; (2) $|V_{gs}|>|V_{th}^h|$, P- and N- doped regions are formed along the channel. Once $V_{sd}>0$, holes (electrons) diffuse in the direction (opposite to) the electric field and recombine in the junction center region. Figure 1.15(b) and (c) presents the image of EL and EL spectrum together with PL, respectively. The emission peak of EL matches well with the PL peak, indicating electrically driven excitonic emission from the direct band

gap. As the size of doping area can be adjusted by the gate voltage, this approach allows emission spot to be controllable by bias conditions.

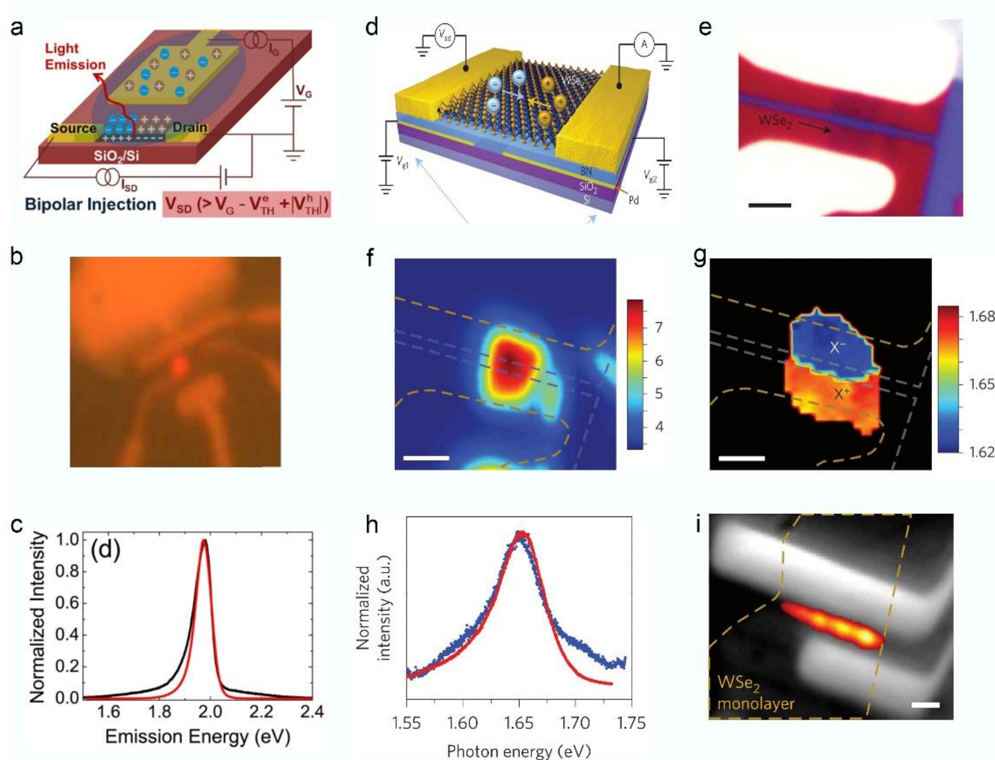

Figure 1.15 (a) schematic of electroluminescence in bipolar WS_2 transistor. (b) Optical image of WS_2 device under a bias of 2.9V (V_g=0.1V). The red dot indicates strong light emission. (c) Comparison of normalized EL and PL spectra of WS_2 transistor.[71] (d) Schematic of electroluminescence in local gated WSe_2 PN junction. (e) Optical image, (f) PL mapping and (g) PL peak energy mapping of the local gated WSe_2 junction. (h) Comparison of normalized EL and PL of WSe_2 PN junction. (i) Optical image of light emission, superimposed on the image of the device.[72]

Besides ionic liquid, thin flakes of hBN has also been used as local gate, as shown in Figure 1.15(d). Distinct from ionic liquid gating, the N-zone and P-zone are separately controlled by two independent local gates. Figure 1.15(f) and (g) show the image of PL mapping and PL peak energy mapping. The X^- and X^+ emission areas demonstrate the efficient N-doping and P-doping by the two gates. Similar to ionic liquid gating, the radiative recombination take place at the undoped region between the two gates, as shown in Figure 1.15(i).

It is important to know that in a homo-junction, electrons and holes contribute to the formation of excitons to the fullest, leading to high EQE. This is supported by very low turn-on current of around 200pA.[72] Ambipolar transistors has turned out to be an effective approach to efficient electroluminescence. However, these EL devices are not ideal for lighting application because the emission area is limited.

In order to achieve planar emission, 2D semiconductor layer needs to be integrated into a vertical structure where electrons and holes are injected into the emission layer uniformly. However, the lack of effective doping strategies, absence of suitable electron transport and hole transport layers and integration challenges add to the difficulties of realizing such vertical integrated devices.

Withers et al came up with an intelligent architecture of quantum well built entirely with layered materials, as shown in Figure 1.16(a).[73] In this structure, monolayer TMD is sandwiched by hBN layers and graphene layers are used as carrier injection layers. The entire device is encapsulated by hBN layers at both side. Figure 1.16(c) illustrates the band alignment of the two-terminal quantum well device under bias. When a bias is applied across the quantum well, it not only modifies the carrier distribution in graphene, but also facilitates the tunneling of carriers through hBN due to changes in work function. The hBN flake are chosen to be so thin (several layers) that a small bias can trigger the injection of carrier through the insulating barrier and thus induce carrier recombination in the semiconductor layer, as shown in Figure 1.16(d). Figure 1.16 (e) and (f) presents the tunneling current as well as 2D PL and EL spectra as a function of bias. The results indicate that EL is

predominately due to trion emission, with weak emission from lower energy states. It is reported that the quantum efficiency of such a single quantum well device is around 1%, probably due to high leakage through the ultrathin barrier. The stacking of multiple quantum well (MQW) offers an effective solution to enhance QE to ~10%, at the cost of increasing complexity of sample preparation and large overall resistance. The well-built structure resulted in record high quantum efficiency values, highlighting the potential of all 2D integration. The PL quantum yield of single layer MoS_2 and WS_2 has recently been reported to reach up to 95% after appropriate chemical treatments. [48] Therefore, there is still huge room for improvement of EL EQE.

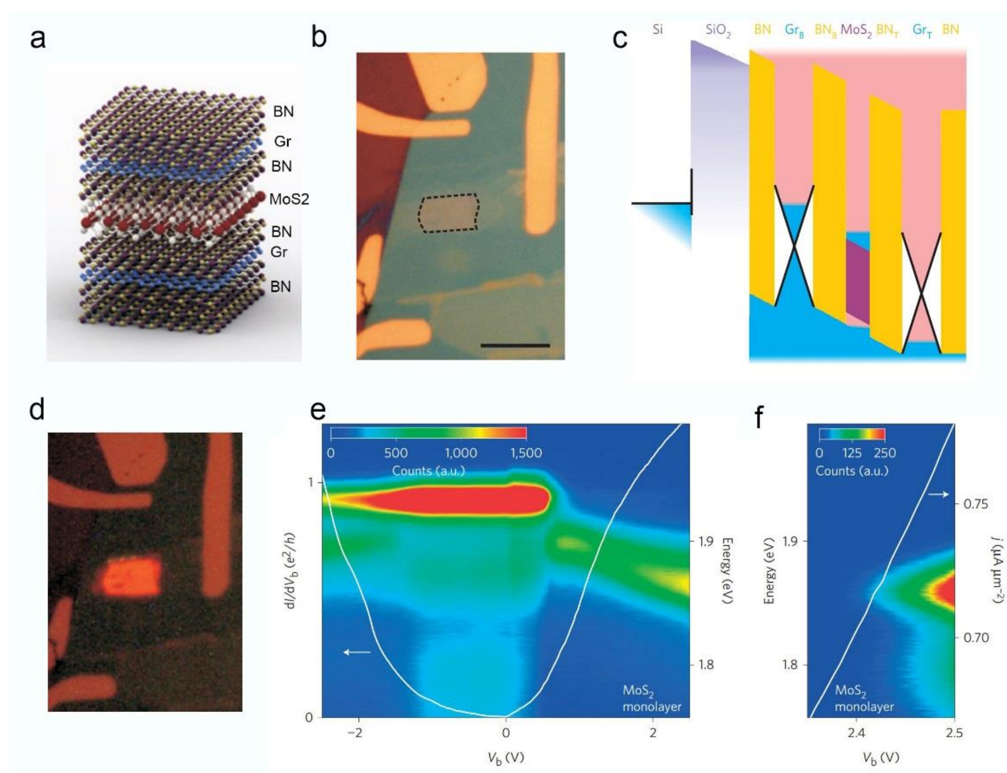

Figure 1.16 (a) schematic and (b) optical image of a single quantum well device. (c) Illustration of carrier distribution and working mechanism of QW device. (d) Optical image of an electrical excited quantum well under sufficient bias. (e) PL spectra and (f) EL spectra as a function of bias. The white line demonstrates the current-voltage characteristic.[73]

1.7 Summary

Despite the chemical stability of TMDs, the ultrathin body makes them sensitive to the external circumstance. Therefore, in chapter 2, we will investigate on the effect of ambient air to WSe_2 and $MoSe_2$ transistors. In addition, it is necessary to achieve both n- and p-doping in the wide band gap TMDs in order to build a robust PN junction. So, in the rest of chapter 2, we will show the utility of O_3 as a strong oxidizing agent to realize efficient P-doping in WSe_2 transistors.

In chapter 3, we will present our results on the new hetero-structure built with TMDs flakes. The electronic structure of the WSe_2-MoS_2 hetero-bilayer is investigated via PL mapping. We go on with electrical characterization of these heterojunction. At length, we explore the photovoltaic effects of these hetero-structures and propose a new structure for improvement.

In chapter 4, we will briefly discuss the limitations of current TMDs based light emitting devices and report our results on bright planar emission in metal-insulator-semiconductor (MIS) diode built from van der Waals heterostructures. We will show the perfect rectification behavior and high quantum efficiency of our MIS device. At last, we ascribe the high efficiency to carrier multiplication due to impact ionization.

2 Effect of Oxygen and Ozone on P-type Doping of Ultra-thin WSe_2 and $MoSe_2$ FETs

2.1 Introduction

Atomically thin layers of semiconducting transition metal dichalcogenides (TMDs) has aroused remarkable interests as novel materials for next-generation electronics and optoelectronics[8]. Field-effect transistors (FETs) based on TMD layers exhibiting high field effect mobility and large on-off ratio have been demonstrated by a number of research groups[39, 43, 74, 75, 76, 77]. The atomic thickness of these materials allow ultimate gate coupling and offer solution to short channel effects such as drain-induced barrier lowering and leakage current[78]. It is anticipated that these materials will enable realization of flexible and small-form-factor devices on a variety of surfaces [43, 79].

One of the fundamental challenges for the realization of TMD-based CMOS-type devices is controlled and reliable doping. The implementation into logic gate and diodes necessitates the establishment of a technique to achieve both N-type and P-type in TMDs, especially the thinnest ones. It has been reported that cation substitution of group 6 TMDs such as MoS_2 with group 5 and group 7 elements leads to p-type and n-type doping, respectively [80]. However, substitutional doping could only been achieved during crystal growth and the control over the doping concentration is limited during the chemical vapor transportation. Furthermore, carrier mobility in substitutionally doped TMDs is significantly compromised by ionized impurity scattering due to the introduced dopant[81].

Charge transfer doping is a viable approach for modulating carrier concentration in two-dimensional (2D) semiconductors. Recent studies have shown that both n- and p-type doping can be induced by exposing 2D TMDs to oxidizing or reducing species with suitable redox potential[82, 83, 84]. For example, NH_3 and NO_2 can be used to dope MoS_2 n-type and p-type, respectively[85]. An adlayer of MoO_x having a large work function has also been shown to strongly dope 2D TMDs p-type[86, 87]. Doping by both physisorbed and chemisorbed species has been reported.[83]

While oxygen is recognized as a common adsorbate and an electron acceptor for carbon nanotubes and graphene[88, 89], its role on TMDs has not been systematically investigated. Here, we report the effects of oxygen and ozone on the transfer and output characteristics of mono- and few-layer WSe_2 and $MoSe_2$ FETs. We show that oxygen and ozone exposure result in metastable p-type doping and substantial increase in hole conductance. Our results demonstrate that while the doping mechanism is similar to that of ambient oxygen, ozone is a significantly more efficient electron acceptor owing its large redox potential. Further, we show that the presence of water adlayer that solubilizes the oxygen and ozone molecules is essential in invoking their powerful oxidizing properties.

2.2 Methods and experimental details

Device fabrication WSe_2 and $MoSe_2$ flakes were mechanically exfoliated on top of a silicon substrate with a 300nm thick SiO_2 layer and subsequently identified under an optical microscope. Standard electron beam lithography techniques were used to define alignment marks and then draw electrode patterns, using 950 PMMA A5 as the resist. Afterwards, Cr/Pd/Au (2nm/20nm/30nm) was thermally evaporated in sequence as the electrodes. Palladium was used because it acts as a good hole injection contact.

Electrical characterization All electrical measurements were conducted at room temperature in nitrogen-filled glove box. Transfer characteristics curves were collected by Agilent parameter analyzer B1500A. Source-drain bias was fixed at 1V for all gate sweep measurement. Measurements on UV/ozone-treated devices were conducted 5~10 min following the procedure. Thus, effects of residual photoexcited carriers can be ignored.

Ozone treatment Ozone was produced by a UV/ozone procleaner (BioForce Nanoscience). The devices were loaded into the chamber and the UV light was switched on for 1 minute, after which they were kept in the chamber for 10 minutes. The UV irradiation time was deliberately set low to avoid oxidation. Slightly longer UV irradiation time (3 min) was used for the devices for TLM measurement.

2.3 Results and Discussion

Mono- and few-layer WSe_2 and $MoSe_2$ devices were fabricated following standard electron-beam lithography and electrode metal deposition. The electrical properties of the devices were then measured in a nitrogen-filled glove box. In typical fabrication procedures, the devices were annealed in the glovebox in order to drive off any residual adsorbates on the surface of the channel and improve metal-semiconductor contacts. In the following discussions, we refer to these annealed devices as "intrinsic" due to minimal surface adsorbates.

2.3.1 Effects of ambient air

The WSe_2 transistors were first exposed to ambient air (relatively humidity of ~ 70%) for a long time. During ambient exposure, water is also expected to adsorb on the channel surface due to hygroscopic nature of TMDs. The effect of surface adsorption of ambient oxygen on the device properties were studied by thermal annealing in N_2 filled glovebox and monitoring the electrical performance.

Figure 2.1(a), (b) and (c) shows the transfer curves of monolayer, bilayer and multilayer WSe_2 at different annealing temperatures for 10 minutes. In those three devices, the transfer curves demonstrate horizontal shift of threshold voltage to the negative direction of gate voltage with higher annealing temperature. In the case of bilayer and multilayer, the transistors even demonstrates ambipolar behaviors. As thermal annealing simply removes air adsorbates from the surface of these transistor, the effect of ambient air is considered to induce P-type doping, based on the n-doping-like behavior of

thermal annealing. As would be discussed later, this doping process is reversible.

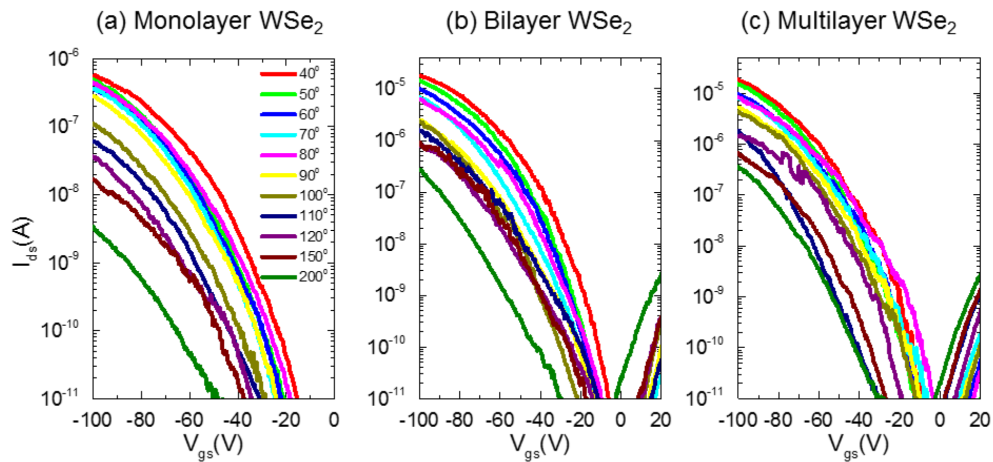

Figure 2.1 $I_{ds} - V_{gs}$ relationships of (a) monolayer WSe_2, (b) bilayer WSe_2 and multilayer WSe_2 after thermal annealing in N_2 filled glovebox at different temperatures.

2.3.2 Doping effects of ozone

The effect of ozone on the device properties was studied by exposing the device to ozone in UV-ozone generator in the presence of ambient gas at room temperature (Figure 2.2(a). See Methods for the details of ozone exposure). The level of ozone adsorption was controlled by varying the exposure time and the number of exposures.

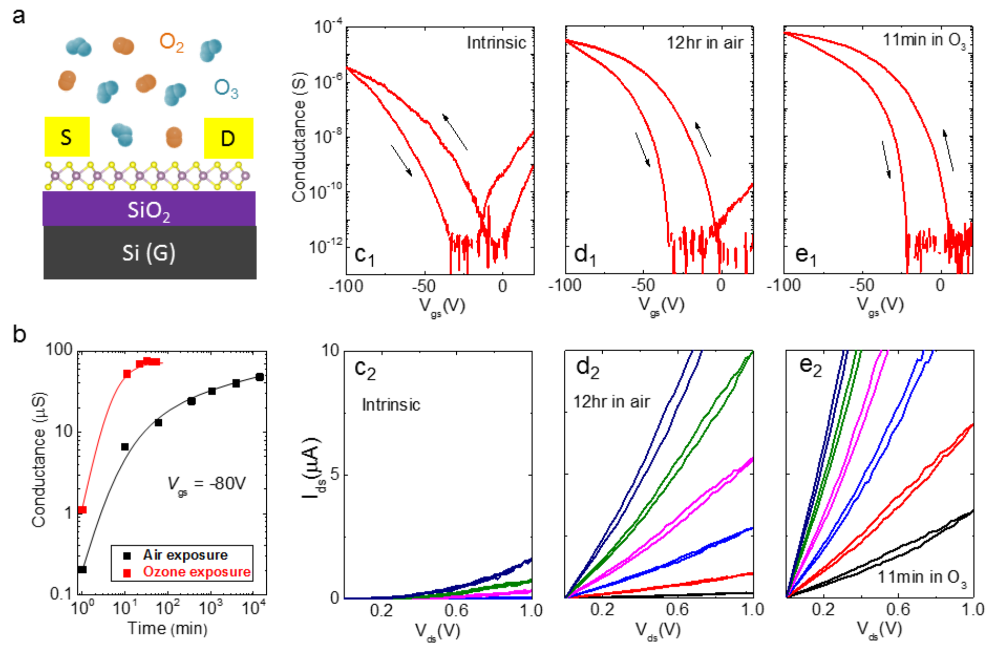

Figure 2.2 (a) Schematic diagram of WSe_2 transistor exposed to a mixture of oxygen and ozone molecules. (b) Conductance of a bilayer WSe_2 device at V_g = -80 V as a function of air and ozone exposure time. (c-e) Transfer (upper panels) and output (lower panels) curves of a bilayer WSe_2 device in its intrinsic state (c), after air exposure for 12 hours (d), and after subsequent ozone exposure for 11 minutes (e).

Figure 2.2 (b) shows changes in device conductance at Vg = -80 V as a function of progressive air and ozone exposure. Air-doping occurred gradually over a period of one week with a slow increase in device conductance by 3 orders of magnitude. In contrast, ozone led to immediate enhancement in device conductance by 3 orders of magnitude within the initial 11 minutes. Note that the enhancement achieved within 20 minutes of ozone exposure was larger than that achieved by air doping after one week. The general saturating trends are similar to those reported for air-doped graphene transistors.[88]

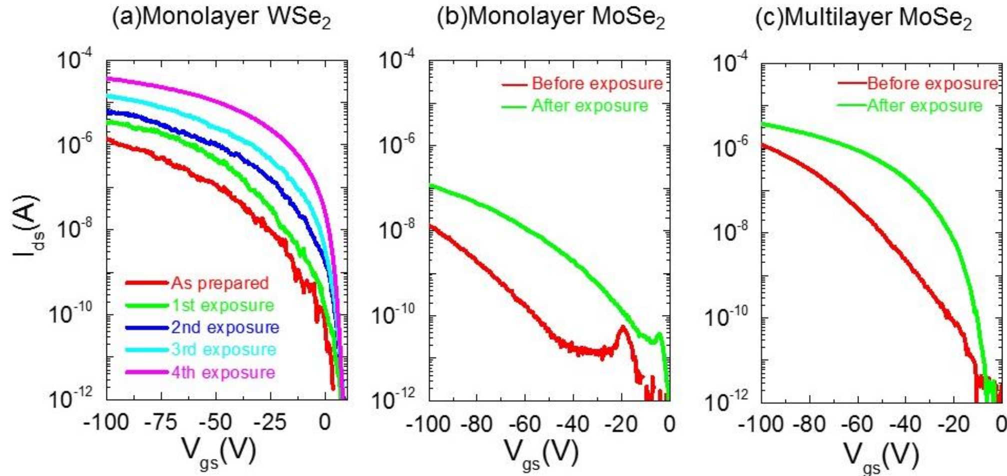

Figure 2.3 (a) Transfer curve of monolayer WSe_2 before and after step by step ozone exposure. At each exposure step, the device was illuminated with UV light for 1 minute and left in the chamber for 10 minutes to allow ozone molecules to adsorb on the surface. Transfer curves of monolayer (b) and multilayer (c) $MoSe_2$ before and after ozone exposure.

Figure 2.2 (c) shows the transfer curve of a bilayer WSe_2 device in its intrinsic state while Figure 2.2(d) and (e) are those after exposure to ambient air for 12 hours, and after subsequent exposure to ozone for 11 min, respectively. Ambient air and ozone exposure resulted in progressive shift of the threshold voltage of both hole branch and electron branch to larger back gate voltages revealing increasing p-type character. Correspondingly, the maximum on-state current density increased from 1.6 μA/um to 15 μA/um by air exposure, and to 30 μA/um by ozone exposure, resulting in an increase in on-off ratio to above 10^7. Similar behaviors were observed for monolayer WSe_2 (Figure 2.3(a)), mono- and few-layer $MoSe_2$ (Figure 2.3(b) and (c)).

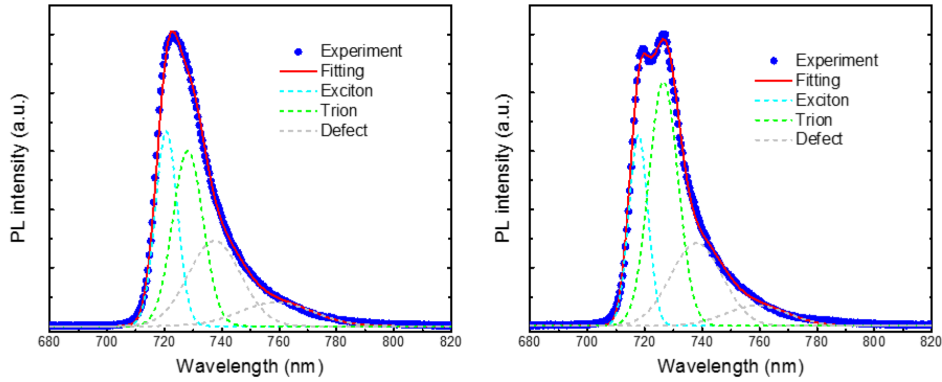

Figure 2.4 Photoluminescence (PL) of monolayer WSe_2 after air exposure for several days (a) and after subsequent ozone exposure for 11 mins (b). The spectra were fitted with exciton, trion and localized states emission peaks. The spectra were obtained in nitrogen atmosphere at liquid nitrogen temperature (77K).

In order to verify that the above observations are due to an increase in hole concentrations, we studied the low temperature photoluminescence spectrum of the samples. The photoluminescence spectrum of monolayer WSe_2 at 77 K after air exposure for several days (Figure 2.4(a)) and after ozone treatment for 11 min (Figure 2.4(b)) reveals peaks arising from the neutral excitons and trions, or charged excitons, as expected for doped samples. The separation between the twin peaks is 21 meV which is consistent with the binding energy of trions in WSe_2.[90] As can been seen, the trion-exciton intensity ratio for ozone-treated sample is larger than that for air-exposed sample, indicating higher hole density achieved with ozone treatment.

2.3.3 Reversibility of ozone doping

Similar to ambient gas doping of MoS_2[91], ozone doping was found to be a reversible process. Annealing ozone-treated devices in nitrogen atmosphere above 150 °C resulted in lower conductance of the original

intrinsic state. Subsequent second exposure to ozone recovered the high doping state equivalent to that of the first exposure. As can be seen in Figure 2.5, this doping and de-doping process can be repeated several times with high reproducibility, indicating no degradation of the material. These findings suggest that the doping is enabled by physisorption rather than chemisorption of ozone molecules.

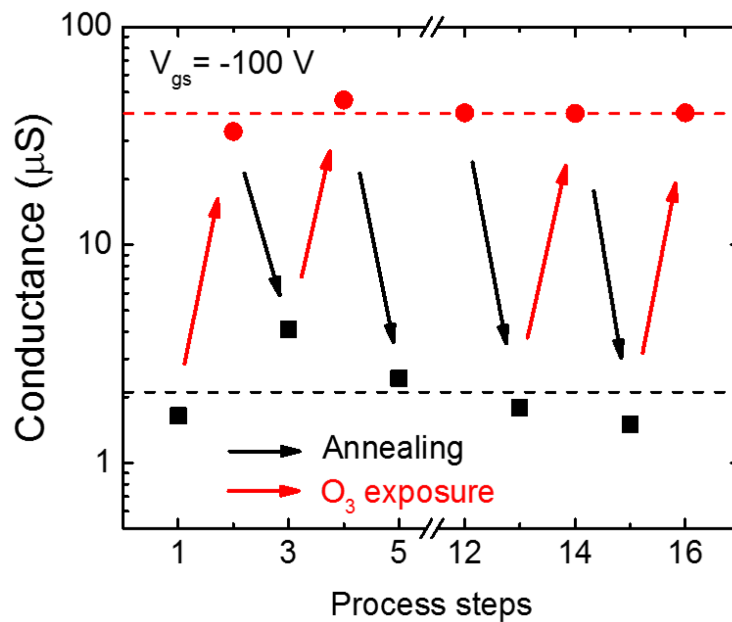

Figure 2.5 On-state conductance of a bilayer device at V_g = -100 V after exposure to ozone and annealing over multiple cycles. The device shows consistent undoped and doped conductance of ~2 μS and ~40 μS, respectively.

2.3.4 The change of R_c and R_{sh} after ozone treatment

The drastic enhancement in channel current upon exposure to ambient air and ozone can be attributed to changes in the contact resistance (R_c) and channel sheet resistance (ρ_{sh}). We investigated the changes in these contributions in devices using transfer length method (TLM). TLM is a

technique to extract contact resistance and sheet resistance simultaneously by studying the scaling behavior of the total device resistance with channel length. Using two-probe technique, we measure the total resistance between each two adjacent contacts of different separation prepared on the same crystal. The total device resistance scales as $R_{tot}=2R_c+\rho_{sh}\cdot L/W$, where L is the channel length and W is the channel width. Since the contact resistance and sheet resistivity are constant, the intercept and the slope of R_{tot}-L plot yields R_c and ρ_{sh}/W, respectively. We studied few-layer devices with channel lengths ranging from 1 to 5 μm (See Supporting Information for details of device fabrication). Figure 2.6(a) and (b) show R_{tot}-L plots for devices measured before and after ozone exposure. Both contact resistance (Figure 2.6 (c)) and sheet resistance (Figure 2.6 (d)) at a given gate voltage shows a decrease by a factor more than 2 after exposure to ozone.

We evaluated the field effect mobility of the devices by $\mu= 1/C_{ox} \times [d\rho_{sh}^{-1} /dV_g]$, where C_{ox} is the oxide capacitance. The mobility of the device before and after exposure was found to be 98.7 $cm^2/V\cdot s$ and 99.3 $cm^2/V\cdot s$, respectively. The negligible change in mobility suggests that ozone adsorbates are not the dominant scattering centers in these systems. This observation is consistent with the non-covalent nature of ozone doping. Given that the mobility is not affected by ozone doping, the carrier density introduced by ozone can be estimated from the horizontal shift of ρ_{sh}-V_g plot (Figure 2.6 (d)), which is found to be around 37 V. From the oxide capacitance, this shift corresponds to ozone-induced carrier density of 2.7×10^{12} cm^{-2}.

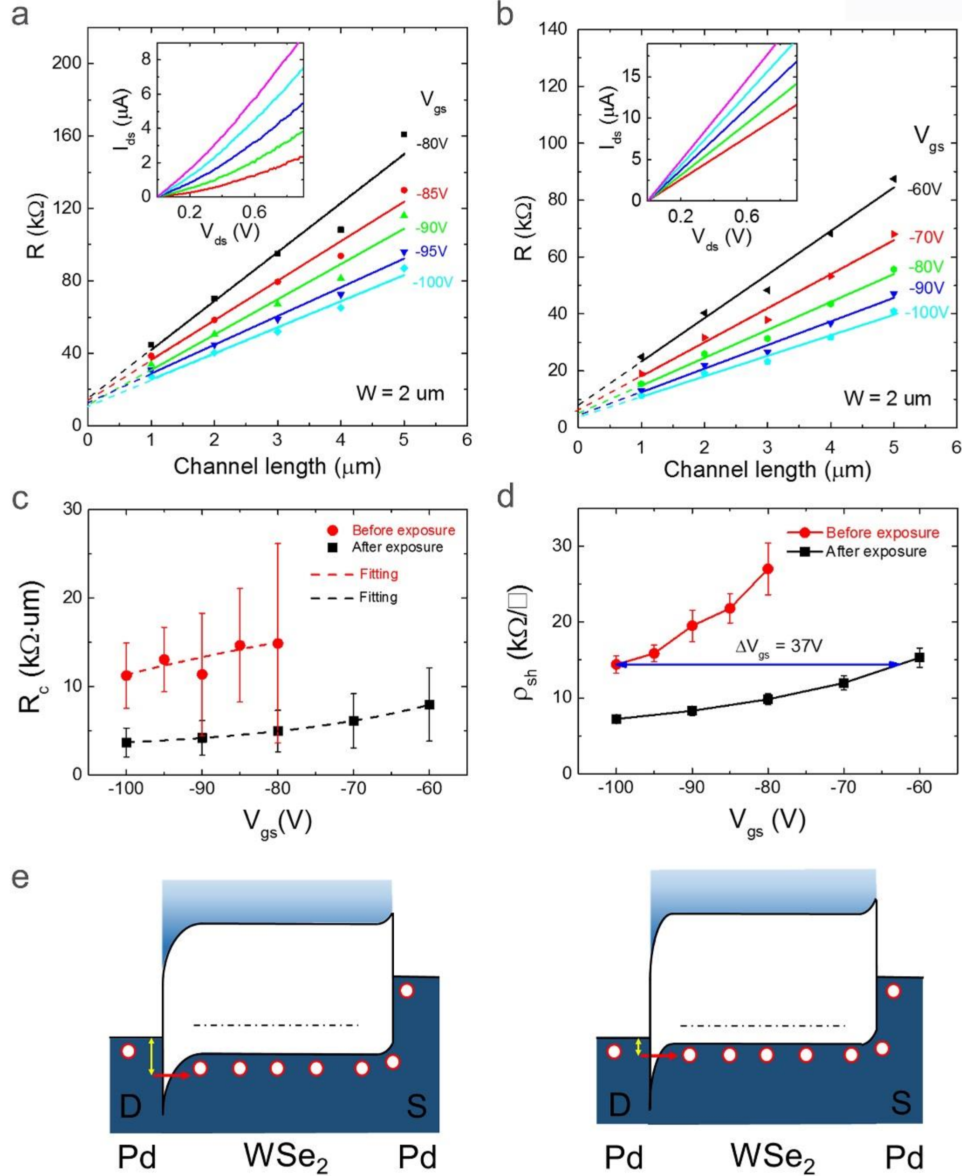

Figure 2.6 (a,b) Total resistance of multilayer WSe_2 devices as a function of channel length at different gate voltages before (a) and after (b) ozone exposure. The insets show output curves at gate voltages ranging between -60 and -100 V in 10 V steps. (c,d) Extracted values of (c) R_c and (d) ρ_{sh} as a function of gate voltages for deivces before and after ozone exposure. The dashed line in (c) is a fit according to Eq (1). (e) Schematic band diagram of WSe_2 transistor with Pd source and drain contacts. The dashed line indicates the Fermi level (E_F). In a weakly doped device, current injection is limited by the Schottky barrier at the contact. After doping, the Schottky barrier becomes narrower and thermionic tunneling of holes is facilitated.

Reduction in contact resistance can also be explained by increase in hole density in the channel and corresponding shift in the Fermi level. The

lowering of Fermi level causes narrowing of Schottky barrier and the depletion region (Figure 2.6 (f)). Since carriers are mostly injected into the channel by thermally assisted tunneling[92], the tunneling probability increases exponentially with decrease in barrier width. This is schematically shown in Figure 2.6. The relationship between contact resistance and carrier density is given by[93]

$$R_c \propto e^{-(\frac{4\pi}{h}\phi_B\sqrt{(\varepsilon m_p)/(qp)})} \quad (1)$$

where Φ_B is the Schottky barrier height , ε is the dielectric constant, m_p is the effective mass of holes and p is the hole density. Note that the contact resistance decreases with decreasing gate voltages for before and after ozone treatment. The $R_c - V_g$ plot in Figure 2.6 (c) shows good agreement with Eq (1). This observation also indicates that thermionic emission is not a dominant carrier injection mechanism in these devices.

2.3.5 Charge transfer between TMDs and O_3/H_2O redox couple

Lavesque et al.[88] showed that oxygen doping in graphene occurs via solvation of the molecules in water adlayer. Doping by ambient air was attributed to electron transfer from graphene to an O_2/H_2O redox couple such that

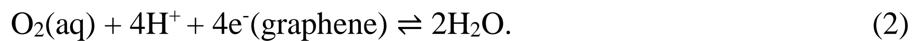

$$O_2(aq) + 4H^+ + 4e^-(\text{graphene}) \rightleftharpoons 2H_2O. \quad (2)$$

Similar observations have been reported for carbon nanotube FETs[89]. We thus hypothesize that a similar doping mechanism is at play in our air- and ozone-doped devices. To test this hypothesis, we investigated the role of water

on doping in WSe_2 by exposing dehydrated device to oxygen and ozone. Dehydration of the device surface was achieved by placing the device in an air-filled and sealed quartz tube and annealing it at 150°C for half an hour. The device was then cooled in a temperature gradient in order to avoid recondensation of water vapor on to the device channel (Figure 2.7 (a)). Note that the device prepared in this way is exposed to oxygen but in absence of significant water adlayer. The quartz tube containing the device after annealing was then loaded inside an ozone stripper. Since quartz is transparent to UV light, ozone is generated inside the quartz tube containing oxygen gas. The device was subsequently measured in nitrogen atmosphere without exposing it to ambient air. Two-probe transfer curves of a dehydrated bilayer WSe_2 device exposed to oxygen and ozone are shown in Figure 2.7 (b). Interestingly, no sign of significant doping was observed in these devices. These observations indicate that presence of water adlayer on the surface of WSe_2 is essential for doping by either oxygen or ozone, similar to the case of graphene. It is also worth noting that dehydrated devices often showed reduction of hole current after prolonged ozone exposure. In fact this reduction in conductivity was irreversible suggesting that ozone tends to oxidize or etch WSe_2 in the absence of protective water adlayer as reported in a recent study[94].

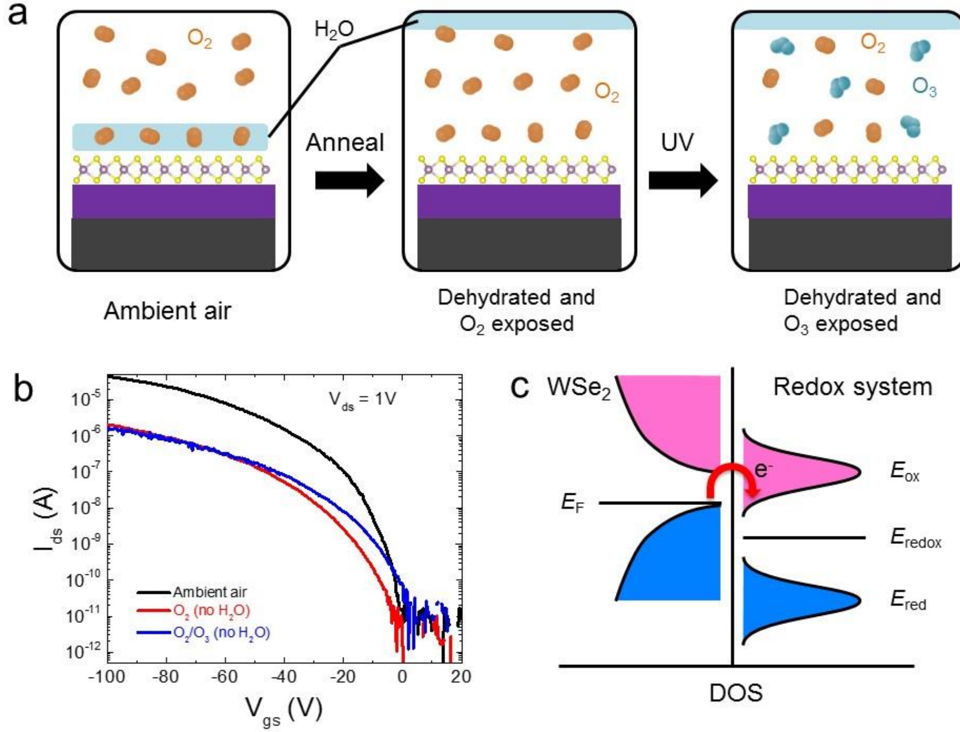

Figure 2.7 (a) Schematic showing the scheme for studying the role of water in oxygen and ozone doping. The water adlayer was removed by annealing the device enclosed in a quartz tube and cooling it over a temperature gradient to condense moisture on the inner walls of the quartz. Ozone is subsequently introduced by UV light exposure. (b) Transfer characteristics of the device in the conditions as illustrated in (a). (c) Schematic energy diagram showing the DOS of WSe_2 (left) relative to that of O_3/H_2O (or O_2/H_2O) redox system (right). Electrons transfer from WSe_2 to the redox system driven by the difference in E_F and E_{redox}.

With these experimental findings, we can now better understand the doping mechanism. In ambient conditions, physisorption of water on TMD surfaces and interfaces is ubiquitous[39 88 95]. In the case of ozone doping, this water adlayer solvates O_3 molecules, establishing a redox reaction

$$O_3(aq) + 2H^+ + 2e^-(WSe_2) \rightleftharpoons O_2 + H_2O \quad (3)$$

Ozone is a strong oxidizing agent and its redox potential E_{redox} lies below the chemical potential or Fermi level of WSe_2, $E_{F,WSe2}$. Thus, electrons are withdrawn from WSe_2, reducing its chemical potential until equilibrium is

reached (Figure 2.7 (c)). Correspondingly, the hole density in WSe_2 increases, giving rise to enhanced hole conductivity.

Rapid doping of WSe_2 by ozone can be attributed to both its high oxidation potential and high solubility in water adlayer. According to the Nernst equation[88], the redox potential of a redox system can be estimated by

$$E_{\mathrm{redox}} = \mu_{e(SHE)} + E^{o}_{redox} - \frac{\alpha k_B T}{n_e F}(log(c_{OX}) - 4pH). \quad (4)$$

Here, $\mu_{e(SHE)}$=4.44eV is the standard hydrogen electrode (SHE) potential relative to the vacuum level, E^{o}_{redox} is the standard electrode potential of the reaction versus SHE, α is chemical activity, $k_B T$ is the thermal energy, n_e is the number of electrons, F is the Faraday constant, and c_{ox} is the concentration of O_2 or O_3. The value of c_{ox} is dependent on the solubility of the oxidizing agent in water. At room temperature, the solubility of ozone in water is more than 10 times that of oxygen. Given the standard electron potential of ozone (~2.08 eV) and oxygen (~1.23 eV), the redox potential of ozone lies below that of O_2, ranging from -5.3 eV to -6.42 eV for a realistic acidity of water in air (~pH=6)[88] . On the other hand, the valence band maximum for monolayer WSe_2 is predicted be at -5.16 eV by first principle calculations[96]. Thus, electrons in WSe_2 have sufficient driving force to transfer to the redox system in both O_2 and O_3 based redox systems. The efficient ozone-induced doping can be explained in terms of its high large standard electrode potential and water solubility of ozone. Further, the ability of ozone to render SiO_2 surface more hydrophilic may also explain the efficient doping.

2.4 Conclusion

We report the role of oxygen and ozone on p-type doping of WSe_2 and $MoSe_2$ devices. Both molecules are shown to induce increase in hole density via a non-covalent charge transfer process, leading to significant increase in hole conductance. Doping occurs by solubilization of oxidizing molecules in water adlayer that is naturally present in devices exposed to ambient air and thereby forming a redox couple with a chemical potential higher than that of WSe_2 and $MoSe_2$. Due to the higher oxidation potential and water solubility, ozone is significantly more efficient in doping these materials compared to oxygen. Nevertheless, oxygen doping can be equally effective after prolonged exposure to ambient air. These findings indicate that care needs to be taken when evaluating intrinsic device performances due to significant extrinsic effects arising from ordinary surface adsorbates.

3 Photovoltaic Effects in Layered TMDs-Based Heterojunctions

3.1 Introduction

As discussed in Chapter 1, ultrathin layers of TMDs hold promise for the applications in thin film optoelectronic device. TMDs exhibit unusually large light absorption per layer at resonance frequencies,[10, 50] highlighting their potential for photodetectors and solar cells. Recently, a number of papers reporting on the photo-response properties of mono- and multilayer TMD two photo-detectors and phototransistors have emerged in the literature.[97, 98, 99, 100] The relatively large band gap of monolayer TMDs along with its ultrathin body allows efficient electrostatic control of these phototransistors. The highest photo-responsivity is reported to be of 880 AW^{-1} for a single layer MoS_2 phototransistor at a detection wavelength of 561 nm .[97] This value is significantly higher than those of silicon- and graphene-based devices. Despite the high responsivity, TMD-based devices tend to exhibit significantly slow response, which has been ascribed to charge trapping by silicon substrate.

In addition to photodetectors, the remarkable absorbance of TMDs along with its moderate carrier mobility and flexibility make them attractive for applications in large area flexible solar cells. For solar energy conservation, a PN junction with robust build-in electric field is required to generate photovoltage on top photocurrent. Recently, Pospischil et al[101] reported fabrication of lateral PN diode in monolayer WSe_2 via electrostatic doping using a split gate device configuration. The power conversion efficiency (PCE) for these devices were estimated to be around 0.5 %. Considering that the

active region of these devices are sub-nanometer thick and that the device design has not been optimized, such PCE values are remarkable. However, these devices suffer from low photocurrent and photovoltage. The low photovoltage may be attributed to low carrier concentration achieved by electrostatic gating. This may be further improved by employing more efficient doping techniques. On the other hand, low photocurrent is due to the small active region, which is limited to the microscopic intrinsic region between the two split gates.

In contrast to lateral devices, vertical heterojunctions of TMDs allow energy harvesting over a large area. The type II heterojunctions formed by dissimilar TMDs with different band gaps are favorable for efficient light absorption and separation of charges. Since TMDs exhibit thickness-dependent band gaps, they offer a variety of designs for the exploration of heterojunctions suitable for photovoltaic devices.

As-synthesized MoS_2 typically exhibits N-type conduction,[38, 39] while P-type conduction of WSe_2 can been achieved by electrostatic doping.[42, 70] PN junctions formed by monolayer MoS_2 and WSe_2 have been shown to exhibit photovoltaic effects albeit with low I_{sc} and V_{oc}.[61] In this Chapter, we will present our investigation on the photo-response and photovoltaic effects in MoS_2-WSe_2 NP vertical heterojunction. First, we demonstrate the formation of a type II heterojunction using PL mapping. In addition, we show that these devices exhibit "anti-ambipolar" behavior and formation of a PN junction by electrostatic doping. Under illumination of a 5μW green laser, the device was found to exhibit an estimated PCE of 0.015 %. We found that such a low value of PCE can be attributed large lateral resistance and low photocurrent.

Subsequently, we investigated a modified structure in which the lateral resistance is minimized by using multilayer sheets as the contact. We show that considerable enhancement of performance can be achieved in this new device design. We discuss the effect of parasitic resistance on the performance of heterostructure solar cells.

3.2 Methods

WSe_2 flakes were first mechanically exfoliated on a commercial SiO_2/P^{++} Si wafer (with a layer of 285nm SiO_2). Subsequently, a MoS_2 flake was exfoliated on a transparent PDMS stamp and stacked onto WSe_2 via the dry transfer techniques. The as-prepared heterojunction was then patterned with standard e-beam lithography and metalized with Cr/Au (2n/50nm). Finally, a thin flake of hBN is exfoliated on PDMS and transferred on top of the heterostructure to encapsulate the entire device. HBN encapsulation layer is used to isolate the sensitive device from unintentional doping effects of air. The device was annealed at 150 ºC in N_2 filled glove box to remove possible adsorbates before measurements. Figure 3.1 (a) shows the schematic of an hBN encapsulated WSe_2-MoS_2 heterojunction device with source, drain, and gate electrodes. Optical image of one of the complete device is presented in Figure 3.1(b).

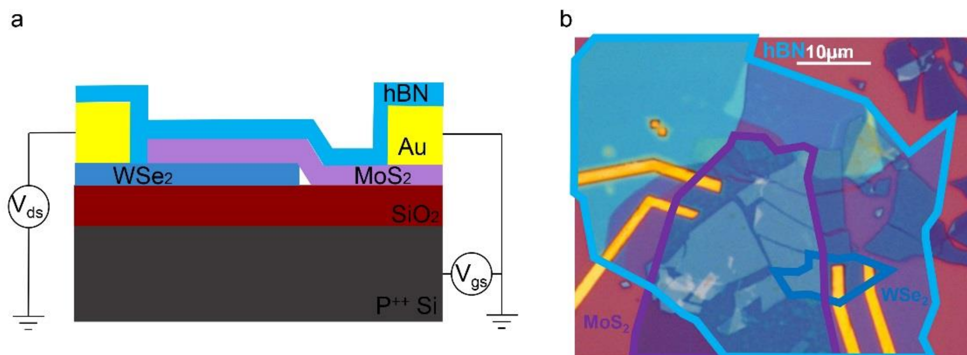

Figure 3.1 (a) Schematic of a multilayer WSe_2-MoS_2 heterojunction; (b) optical image of an hBN encapsulated WSe_2-MoS_2 heterojunction; WSe_2 flake is highlighted with the dark blue line, while the violet line indicates the position of MoS_2 flakes. The entire junction is encapsulated with hBN marked by the light blue line. The scale bar is 10um.

The electrical properties of the device were initially characterized in N_2 filled glove box with an Agilent B1500A module. Subsequently, the device was wire-bonded to an in-house chip-carrier and mounted onto a Janis vacuum cryostat with an optical window. Measurements were conducted at pressures of around 10^{-5} Torr. Blue (473 nm) and green (532 nm) lasers were used to test the opto-electrical response of the device. The laser was focused on the device through a 50x objective lens and its power was adjusted using a neutral density filter. The *I-V* characteristics were measured using Agilent B2902A.

3.3 Results and discussions

3.3.1 PL mapping of 1L MoS_2-1L WSe_2 heterojunction

PL mapping is utilized to probe the electronic structure of MoS_2-WSe_2. Single layer MoS_2 and WSe_2 are taken advantage of thanks to their strong PL intensity. Figure 3.2 (a) shows the PL mapping of a monolayer MoS_2-WSe_2 hetero-bilayer under 473 nm laser excitation. As can be seen, both single layer MoS_2 and WSe_2 regions exhibit bright optical gap emission. On the other hand, the emission from the overlapping region is significantly weaker. The PL spectrum collected from the junction area is plotted in Figure 3.2(b). The two main peaks around 1.67 eV and 1.87 eV correspond to the optical gap emission of monolayer WSe_2 and MoS_2. According to the band diagram given by Kang et al,[54] monolayer MoS_2 and WSe_2 form a type II band alignment. Upon optical excitation, photo-generated carriers are expected relax to energy minima that are in two different layers for electrons and holes. This involves interlayer charge transfer and corresponding loss of intralayer excitons. Thus this interlayer charge transfer process is believed to account for the observed quenching of PL in the hetero-bilayer region. Further, a small peak at a lower energy of around 1.46 eV can be identified. This lower energy peak can be attributed to interlayer excitonic transition across the stagger gap, according to earlier reports.[56, 58]

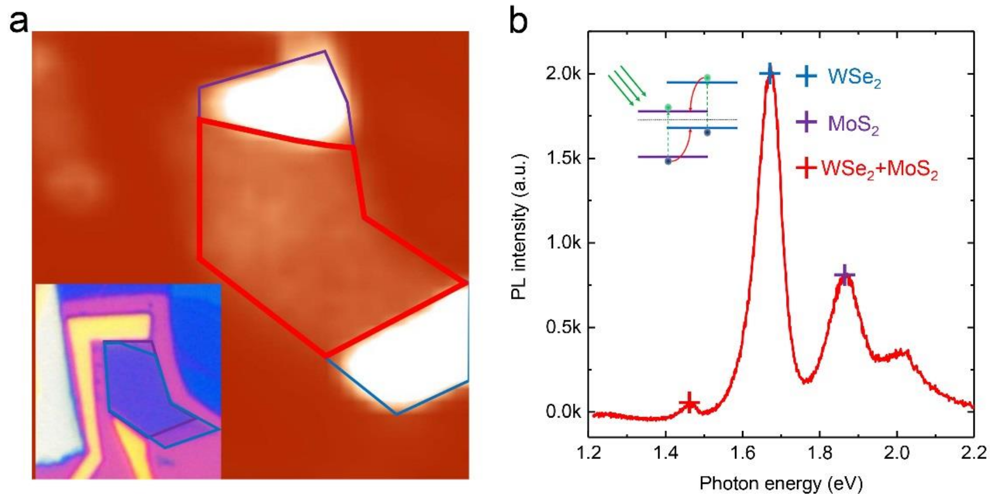

Figure 3.2 (a) PL mapping of a 1L MoS_2-1L WSe_2 heterojunction excited by a 473nm laser. The inset shows the optical image of the device. 1L MoS_2 and 1L WSe_2 are marked by the violet and blue line, respectively. (b) PL spectrum at the interface of heterojunction. Two main peaks are ascribed to exciton emission of single WSe_2 and MoS_2, a lower energy peak is probably due to indirect transition of majorities in separate layers. The inset shows the typical photo-generated carrier transfer process in a type II heterojunction.

3.3.2 “Anti-ambipolar” behavior of hetero-multilayer

Despite the direct band gap of monolayer, the total light absorbance of monolayer is lower than multilayer. Below, we present our findings on the heterojunctions consisting of multilayers. Figure 3.3 (a) illustrates the I_{ds}-V_{gs} relationships of multilayer MoS_2, WSe_2 and their hetero-structure at a fixed voltage of 1 V. A threshold voltage of -40V together with the large current density reveal that hBN encapsulation is effective in isolating TMDs layers from the unintentional P-type doping by ambient molecules. Furthermore, the transfer curve of the hetero-multilayer demonstrates an “anti-ambipolar” behavior.

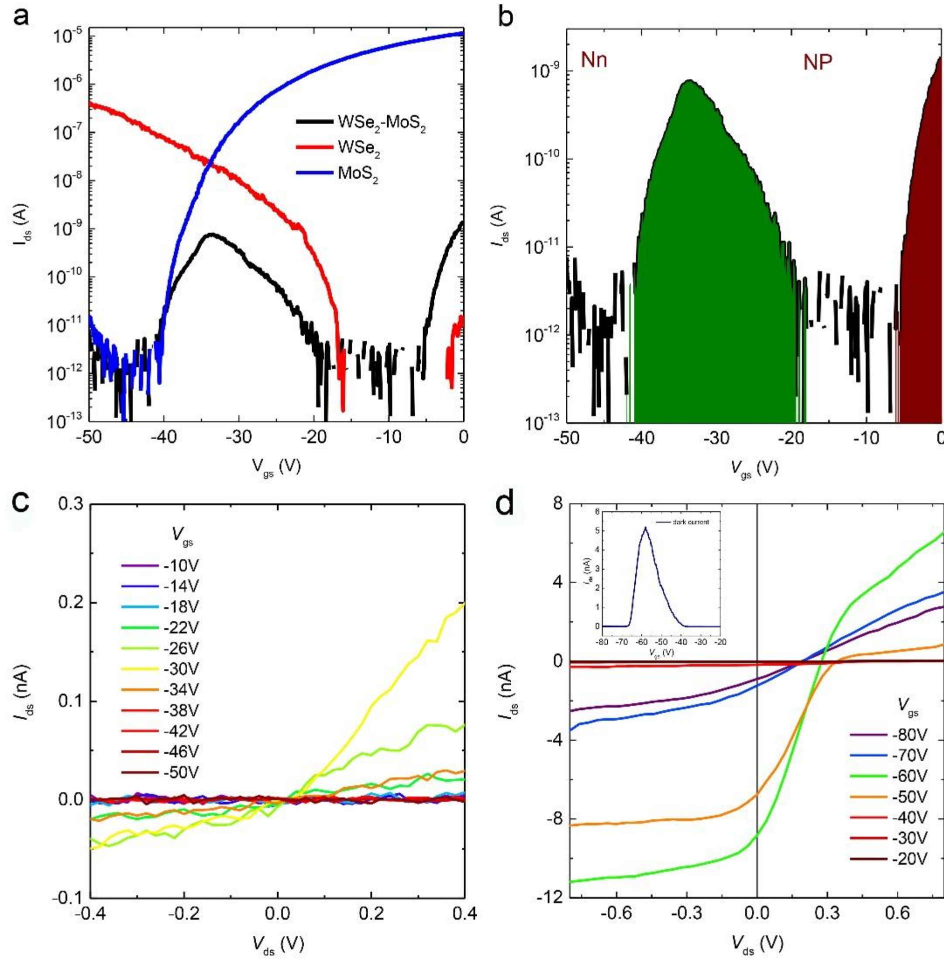

Figure 3.3 (a) Transfer curves of single MoS_2 transistor (blue), single WSe_2 transistor (red) and the MoS_2-WSe_2 heterojunction (black). V_{ds} is fixed at 1V. (b) Illustration of a Nn zone and np zone based on the interpretation of gate dependence. (c) I_{ds}-V_{ds} under different gate voltages in the dark. (d) Photovoltaic effect of the hetero-multilayer as a function of gate voltage under the excitation with a 5μW green laser.

When the bottom gate modulates carrier density of both MoS_2 and WSe_2 simultaneously, electron and hole densities in the two layers are modulated with opposite trends. The forward current, consisting of both electron and hole diffusion current, varies according to the change of carrier densities and reaches the maximum when bother layers are in the conducting state. In other words, MoS_2 and WSe_2 contribute together to the total resistance of the heterojunction and only when both layers are turned "on" does the heterojunction exhibit significant current. There are two conditions

when this occurs. First, the device current reaches a maximum when MoS_2 is n-doped and WSe_2 is p-doped. In this way, a pn hetero-diode is established, as highlighted by the green shade in Fig Figure 3.3(b). Besides the pn regime, there exists another regime where the device is in a conducting state. This is shown as the Nn region shaded with dark red in Figure 3.3 (b). ("N" denotes heavy n-doping and "n" represents weak n-doping) In this regime, MoS_2 is heavily electron doped and WSe_2 is weakly electron doped. Rectifying output characteristics are observed in the np regime as shown in Figure 3.3 (c). In the following, we discuss the photovoltaic effect of the hetero-multilayer in the PN regime.

The photovoltaic effect is examined with the excitation by a 5μW monochromatic green laser. The current-voltage characteristics under illumination is shown in Figure 3.3(d) as a function of gate voltage. We estimate the highest PCE (P_{el}^{max}/P_{in}) to be around 0.0148 % at a gate voltage of -60V. Interestingly, we find that the I_{ds}-V_{gs} curve shifts to the negative direction, implying photo-induced N-doping.

It is noteworthy that at the PN regime, the heterojunction exhibits bad diode behaviors. The highest ratio between forward and reverse current is around 4 times. The forward current is in the order of sub-nanoampere. This low carrier density severely limits the performance of these devices. Below we discuss the possible origin of high device resistance and demonstrate an improved device based on a modified hetero-multilayer structure.

3.3.3 Hetero-multilayer solar cell with a modified structure

3.3.3.1 Modification of device structure

We consider that the low current density originates from limited conducting regime overlap of the MoS_2 and WSe_2 layers. That is, the device exhibits high resistance when either one of the material is in the off state for a given gate voltage. Due to the lateral electrode design, high resistance of each layer adds up in series. As highlighted by the red frame in Figure 3.4 (a), under high negative gate voltage, non-overlapping region of MoS_2 exhibits large sheet resistance.

An effective way to reduce the resistance of non-overlapping region is to place the metal contact directly on the overlapping area. However, this leads direct vertical tunneling of holes through the very thin MoS_2 layer. By inserting a thick layer of MoS_2, the probability of direct tunneling through the layers can be reduced. Schematic of the modified structure is shown in Figure 3.4 (b). Figure 3.4 (c) presents the optical image of one hetero-multilayer with the modified structure.

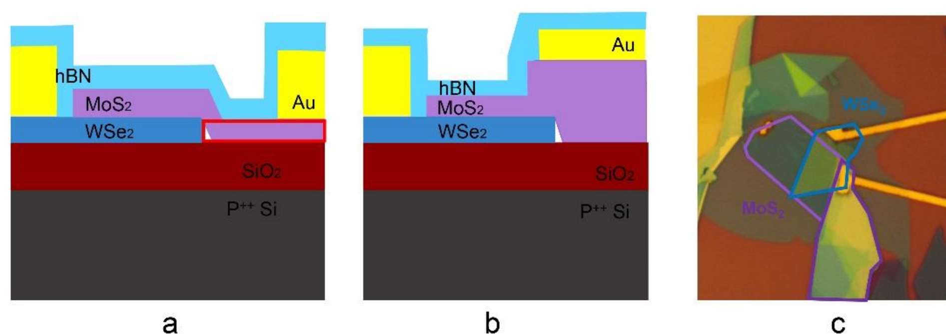

Figure 3.4 (a) the red frame highlights the gate-dependent resistance which limits the current density of the heterojunction (b) Modification of device structure. A thick layer of MoS_2 is utilized to contact the bilayer MoS_2. (c) Optical image of a heterojunction with the modified structure.

3.3.3.2 $I_{ds} - V_{gs}$ and I_{ds} - V_{ds} characteristics

Figure 3.5(a) presents the electrical characterization of source-drain current as a function of gate voltages for the same device shown in Figure 3.4(c). Unlike the “anti-ambipolar” behavior in the previous structure, the new structure exhibits ambipolar-like gate dependence. For this measurement, N-type MoS_2 is grounded and a constant bias of 1V is applied to the bottom WSe_2 layer. As the gate voltage decreases from 0V to -60V, the source-drain current decreases accordingly, indicating electron-dominant conduction. It is noteworthy that multilayer WSe_2 transistor generally shows ambipolar gate dependence with slightly electron-dominant conduction (red curve in Figure 3.3(a)). This reveals the formation of a MoS_2-WSe_2 Nn heterojunction, which is more strongly electron-dominant than the trend in Figure 3.3. Below -60V, the trend is reversed and the device current increases with decreasing gate voltage. Meanwhile, the portion of the curve below V_{gs} = -60V is quite similar to the hole branch of the red curve in Figure 3.3 (a). It is worth noting that the device does not exhibit an off state unlike the previous one. This suggests that the electron density in MoS_2 is not depleted by the gate electrical field due to screening by bottom WSe_2 Therefore, the top MoS_2 flake could be considered as an electron channel with weakly variable resistance.

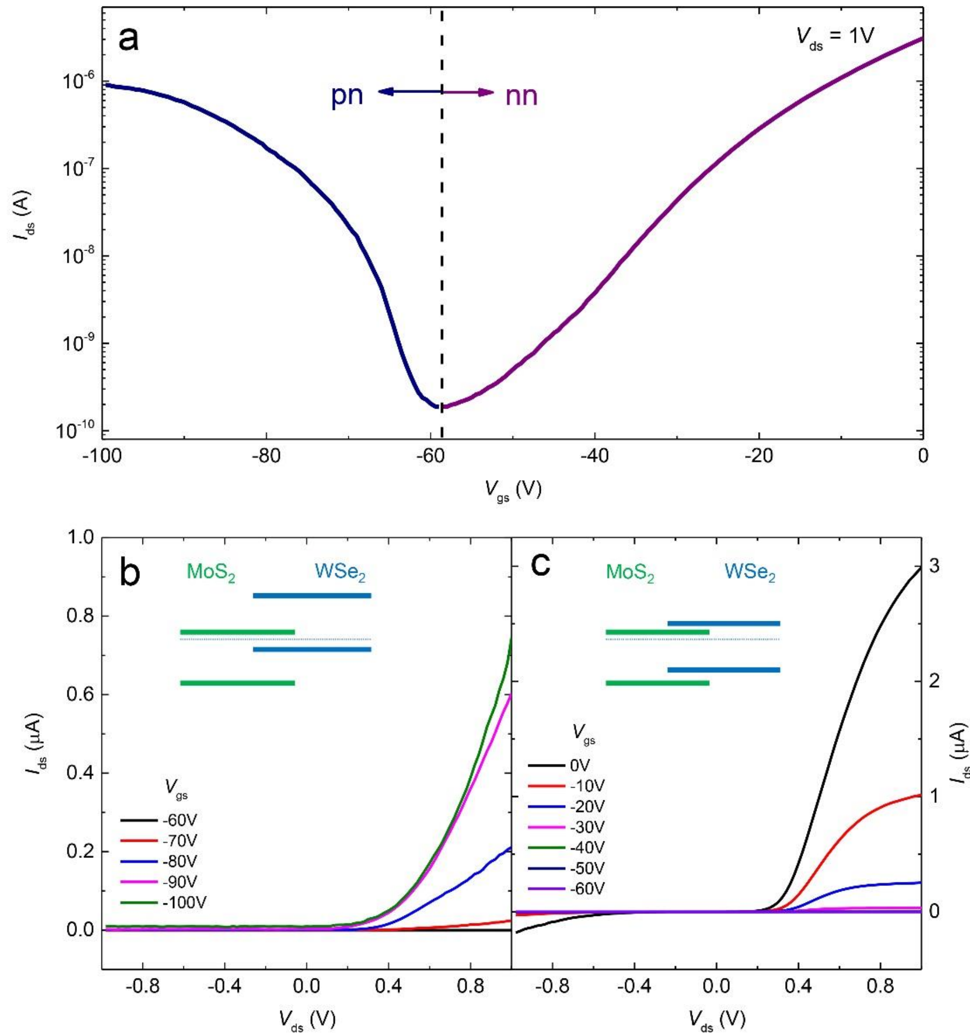

Figure 3.5 (a) I_{ds} – V_{gs} relationship (V_{ds} = 1V). The ambipolar-like gate dependence demonstrates the formation of nn and pn junction at different gate voltages. (b) IV curve at the pn regime with a gate voltage ranging from -60V to -100V. (c) IV curve at the nn regime with a gate voltage ranging from 0V to -60V.

As MoS_2 exhibits constant n-type conduction, the gate dependence reveals the formation of an nN junction and a pN junction in two regimes, with a turning point around V_{gs} ~ -60V. The gate-dependent conduction can be described by the band structure shown in Figure 3.5(b) and (c). The semiconducting behavior of WSe_2 changes from N-type (Figure 3.5 (c)) to P-

type (Figure 3.5 (b)), while MoS_2 remains in the N-doped regime. We believe that the gate field primarily alters the Fermi level in WSe_2, while the shift of Fermi level in MoS_2 is comparatively smaller due to large thickness of the layers and screening effects arising from free carriers in WSe_2.

In both nN and pN regimes, the heterojunction exhibits diode-like conduction, with high ratio between forward and reverse current. Figure 3.5(b) shows the IV curve in the pN regime at gate voltages below -60V. The increase of forward current with decreasing gate voltage reflects effective tuning of hole density by electrostatic doping. On the contrary, the forward current in the nN regime decrease with gate voltage (Figure 3.5(c)).

3.3.3.3 Photovoltaic effects and photocurrent generation

IV curves of the hetero-multilayer in the PN regime as a gate voltage of -100V in the dark and under illumination are shown in Figure 3.6 (a). The device in the dark shows excellent rectification with a rectification ratio of above 10^3. Upon illumination of focused 532nm laser at a power of 6.328μW, the device exhibits significant photovoltaic effects with an I_{ds} around 0.4μA and a V_{oc} around 0.5V The output power P_{el} ($P_{el} = V_{ds} \cdot I_{ds}$) as a function of V_{ds} is presented in the inset, with a maximum value of 67nW. The maximum output power occurs for $V_{ds} \sim 0.24$V. The power conversion efficiency ($\eta = P_{el}^{max} / P_{in}$) is estimated to be around 1.06%. The external quantum efficiency ($EQE = (I/q) / (P_{in}/h\nu)$) is determined to be around 14.8% at a V_{ds} of -1V. We ascribe the strong enhancement of PCE and EQE to the significant reduction of lateral resistance in the modified structure.

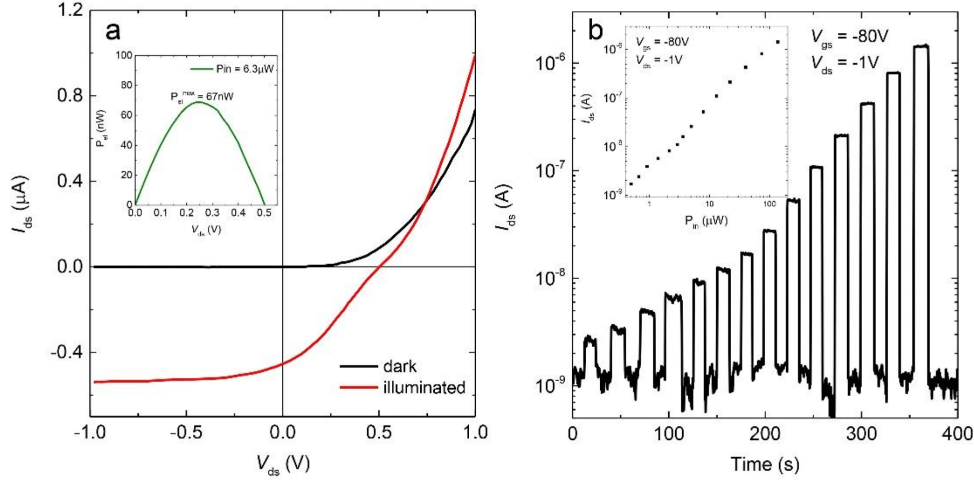

Figure 3.6 (a) IV curves of the device at a gate voltage of -100V in the dark and under illumination. The excitation power is 7.9μW. The inset shows the P_{el} as a function of V_{ds}. (b) Photo response as different excitation powers when the device is negatively biased. The inset plots out the relationship of photocurrent as a function of incident power.

The time-dependent response of photocurrent generation at different excitation power is shown in Figure 3.6 (b) (V_{gs} = -80V and V_{ds} = -1V). The rise time of the photocurrent is lower than 0.1s, since the interval between two measurements is set to be 0.1s. We show in the inset of Figure 3.6 that photocurrent increases linearly with incident power. The photoresponsivity at an excitation power of 0.4uW is estimated to be 4.25mW/A.

3.3.3.4 Gate dependence

The gate dependence of short circuit current (I_{sc}) and open circuit voltage (V_{oc}) is plotted in Figure 3.7 (a) and (b), respectively. Unlike the linear relationship of photocurrent I_{ph}, I_{sc} exhibits a sub-linear relationship with the incident power and tends to saturate at high incident power (Figure 3.7(a)).

On the other hand, V_{oc} increases linearly with log(P_{in}). Given the relationship between V_{oc} and I_{ph}:

$$V_{oc} = \frac{nkT}{q} \ln(1 + \frac{I_{ph}}{I_o}),$$

where n is the ideality factor, k is the Boltzmann constant, I_{ph} is the photocurrent and I_o is the dark current. Given the linear power dependence of I_{ph} (Figure 3.6(b)), V_{oc} is expected to demonstrate linear dependence on ln (I_L) and thus ln (P_{in}).

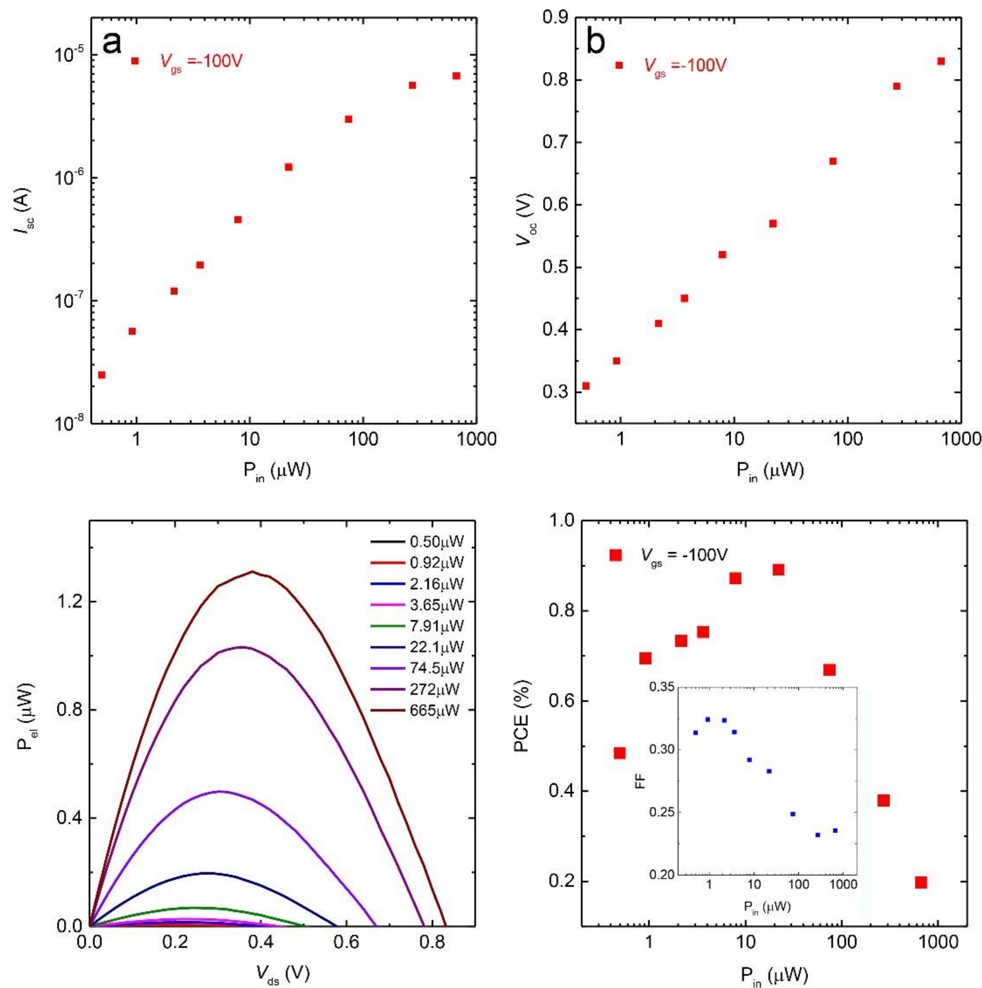

Figure 3.7 (a) Short circuit current and (b) open circuit voltage as a function of incident power. (c) P_{el} as a function of V_{ds} under different excitation power. (d) Power conversion efficiency (PCE) as a function of P_{in}. The inset shows the FF as a function of P_{in}

The output powers as a function of V_{ds} at different excitation power is shown in Figure 3.6(c). The maximum electrical power, labelled as P_{el}^{max}, increases sublinearly with excitation power. The power conversion efficiency ($\eta = P_{el}^{max}/P_{in}$) at a fixed gate voltage of -100V is given in Figure 3.7(d). Despite the increase of P_{el}^{max} with P_{in}, the PCE does not show a linear increase with P_{in}. Instead, it increases with P_{in} at low incident power and then falls at high excitation power. Meanwhile, FF decreases with increasing P_{in} (the inset of Figure 3.7 (d)). Based on the equation $\eta = I_{sc} \cdot V_{oc} \cdot FF/P_{in}$, the trend of PCE with P_{in} could be ascribed to both the sublinear power-dependence of I_{sc} and the decrease of FF with increasing P_{in}.

Besides, as the gate voltage decreases, the IV curves of the solar cell evolve from a quasi-rectangle shape to a quasi-triangle shape (Figure 3.8 (a)), which indicates the decrease of filling factor (FF) with decreasing gate voltage. The FF as a function of gate voltage at an excitation power of 665μW is given in Figure 3.8 (b). The gate dependent FF exhibits an abrupt change near V_{gs} ~ -60V, which coincides with the voltage at which the device transition between nN and pN regimes.

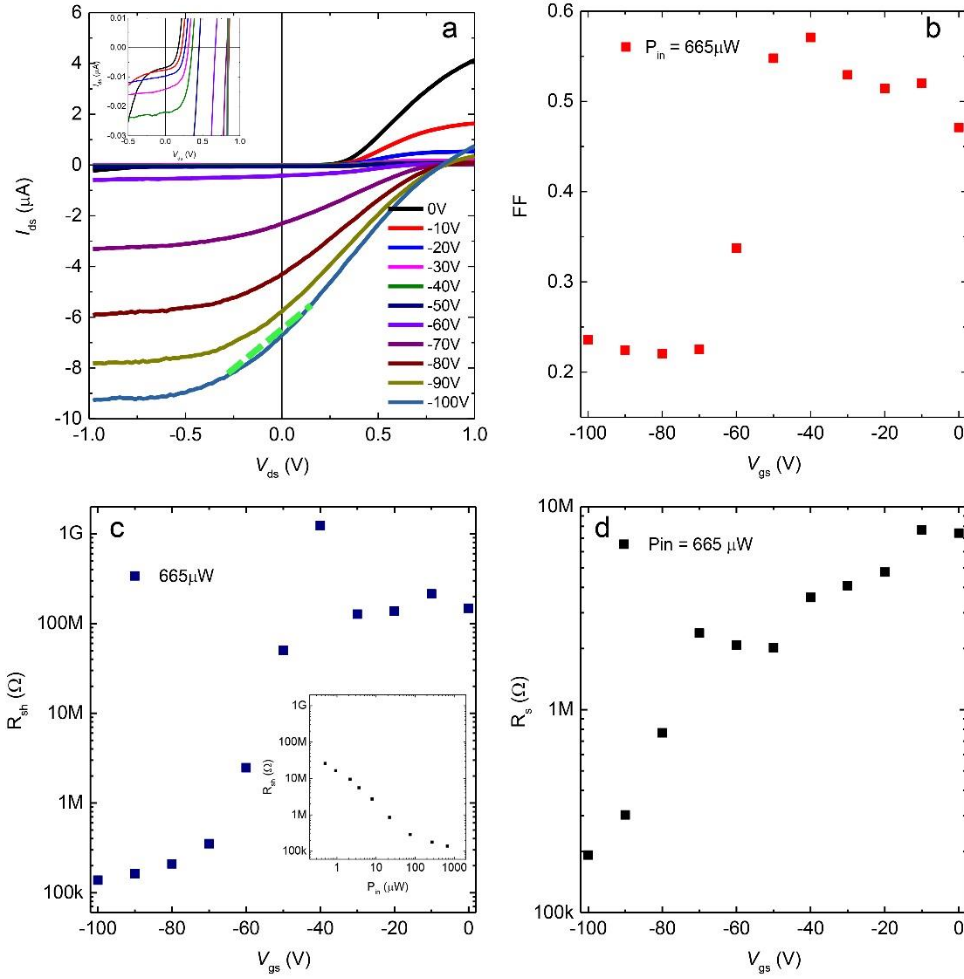

Figure 3.8 (a) IV characteristics at different gate voltages with the excitation of a 665μW green laser. The inset shows the zoom-in picture around the original point. (b) Filling factor as a function of gate voltage. (c) Shunt resistance of the hetero-multilayer as a function of gate voltage under different excitation power. The inset shows that R_{sh} decreases with increasing P_{in}. (d) Series resistance as a function of gate voltage under the excitation of 665μW green laser.

It is known that parasitic resistances, such as parallel shunt resistance R_{sh} and series resistance R_s, have an significant impact on FF. R_{sh} and R_s can be roughly approximated by the inverse of the slope of IV curves at the point of I_{sc} and V_{oc}, respectively.[102] In general, for an ideal solar cell, R_{sh} should be as large as possible so that there is no other leakage paths for photocarriers while R_s should be close to zero, so that output power loss is minimized. R_{sh}

and R_s as a function of gate voltages under different excitation powers is plotted in Figure 3.8 (c) and (d). We found that the gate voltage strongly affects R_{sh}, resulting in an increase by 3 orders of magnitude with increasing V_{gs} under an excitation power of 665μW. Besides, the sharp decline of shunt resistance occurs around the turning point (-60V) of P-type and N-type semiconducting behavior of WSe_2. Further, R_{sh} decrease substantially with increasing excitation power. (Inset of Figure 3.8(c)) Both of them indicates that the shunt resistance decrease rapidly with increasing hole density, which may be due to the decrease of tunneling resistance through the thick MoS_2 layer as the hole density in WSe_2 is enhanced. R_s also decreases with decreasing gate voltages, even comparable to the value of R_{sh} at a gate voltage of -100V. This is most likely the origin of the low FF at high negative gate voltages. In addition, the decrease of R_s with decreasing gate voltages may be ascribed to the reduced contact resistance by electrostatic doping.

3.4 Conclusion

In this chapter, we investigated on the electrical and optoelectronic properties of a hetero-stacking of MoS_2 and WSe_2. We found that PL mapping of monolayers is significantly quenched and a new low energy peak emerge at the heterojunction. These observations are consistent with the recently reported results by several other groups and indicate the formation of type II band alignment at MoS_2-WSe_2 hetero-interface. We further prepared heterojunctions consisting of multilayer MoS_2 and WSe_2 flakes and found that such structures exhibits "anti-ambipolar" behaviors with clear photo response. This device was found to exhibit low current density in the order of sub-nanoampere and a maximum power conversion efficiency of 0.0148%. We attribute the performance of this device to the low doping concentration in the separate layers and high lateral resistance.

We further investigated an improved device structure by the insertion of a multilayer MoS_2 between the contact and WSe_2. This device structure demonstrates an ambipolar gate dependence and significantly improved I_{sc} due to the reduced lateral resistance. PCE was found to be strongly dependent on V_{gs} and illumination power. The highest PCE of our solar cell is estimated to be around 1%. Finally, we discussed the effect of parallel shunt resistance and series resistance on FF. Gate dependent R_s and R_{sh} suggests that the optimal operation condition of this type of device is non-trial and is determined by the competition between power loss by series resistance and leakage current in the high doping regime.

4 Highly Efficient Electroluminescence from Ultrathin Field Emission Diodes

4.1 Introduction

In the family of two dimensional materials, monolayer TMDs, such as MoS_2 and WS_2, stand out as they possess a direct band gap and are able to host stable band gap excitons that exhibit robust electronic[103] and valley[104] coherence. Due to quantum confinement of carriers and reduced dielectric screening in the ultrathin limit, excitons and their complexes in monolayer TMDs are tightly bound and mediate strong light matter interaction in resonance conditions[105, 106, 107]. The binding energy of neutral excitons at room temperature in monolayer TMDs is much higher than that in commonly known semiconductors, like group III-V compound. These features allow observation of exciton polaritons [108, 109] and offer prospects for the development of room-temperature polariton lasers as well as exploration of exotic condensed matter phases[110].

One essential step towards the realization of novel photonic devices based on 2D semiconductors is to achieve planar emission with high quantum efficiency by electrical excitation. A vertical structure is desirable for the implementation of planar emission in the whole device area. Heterojunction consisting of an intrinsically n-type MoS_2 and P-type silicon have shown good rectification and electroluminescence from the entire interface area.[68] However, only a small fraction of current contributes to the formation of exciton, since the bandgap of monolayer MoS_2 is much larger than that of silicon. To date, electroluminescence of light emitting devices based on

monolayer TMDs have shown external quantum efficiency that falls far below 10 % [60, 72, 73, 111, 112, 113, 114, 115, 116]. The challenges are mainly two folds: low current-to-exciton conversion efficiency and low quantum yield of excitonic luminescence. Previous studies indicate that injected electrons and holes have low probability of forming a bound state during its transit across the active layer. This issue has been partly addressed by employing judiciously designed vdW hetero-stacks, which, by mimicking the conventional multi-quantum-well (MQW) structure, was found to allow enhanced carrier injection and improved probability of exciton generation [73]. However, EQE of these devices is still limited by large leakage current and low emission QY, which is evident from the high turn-on current density ($> 0.5\ \mu A \cdot \mu m^{-2}$) and low PL QY ($< 10$ %) of these materials [117]. Moreover, stacking multi-quantum-well heterostructure by repeating the dry transfer process considerably adds to the difficulties in preparing high quality and clean samples with less bubbles and defects. On the other hand, the quantum yield of excitonic luminescence is mainly dependent on the quality of the sample, while the current-to-exciton conversion rate could be enhanced by judicious design of device structure. For the existing device structure, the current-to-exciton conversion rate is, to a great extent, limited by large leakage, namely the wasted current. In the best scenario, every hole injected into the intrinsic n-type monolayer TMD is anticipated to be made full use of and form an exciton. Here, we report observation of highly efficient light emission from tunnel diodes based on metal-insulator-semiconductor (MIS) vdW heterostack prepared by dry transfer technique[118]. These diodes consist of a FLG electrode, hBN tunnel barrier layer, and an electrostatically gated monolayer WS_2 layer (Figure 4.1

(a)). They are found to exhibit stable planar EL with ultra-low turn-on current density of 4 pA·μm^{-2}, which is orders of magnitude lower than that of the best EL device reported to date [119]. Besides, the devices exhibit exceptionally high external quantum efficiencies (EQE ~ 13 %) that unexpectedly exceed photoluminescence (PL) quantum yield (QY) by more than one order of magnitude. We propose that the light emission is probably triggered by injection of energetic minority carriers by Fowler-Nordheim tunneling and that the boost in quantum efficiency is most likely attributed to carrier multiplication effects. Our findings highlight the possibilities of exploiting impact ionization effects in 2D semiconductors for realizing light emitting devices with efficiencies exceeding 100 %.

4.2 Materials and Methods

Device preparation WS_2 crystals were grown by chemical vapor transport (CVT) method using I_2 as the transport agent. Monolayer WS2 flake was exfoliated on a silicon substrate with a 285 nm thick silicon oxide layer. Thin flake (4 ~ 7 nm) of hexagonal boron nitride (hBN) was exfoliated from a commercial hBN powder (Momentive) onto PDMS surface and then transferred on top of monolayer WS_2 using a standard dry transfer technique.[118] Few-layer graphene (FLG) having thickness of 3 ~ 5 nm was similarly exfoliated on PDMS and then transferred on top of the hBN layer, leaving a part of bare WS_2 uncovered for electrical contact. A standard electron beam lithography was used to pattern electrodes onto the WS_2 and FLG layers. Cr/Au (2 nm/50 nm) electrodes were deposited by thermal evaporation.

Characterization All measurements were conducted in a liquid-nitrogen-cooled Janis cryostat in vacuum (~10^{-5} Torr). Electrical measurements were conducted using Agilent source/measure unit (B2900A) and a parameter analyzer (B1500A). EL and PL signals were collected through a 50× object lens of a laser confocal microscope (NT-MDT), typically at an integration time of 1s. For PL, 473 nm excitation laser was used.

Estimation of PL quantum yield and EL external quantum efficiency

In order to obtain the absolute PL quantum yield (QY: for WS_2, we define this as the percentage of photons emitted from the heterostack per photons absorbed by WS_2) and EL external quantum efficiency (EQE), we used a commercial organic dye ($C_{58}H_{49}BN_2S_4$ = 5,5'''-Bis(N,N-dipenylamino)-4'-dimesitylboryl-2,2':5',2'':5'',2'''-quaterthiophene) dispersed in PMMA matrix

as a reference sample. The reference sample was provided by Prof. Kazunari Matsuda's group at Kyoto University. In contrast to rhodamine 6G, which exhibits high QY in solution [120] but not in solid thin film form [117], the dye dispersed in PMMA was stable and exhibited QY of ~36 %. [121] The absolute QY of the film could be readily measured in an integrating sphere. Absorption of the thin film was measured in a UV-Vis spectrophotometer as well as in our laser confocal microscope where all EL and PL measurements were conducted. PL of the reference sample and WS_2 was measured in our laser confocal microscope keeping all experimental conditions strictly identical. The PL internal quantum yield of WS_2 was calculated by $Q = Q_R \frac{I}{I_R} \frac{OD_R}{OD}$, where Q_R is the absolute QY of the reference sample, I and I_R are the PL intensity, and OD and OD_R are the optical density of WS_2 and the reference, respectively. Based on this, we estimated the QY of monolayer WS_2 at room temperature to be 0.216 % for excitation power density of 5.35 W/cm^2, which corresponds to a generation rate of 1.81×10^{18} $cm^{-2}s^{-1}$. This PL QY for exfoliated monolayer WS_2 at room temperature is in reasonable agreement with that report by Amani et al [122]. EL EQE was also estimated in a similar manner. We assumed that the collection efficiency was the same for both PL and EL measurements. The collection area for both PL and EL is estimated to be ~3 μm^2 based on our optical system. For all the device measured, the emission area is much larger than 3 μm^2 and the collection spot is located in the center of the device for the measurement.

4.3 Results and Discussion

4.3.1 Basic electrical and optical characterization

The diode characteristics of our MIS devices at room temperature are shown in Figure 4.1 (b). At large positive back gate bias V_g that renders WS_2 n-type conductor, the devices exhibit rectification behavior with a clear threshold in forward bias (the FLG layer is positively biased with respect to WS_2 at ground potential) and rectification ratios of $10^3 \sim 10^4$. The forward bias current (I_d) increases exponentially beyond the threshold bias V_{th} of ~ 5.5 V before saturating at higher voltages (V_d). The dependence of saturation current on V_g indicates that high bias current is limited by the in-plane resistivity of the WS_2 layer (Inset of Figure 4.1 (b)), which could be taken advantage of as overcurrent protection for the tunneling device. On the other hand, the exponential current is independent of V_g, indicating that out-of-plane resistance of the insulating hBN layer limits the device current in this regime.

Above the threshold bias, EL with emission peak near the optical gap of WS_2 (~ 2eV) is observed (Figure 4.1 (c)). Additionally, the intensity of electroluminescence increases with applied bias voltage and tunneling current. The EL signal is stable over time and readily detectable even at sub-nanoampere currents at one-second integration with our CCD (Figure 4.2). Comparing the bight-field optical image and the image of electroluminescence, we find the light emission mostly comes from the overlapping area of graphite-BN-WS_2, which implies that the planar could be ascribed to radiative recombination of tunneled holes from graphite and electrons in WS_2. The emission profile reveals that the EL is spatially uniform

across the WS_2 flake despite the fact that the carriers are supplied by lateral electrodes (Figure 4.1 (d)), which, at the same time, indicates that the tunneling current is uniformly distributed across the heterojunction area.

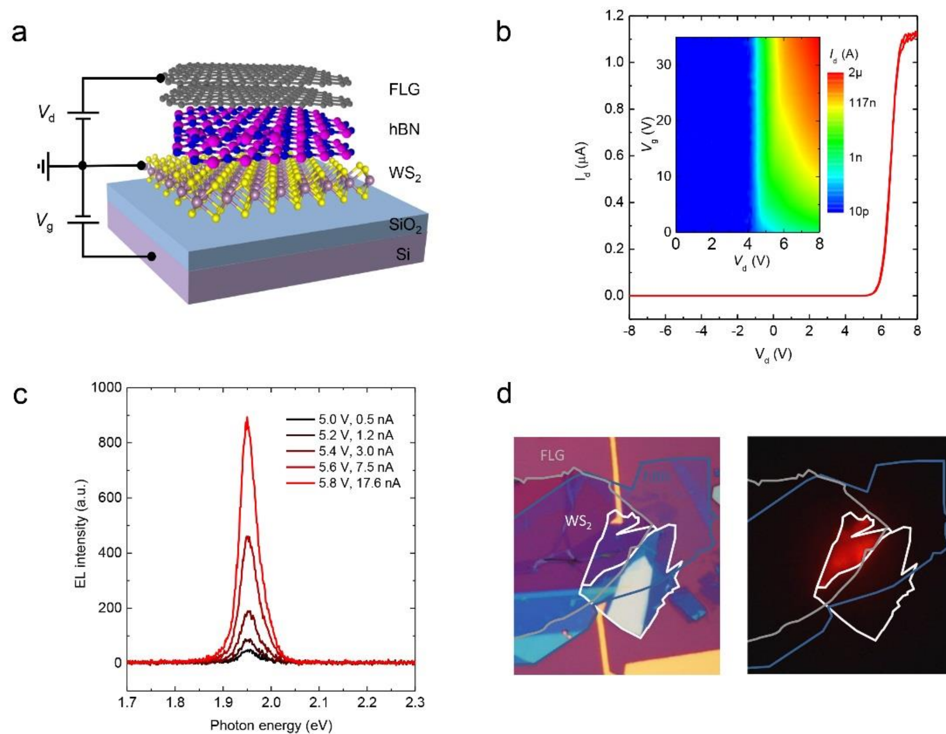

Figure 4.1 (a) Schematic view of FLG/hBN/WS_2 light emitting diode. (b) I_d-V_d characteristic at $V_g = 40$ V. The inset shows the plot of tunneling current as a function of V_g and V_d. (c) EL spectra of the MIS diode at different V_d and I_d at 100 K. (d) Bright-field optical image of the device and image of EL at an injection current of 100 nA at an accumulation time of 2 s. The emission area is ~ 66 μm^2.

In unipolar semiconductors, EL may originate from radiative recombination of majority carriers with minority carriers introduced by injection, impact ionization, or thermal generation. Since the observed EL is sharp and turns on at extremely low current density, we rule out thermal generation of holes. It is also highly unlikely that electrons gain sufficiently high energy for impact ionization due to the small voltage drop in the WS_2 layer. Thus, the emergence of EL from an n-type WS_2 indicates that minority

carriers (holes) are injected from the FLG electrode. Further, as shown in Figure 4.2, the onset of emission coinciding with the rise of diode current above the background level (~ 100 pA) implies that the measured current is purely due to hole injection. Under steady-state conditions, electron density in the WS_2 layer is orders of magnitude greater than the hole density because WS_2 is heavily n-doped by both the Si back gate and the MIS capacitance. A typical transfer curve of monolayer WS_2 transistor with gold contact on silicon wafer is shown in Figure 4.3. The source-drain current is turned on at zero gate voltage and increases with high positive voltage, which represents an N-type conducting behavior. During our measurement, the devices are always positive biased to enhance the electron density in the WS_2 channel. Thus, we anticipate that under a large enough electrical field, majority of holes tunnel through the BN barrier, enter WS_2, bind to an electron and form an exciton. In addition, the sharp steps in Figure 4.2 under various bias manifest the reliability of this special MIS structure, because the tunneling current at a fixed voltage is quite stable.

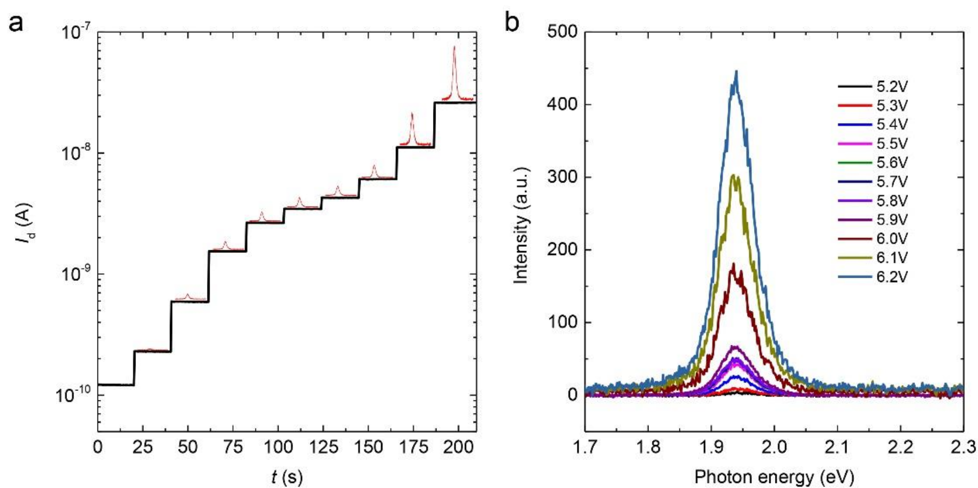

Figure 4.2 (a) Diode current (I_d) vs time (t) plot of a device during increasing steps of applied bias (V_d). The bias was increased from 5.1 V to 6.0 V at 0.1 V step at ~ 20 s interval. EL spectra at different current levels are shown at each step. The background current was ~ 100 pA for this device. EL emerges

immediately above the threshold voltage of 5.1 V, at current of ~ 200 pA. The active area of this device is 37 μm^2. (b) EL spectra under different bias.

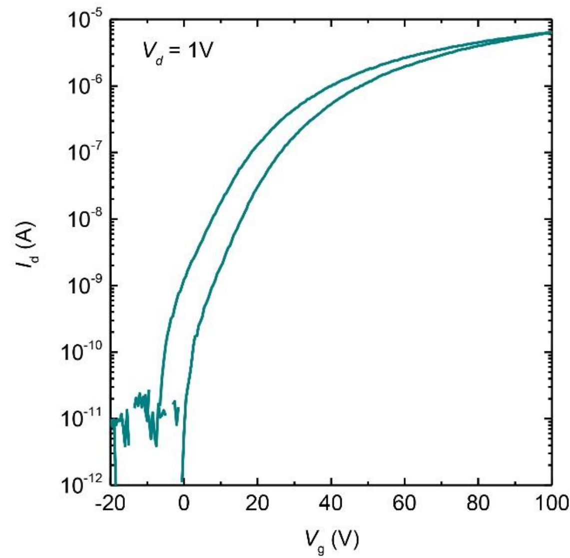

Figure 4.3 Typical transfer characteristics of monolayer WS_2 device at room temperature measured in N_2 atmosphere.

4.3.2 Highly efficient electroluminescence

Using a fluorescent dye dispersed in PMMA as a reference, we estimated the EL EQE of our devices to range from 1.38 to 13.0 % at different bias conditions at 77 K, as shown in Figure 4.5 (b) as the solid circles (See Materials and Methods). On the other hand, the estimated PL QY (defined here for convenience as the number of photons emitted from the heterostack per each photon absorbed by WS_2) from the same WS_2 layer at the same location on the device using CW laser excitation ranged from 0.13 to 0.4 % at different excitation powers. In order to verify this difference between EL and PL efficiencies, we compared the EL and PL spectra at the same electron-hole (e-h) pair generation rate $G_{e\text{-}h}$. For EL, we assume $G_{e\text{-}h} = I_d/eA$ where e is the electronic charge and A is the emission area. For PL, we assume $G_{e\text{-}h}$ = (1-

$A_G)A_W P_{exc}/S\hbar\omega$ where A_G and A_W are absorptance of FLG and WS_2, respectively, P_{exc} is the excitation power, S is the laser spot size, and $\hbar\omega$ is the energy of excitation laser.

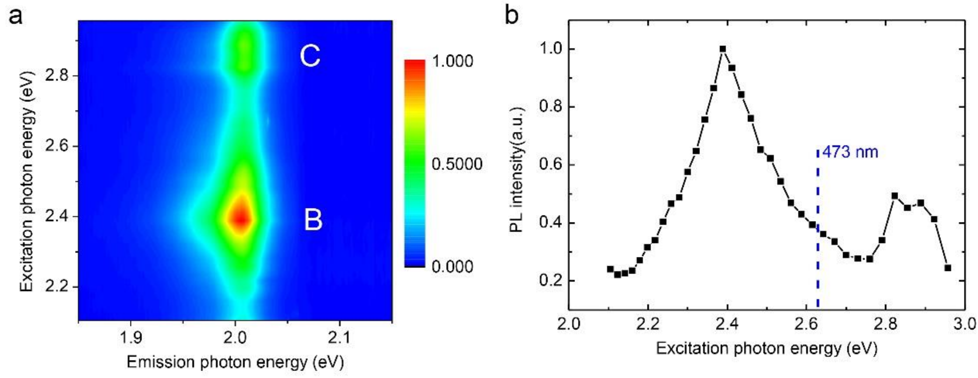

Figure 4.4 PLE spectra of a FLG/h-BN/WS_2/SiO_2/Si heterostack. (a) PLE intensity map and (b) relative PLE spectra based on the integrated intensity of the A peak in the PL spectra at each excitation energy; the excitation laser we used (473 nm) has also been labeled in this figure.

Here, we estimate A_W and A_G to be equivalent to the absorptance of isolated WS_2 and FLG flakes measured on a quartz substrate in transmission and reflection geometry. At 473 nm excitation, we find A_W = 20 % and A_G = 29 %. Note that the actual absorption in these layers in our MIS device is expected to be larger due to multiple reflection effects[123]. Thus, $G_{e\text{-}h}$ and QY values for PL presented here represent the lower and upper limit, respectively. Further we verify from our PL excitation spectroscopy measurements that interference effects do not play a major role in modifying light in-coupling efficiency of WS_2 and FLG layers (See Figure 4.4 for excitation spectroscopy results). Figure 4.5 (a) shows the EL and PL spectra obtained at similar $G_{e\text{-}h}$ above and below the threshold bias, respectively, since above the threshold bias, the PL spectra is a mixture of PL and EL. It is evident that the EL

intensity is substantially greater than the PL intensity, indicating that the external quantum efficiency is correspondingly higher for EL. By plotting all the data collected at a range of $G_{e\text{-}h}$ in Figure 4.5 (b), we find that the enhancement of EL with respect to PL is consistent over more than two decades of $G_{e\text{-}h}$ values. Both EL and PL show decrease in quantum efficiency at very low $G_{e\text{-}h}$, similar to the report by Amani et al.[48, 122], suggesting that Auger-type recombination becomes increasingly dominant at high excitation rates. The origin of apparent saturation at higher $G_{e\text{-}h}$ is not clearly understood.

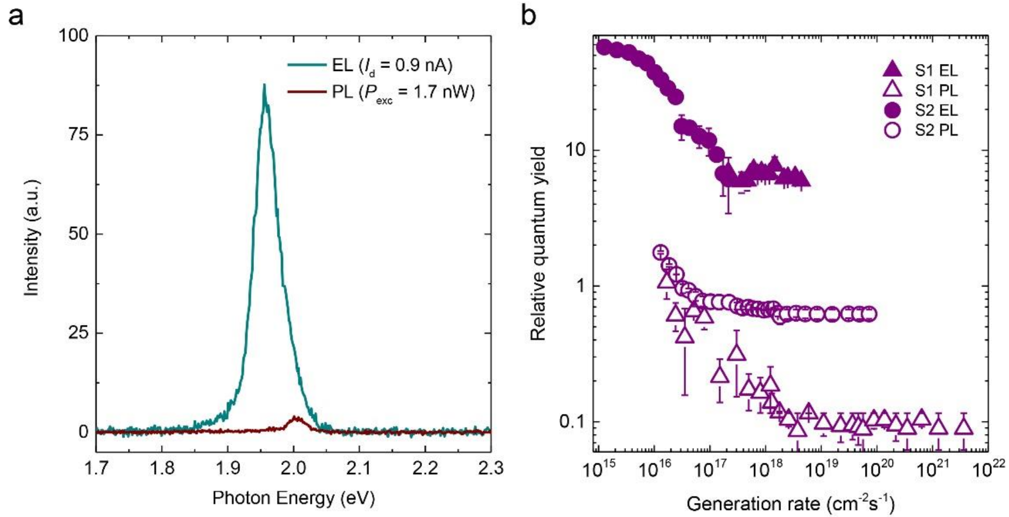

Figure 4.5 (a) Comparison of EL and PL spectra measured at similar $G_{e\text{-}h}$ at 100 K. EL was collected at $I_d = 0.9$ nA, $V_d = 8.4$ V and $V_g = 80$ V. The device area is 16 μm^2. PL was obtained at excitation energy and power of 2.6 eV and 1.7 nW. PL was measured at $V_g = 80$ V and $V_d = 0$ V. $G_{e\text{-}h}$ for EL and PL are 1.8×10^{16} $cm^{-2}s^{-1}$ and 1.9×10^{16} $cm^{-2}s^{-1}$, respectively. (b) Comparison of the relative QY of PL and EL over a wide range of electron-hole pair generation rates. S1 and S2 are two different devices measured at 100 K and 77 K, respectively.

We discuss below the possible explanations for these observations. In steady-state conditions, the output power P of EL and PL can be both expressed as

$$P = \beta\eta\alpha G_{e-h}\hbar\omega \qquad (1)$$

where β is the out-coupling efficiency, η is the quantum efficiency of radiative recombination of ground excitons, and α is the yield of ground excitons for each electron-hole pair generated. Our observation of $P_{EL}>P_{PL}$ for an identical G_{e-h} implies that at least one of the following conditions is true for our devices: $\eta_{EL} > \eta_{PL}$ and $\alpha_{EL} > \alpha_{PL}$. In the following, we consider these two cases.

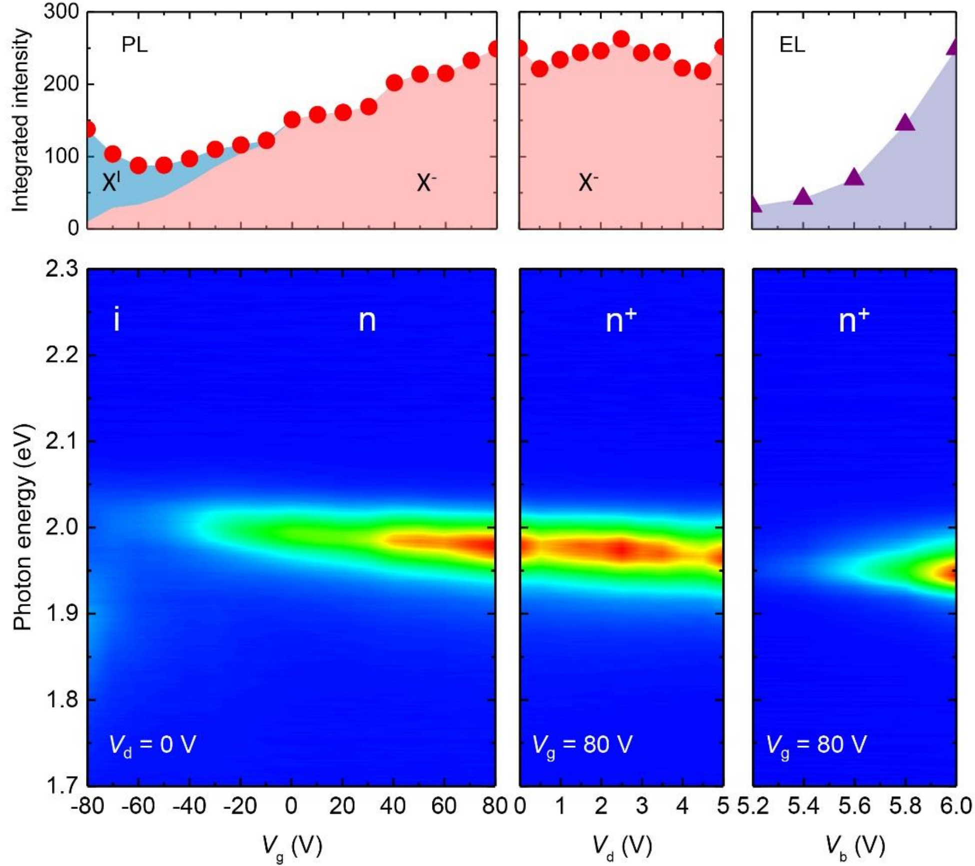

Figure 4.6 PL and EL intensity as a function of V_g and V_d. Left and middle columns show changes in the integrated PL intensity (upper panel) and color-coded spectrum (lower panel) as a function of V_g at $V_d = 0$ (left column) and as a function of V_d at V_g = 80 V (middle column). PL was measured at the excitation energy and power of 2.6 eV and 5μW. X^I and X^- denote emission due to impurities/defects and negative trions, respectively. Right column shows the evolution of EL integrated intensity (upper panel) and spectrum (lower panel) as a function of V_d at $V_g = 0$ V.

It is known that the QY of PL in monolayer TMDs depends on carrier densities due to redistribution of oscillator strengths between excitons, trions, and bound exciton complexes [51, 105]. Figure 4.6 shows the changes in the PL intensity and energy as a function of V_g and V_d. The emission is predominantly due to negatively charged trions (X^-) as it is evident from the characteristic redshift of the peak with increasing carrier density[105]. The total PL QY is nearly constant in the heavily electron-doped regime (n^+) and decreases gradually when the material is depleted of free electrons. EL was observed in the n^+ regime where the emission QY is effectively independent of carrier densities. Thus, the large EL cannot be explained by redistribution of oscillator strengths.

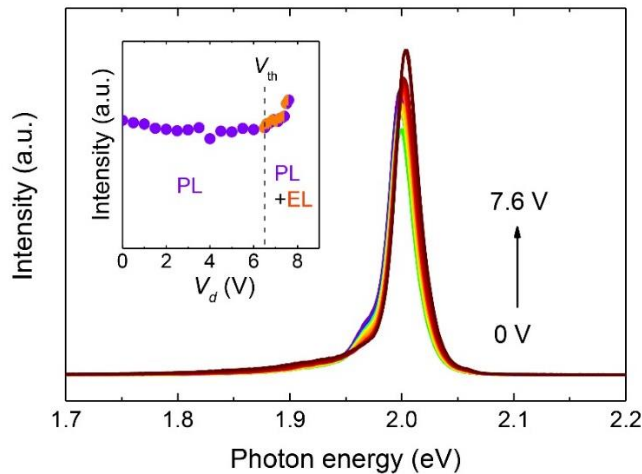

Figure 4.7 PL spectrum as a function of diode bias voltage. The measurements were made below and above the EL threshold V_{th} = 6.5 V. For $V_d > V_{th}$, the spectrum comprises of both the PL and EL signals. Note that there is no evidence of discontinuity in PL QY around V_{th}, indicating that the decay dynamics of ground excitons is neither altered by the diode bias nor current. Note that the PL intensity is greater than the EL intensity due to high optical excitation power (159 W/cm^2) used in this experiment. PL is predominantly due to negative trions, whereas EL is both due to negative trions as well as impurity emission.

Further, we did not observe notable changes in the PL QY below and above the EL threshold as shown in Figure 4.7, indicating that the radiative

and non-radiative decay rates of excitons are not affected by bias or current. EL was often dominantly due to trions but emission from neutral excitons and impurity states were also observed in some devices, as shown in Figure 4.8.

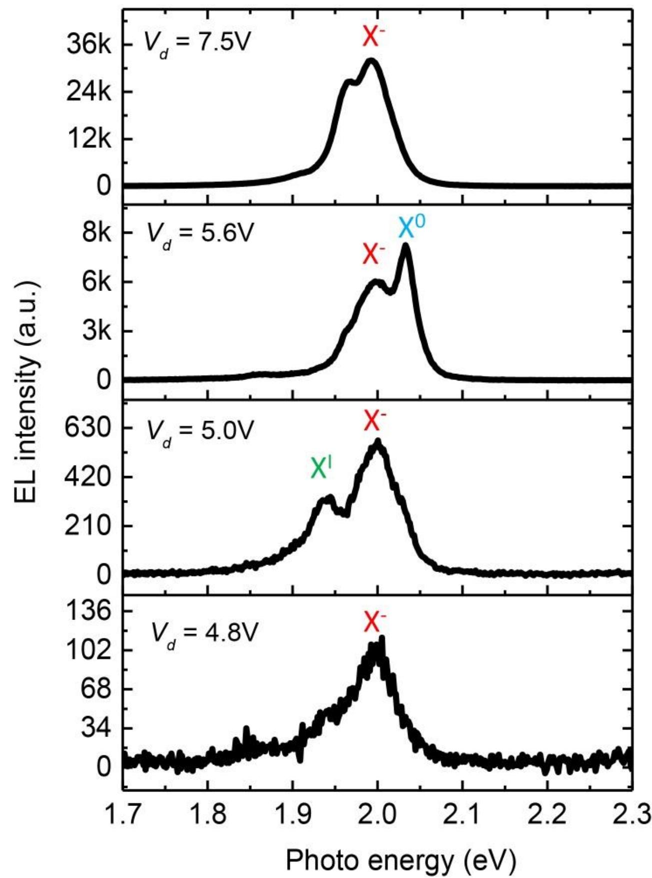

Figure 4.8 EL spectrum of a device exhibiting peaks due to neutral exciton, negative trion, as well as impurity emission.

4.3.3 Impact ionization

Next, we consider the relaxation process that determines the magnitude of α. Due to fast non-radiative recombination processes that compete with carrier cooling[124], α is expected to be below unity for most conditions [125]. This is evidenced by the tendancy of PL QY to decrease with increasing optical

excitation energies[125]. However, sufficiently energetic e-h pairs or free carriers can generate extra e-h pairs by impact ionization of valence electrons. In such a case, more than one ground exciton can be generated for a single energetic e-h pair or free carrier. Therefore, α is a complex function of excess energy and may exceed unity under certain conditions. Our EL devices turn on at voltages significantly exceeding the band gap of WS_2, and thus such hot carrier effects can play a dominant role.

We show in Figure 4.9 (a) that the I_d-V_d characteristics in forward bias can be fitted very well by the Fowler-Nordheim tunneling equation [126] at temperatures ranging from 77 to 240 K. (As the current below threshold is ascribed to noise, the portion of curve below threshold voltage does not fit in.)

$$J = \frac{q^2 (V/d)^2}{16\pi^2 \hbar \phi_{in}} \exp\left[\frac{-4\sqrt{2m^*}(q\phi_{in})^{3/2}}{3\hbar q\left(V/d\right)}\right] = C_4 V^2 \exp(\frac{-C_5}{V})$$

This excellent fit indicates that holes in FLG tunnel into the valence band of hBN where they are subject to very large electric fields of ~1 V/nm. Due to the small thickness of the hBN layer, holes accelerate and ballistically transit into WS_2 as hot carriers. The high energy of injected holes is unambiguously revealed by the emergence of B exciton peak in the EL spectrum, which is 0.4 eV higher in energy with respect to the ground exciton (A) emission (Figure 4.9 (b)). Sketch of the band diagram of unbiased and biased vdW heterostructure (Figure 4.9 (c)) shows that the hot holes have excess energy of approximately $E_{exs} = eV_d - E_g$ where E_g ~ 2.3 eV is the quasi-particle band gap of monolayer WS_2 [127]. Thus, above the typical V_{th} of 4 ~ 6 V, the holes have sufficient energy to ionize valence electrons into the

conduction band or directly generate bound electron-hole pairs. This proposed scenario is also consistent with the observation that the power conversion efficiency of our EL devices also exceeds that of PL (Figure 2a). Since the excitation energy of EL (> 4 eV) is far more in excess of the ground exciton emission energy (~ 2 eV) compared to that of PL (2.6 eV), the power dissipation due to thermal relaxation is expected to be far greater for EL. However, our observation suggests that the input electrical power was not only lost as heat but was efficiently consumed in generating e-h pairs. In contrast, for PL excitation, the excess energy is not sufficiently large to ionize valence electrons and therefore is dissipated only through non-radiative decay processes.

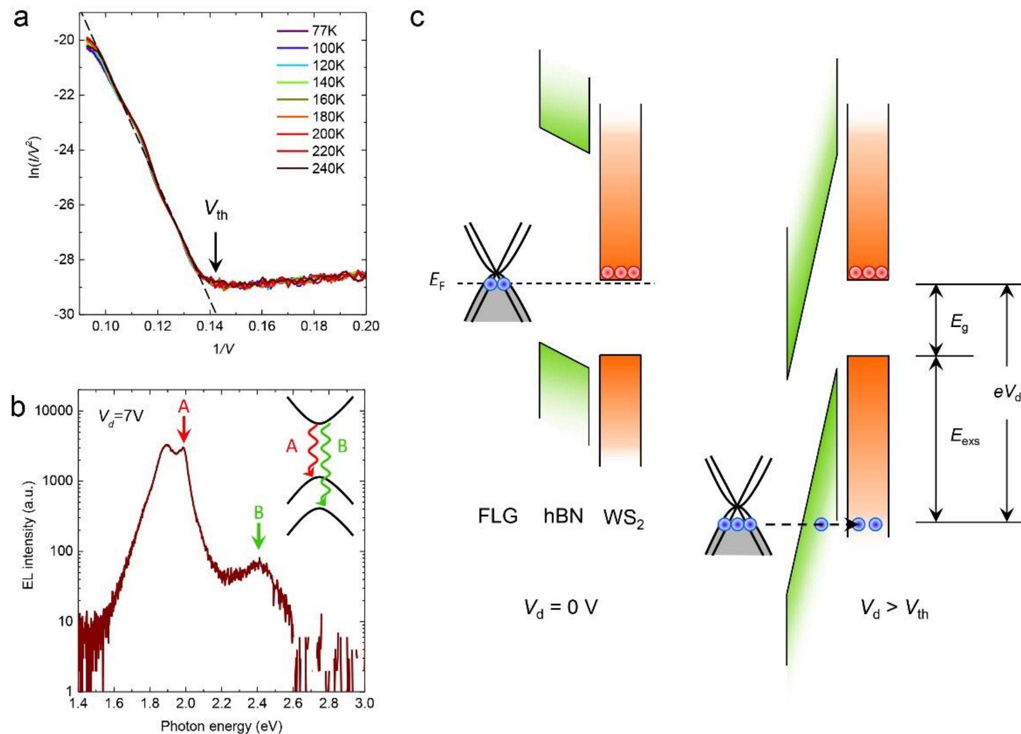

Figure 4.9 (a) Fowler-Nordheim plot of I_d-V_d relationship at temperatures ranging from 77 to 240 K. The turning point in the plot coincides with the threshold voltage (Vth) for light emission. (b) EL spectrum at a high bias voltage (V_d = 7 V). A and B denote emission due to A and B excitons arising from spin-orbit-split valence bands as shown in the inset. (c) Band diagram of the FLG/hBN/WS_2 heterostructure for $V_d = 0$ and $V_d > V_{th}$.

Luminescence in unipolar semiconductors followed by impact ionization is known to occur in conventional semiconductors[128]. Typically, energetic majority carriers are injected and accelerated before ionizing valence electrons and generating e-h pairs. The first EL observed in unipolar monolayer MoS_2 was attributed to such effects[66] . Impact ionization by energetic minority carriers is fundamentally different in that single ionization event results in generation of two e-h pairs or excitons as schematically described in Figure 4.10. Excitation by photons having energy smaller than $2E_g$ yields maximum of a single e-h pair per photon in linear regime (Figure 4.10 (a)) while similarly, impact ionization by energetic majority carriers with $E_{exs} < 2E_g$ yields a maximum of a single e-h pair per carrier (Figure 4.10 (b)). In contrast, energetic minority carriers can excite e-h pairs and also bind with a majority carrier to form extra pairs, thus yielding more than one e-h pair per carrier (Figure 4.10 (c)). Conventional forward-biased MIS-type Schottky light emitting diodes operate on a similar principle of minority carrier injection[129]. However, large majority carrier tunnel current prevents injection of energetic minority carriers at high biases, often severely limiting their efficiencies.

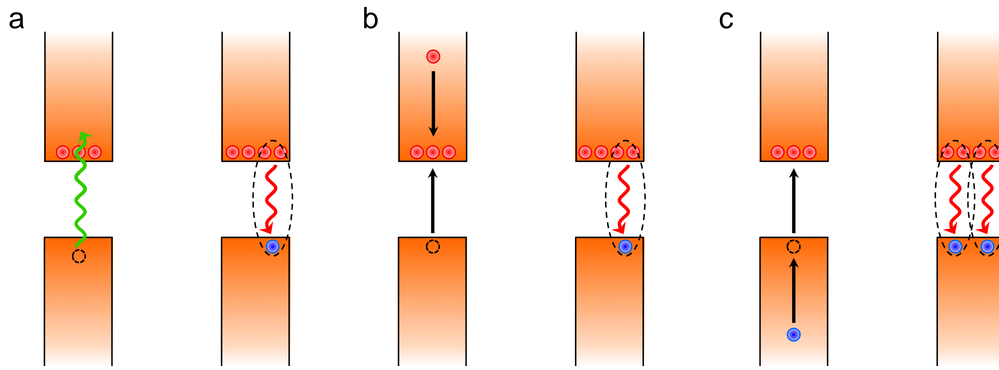

Figure 4.10 Exciton generation mechanisms in n-type WS_2 monolayer. (a) Generation of a single trion and emission following absorption of a photon having energy slightly greater than the semiconductor band gap. (b) Impact ionization by an energetic electron followed by generation of a single trion. (c) Impact ionization by an energetic hole followed by generation of two trions.

4.4 Conclusion

In summary, efficient light generation by the MIS-type vdW heterostructure reported here is enabled by the unique properties of each layer: FLG offers a reservoir of holes; hBN serves as a quasi-vacuum layer in which high voltages can be applied to accelerate holes over a few-nanometer distance; and WS_2 serves not only as a light emitting layer but also an efficient electron transport layer in which carrier multiplication effects are expected due to strong confinement. Even though there have been results taking advantage of similar structure as ours, like the light emitting quantum well device, our devices show higher efficiency and low turn-on current density. That is because we deliberately chose the thickness of boron nitride, so that the tunneling current could be well controlled and the generated electrical field is large enough to trigger impact ionization. Carrier multiplication by impact ionization in quantum dots has generated significant interest during the past decade due to its potential application in solar energy harvesting[130]. Besides, in the F-N tunneling dominant regime, there are few electrons tunneling through the BN barrier, because the valence band offset between graphite and BN is much less than the conduction band offset between WS_2 and BN. Our results indicate that these ideas can also be applied to light emitting applications and offer prospects for realizing EL devices with >100 % efficiencies. We believe that vdW MIS diodes consisting of vdW layers are an ideal platform for the exploration of hot carrier effects and realization of unconventional photonic devices.

5 Conclusion and outlook

Throughout this thesis, we explored the potential for using 2D sheets of TMDs and their heterostructures for electronic and optoelectronic devices. Unlike convention semiconductors, some fundamental aspects of doping, charge injection and transfer are yet to be fully understood despite recent significant efforts. In chapter 2, we showed that ambient air molecules induce unintentional p-type doping in TMD nanosheets by measuring FET behaviors. We further showed that ozone molecules, which are strong oxidizing, considerably enhances P-type doping effect, resulting in significant increase of hole conductance. The reversible ozone doping reduces not only the sheet resistance but also contact resistance without degrading the intrinsic mobility of TMD FETs. We demonstrate that the observed p-type doping is due to non-covalent charge transfer between WSe_2 and the H_2O/O_3 redox couple and that water plays an essential role in the doping process. The air-stable efficient doping by ozone provides easier access to the high doping regime of WSe_2 transistor. However, the doping effect is lost when ozone molecules decompose and desorb from the TMD surface. Charge transfer by a redox couple is a highly versatile approach to inducing doping in 2D TMDs. Therefore, it is important to explore other stable oxidizing and reducing agents to achieve long-term doping. It is also crucial to demonstrate spatially selective doping to achieve p-n junctions in desired regions of 2D semiconductors.

In Chapter 3, we first studied photo-induced charge transfer in hetero-structure of MoS_2 and WSe_2 via PL spectroscopy. The quenching of PL in the

heterostack region and an emergence of a new low energy peak due to interlayer indirect transition reveals the formation of type II heterojunction, which is desirable for solar cells. Next, we turn to the heterostack of multilayers and investigated photovoltaic effects. The multilayer heterojunction exhibits “anti-ambipolar” behaviors, low current density and a power conversion efficiency of 0.0148%. We attribute the poor photovoltaic performance to large resistance of the two layers owing to low carrier density. Therefore, we propose an improved device structure by the insertion of a multilayer MoS_2 between the contact and WSe_2. The new structure demonstrates an ambipolar gate dependence and significantly enhanced I_{sc}. Both I_{sc} and V_{oc} exhibit gate and incident laser power dependence. The highest PCE of our solar cell is estimated to be around 1 % under monochromatic focused laser illumination at 532 nm. Finally, we reported on the effects of parallel shunt resistance and series resistance on the shape of IV curve and filling factors (FF). While the new device structure substantially enhanced PCE, the efficiency is strongly limited by low FF. These devices exhibit reasonable PCE but only within small gate voltage windows. For the development of practical photovoltaic devices, a robust pn junction needs to be formed without relying on external electric fields.

In Chapter 4, we report efficient light generation from a MIS-type structure by heterostacking of few-layer graphite (FLG), thin layers of hBN and monolayer WS_2. In this heterostructure, FLG plays the role of hole reservoir; the insulating hBN serves as a hole transport layer which allows only holes to pass under sufficiently large bias; and WS_2 with a direct band gap serves not only as a light emitting layer but also an efficient electron

transport. Our temperature-dependent electrical measurement demonstrates that the carriers are injected by F-N tunneling through BN. Due to the lower VBM between graphite and BN than CBM between WS_2 and BN, there are few electrons tunneling through BN. That is why the turn-on current density is very low. Our devices show higher efficiency around 13% at low temperature and high ratio between EL and PL at the same generation rate. That is because we deliberately chose the thickness of boron nitride, so that the threshold voltage and the generated electrical field are large enough to trigger impact ionization and carrier multiplication. Recently, Ali Javey's group reported PL quantum yield of monolayer TMDs could be strongly enhanced by defect passivating chemical treatment. We envision that the quantum efficiency of monolayer light emitting devices could be further enhanced by such treatment or use of high quality materials.

This thesis discussed various aspects of TMD-based electronic and opto-electronic devices. Our findings suggest that it is essential to establish robust doping schemes and growth of high quality materials for the development of practical devices. Further efforts are needed to understand the limiting factors in lateral and out-of-plane carrier conduction in these devices and optimize device performances.

6 Bibliography

1. Novoselov KS, Geim AK, Morozov SV, Jiang D, Zhang Y, Dubonos SV, *et al.* Electric Field Effect in Atomically Thin Carbon Films. *Science* 2004, **306**(5696)**:** 666-669.

2. Geim AK, Novoselov KS. The rise of graphene. *Nat Mater* 2007, **6**(3)**:** 183-191.

3. Geim AK. Graphene: Status and Prospects. *Science* 2009, **324**(5934)**:** 1530-1534.

4. Schwierz F. Graphene transistors. *Nat Nano* 2010, **5**(7)**:** 487-496.

5. Späh R, Elrod U, Lux-Steiner M, Bucher E, Wagner S. pn junctions in tungsten diselenide. *Appl Phys Lett* 1983, **43**(1)**:** 79-81.

6. Späh R, Lux-Steiner M, Obergfell M, Bucher E, Wagner S. n-MoSe2/p-WSe2 heterojunctions. *Appl Phys Lett* 1985, **47**(8)**:** 871-873.

7. Ding Y, Wang Y, Ni J, Shi L, Shi S, Tang W. First principles study of structural, vibrational and electronic properties of graphene-like MX2 (M=Mo, Nb, W, Ta; X=S, Se, Te) monolayers. *Physica B: Condensed Matter* 2011, **406**(11)**:** 2254-2260.

8. Wang QH, Kalantar-Zadeh K, Kis A, Coleman JN, Strano MS. Electronics and optoelectronics of two-dimensional transition metal dichalcogenides. *Nat Nano* 2012, **7**(11)**:** 699-712.

9. Splendiani A, Sun L, Zhang Y, Li T, Kim J, Chim C-Y, *et al.* Emerging Photoluminescence in Monolayer MoS2. *Nano letters* 2010, **10**(4)**:** 1271-1275.

10. Mak KF, Lee C, Hone J, Shan J, Heinz TF. Atomically Thin MoS_2: A New Direct-Gap Semiconductor. *Phys Rev Lett* 2010, **105**(13)**:** 136805.

11. Kuc A, Zibouche N, Heine T. Influence of quantum confinement on the electronic structure of the transition metal sulfide TS_2. *Phys Rev B* 2011, **83**(24)**:** 245213.

12. Zhang Y, Chang T-R, Zhou B, Cui Y-T, Yan H, Liu Z*, et al.* Direct observation of the transition from indirect to direct bandgap in atomically thin epitaxial MoSe2. *Nat Nano* 2014, **9**(2)**:** 111-115.

13. Zhao W, Ribeiro RM, Toh M, Carvalho A, Kloc C, Castro Neto AH*, et al.* Origin of Indirect Optical Transitions in Few-Layer MoS2, WS2, and WSe2. *Nano letters* 2013, **13**(11)**:** 5627-5634.

14. Zhao W, Ghorannevis Z, Chu L, Toh M, Kloc C, Tan P-H*, et al.* Evolution of Electronic Structure in Atomically Thin Sheets of WS2 and WSe2. *Acs Nano* 2013, **7**(1)**:** 791-797.

15. Sahin H, Tongay S, Horzum S, Fan W, Zhou J, Li J*, et al.* Anomalous Raman spectra and thickness-dependent electronic properties of WSe_2. *Phys Rev B* 2013, **87**(16)**:** 165409.

16. Lee C, Yan H, Brus LE, Heinz TF, Hone J, Ryu S. Anomalous Lattice Vibrations of Single- and Few-Layer MoS2. *Acs Nano* 2010, **4**(5)**:** 2695-2700.

17. Luo X, Zhao Y, Zhang J, Xiong Q, Quek SY. Anomalous frequency trends in MoS_2 thin films attributed to surface effects. *Phys Rev B* 2013, **88**(7)**:** 075320.

18. Ubaldini A, Jacimovic J, Ubrig N, Giannini E. Chloride-Driven Chemical Vapor Transport Method for Crystal Growth of Transition Metal Dichalcogenides. *Crystal Growth & Design* 2013, **13**(10)**:** 4453-4459.

19. Shi Y, Li H, Li L-J. Recent advances in controlled synthesis of two-dimensional transition metal dichalcogenides via vapour deposition techniques. *Chemical Society Reviews* 2015, **44**(9)**:** 2744-2756.

20. Zhan Y, Liu Z, Najmaei S, Ajayan PM, Lou J. Large-Area Vapor-Phase Growth and Characterization of MoS2 Atomic Layers on a SiO2 Substrate. *Small* 2012, **8**(7)**:** 966-971.

21. Lin Y-C, Zhang W, Huang J-K, Liu K-K, Lee Y-H, Liang C-T*, et al.* Wafer-scale MoS2 thin layers prepared by MoO3 sulfurization. *Nanoscale* 2012, **4**(20)**:** 6637-6641.

22. Song J-G, Park J, Lee W, Choi T, Jung H, Lee CW*, et al.* Layer-Controlled, Wafer-Scale, and Conformal Synthesis of Tungsten

Disulfide Nanosheets Using Atomic Layer Deposition. *Acs Nano* 2013, **7**(12)**:** 11333-11340.

23. van der Zande AM, Huang PY, Chenet DA, Berkelbach TC, You Y, Lee G-H*, et al.* Grains and grain boundaries in highly crystalline monolayer molybdenum disulphide. *Nat Mater* 2013, **12**(6)**:** 554-561.

24. Schmidt H, Wang S, Chu L, Toh M, Kumar R, Zhao W*, et al.* Transport Properties of Monolayer MoS2 Grown by Chemical Vapor Deposition. *Nano letters* 2014, **14**(4)**:** 1909-1913.

25. Lee Y-H, Zhang X-Q, Zhang W, Chang M-T, Lin C-T, Chang K-D*, et al.* Synthesis of Large-Area MoS2 Atomic Layers with Chemical Vapor Deposition. *Adv Mater* 2012, **24**(17)**:** 2320-2325.

26. Ling X, Lee Y-H, Lin Y, Fang W, Yu L, Dresselhaus MS*, et al.* Role of the Seeding Promoter in MoS2 Growth by Chemical Vapor Deposition. *Nano letters* 2014, **14**(2)**:** 464-472.

27. Okada M, Sawazaki T, Watanabe K, Taniguch T, Hibino H, Shinohara H*, et al.* Direct Chemical Vapor Deposition Growth of WS2 Atomic Layers on Hexagonal Boron Nitride. *Acs Nano* 2014, **8**(8)**:** 8273-8277.

28. Gutiérrez HR, Perea-López N, Elías AL, Berkdemir A, Wang B, Lv R*, et al.* Extraordinary Room-Temperature Photoluminescence in Triangular WS2 Monolayers. *Nano letters* 2013, **13**(8)**:** 3447-3454.

29. Wang X, Gong Y, Shi G, Chow WL, Keyshar K, Ye G*, et al.* Chemical Vapor Deposition Growth of Crystalline Monolayer MoSe2. *Acs Nano* 2014, **8**(5)**:** 5125-5131.

30. Huang J-K, Pu J, Hsu C-L, Chiu M-H, Juang Z-Y, Chang Y-H*, et al.* Large-Area Synthesis of Highly Crystalline WSe2 Monolayers and Device Applications. *Acs Nano* 2014, **8**(1)**:** 923-930.

31. Chen J, Liu B, Liu Y, Tang W, Nai CT, Li L*, et al.* Chemical Vapor Deposition of Large-Sized Hexagonal WSe2 Crystals on Dielectric Substrates. *Adv Mater* 2015, **27**(42)**:** 6722-6727.

32. Wu S, Huang C, Aivazian G, Ross JS, Cobden DH, Xu X. Vapor–Solid Growth of High Optical Quality MoS2 Monolayers with Near-Unity Valley Polarization. *Acs Nano* 2013, **7**(3)**:** 2768-2772.

33. Yoon Y, Ganapathi K, Salahuddin S. How Good Can Monolayer MoS2 Transistors Be? *Nano letters* 2011, **11**(9)**:** 3768-3773.

34. Radisavljevic B, Whitwick MB, Kis A. Integrated Circuits and Logic Operations Based on Single-Layer MoS2. *Acs Nano* 2011, **5**(12)**:** 9934-9938.

35. Wang H, Yu L, Lee Y-H, Shi Y, Hsu A, Chin ML*, et al.* Integrated Circuits Based on Bilayer MoS2 Transistors. *Nano letters* 2012, **12**(9)**:** 4674-4680.

36. Tosun M, Chuang S, Fang H, Sachid AB, Hettick M, Lin Y*, et al.* High-Gain Inverters Based on WSe2 Complementary Field-Effect Transistors. *Acs Nano* 2014, **8**(5)**:** 4948-4953.

37. Kaasbjerg K, Thygesen KS, Jacobsen KW. Phonon-limited mobility in n-type single-layer MoS${}_{2}$ from first principles. *Phys Rev B* 2012, **85**(11)**:** 115317.

38. Kim S, Konar A, Hwang W-S, Lee JH, Lee J, Yang J*, et al.* High-mobility and low-power thin-film transistors based on multilayer MoS2 crystals. *Nat Commun* 2012, **3:** 1011.

39. RadisavljevicB, RadenovicA, BrivioJ, GiacomettiV, KisA. Single-layer MoS2 transistors. *Nat Nano* 2011, **6**(3)**:** 147-150.

40. Jena D, Konar A. Enhancement of Carrier Mobility in Semiconductor Nanostructures by Dielectric Engineering. *Phys Rev Lett* 2007, **98**(13)**:** 136805.

41. Ayari A, Cobas E, Ogundadegbe O, Fuhrer MS. Realization and electrical characterization of ultrathin crystals of layered transition-metal dichalcogenides. *Journal of Applied Physics* 2007, **101**(1)**:** 014507.

42. Liu B, Ma Y, Zhang A, Chen L, Abbas AN, Liu Y*, et al.* High-Performance WSe2 Field-Effect Transistors via Controlled Formation of In-Plane Heterojunctions. *Acs Nano* 2016, **10**(5)**:** 5153-5160.

43. Cui X, Lee G-H, Kim YD, Arefe G, Huang PY, Lee C-H*, et al.* Multi-terminal transport measurements of MoS2 using a van der Waals heterostructure device platform. *Nat Nano* 2015, **10**(6)**:** 534-540.

44. Shuigang X, Zefei W, Huanhuan L, Yu H, Gen L, Xiaolong C*, et al.* Universal low-temperature Ohmic contacts for quantum transport in transition metal dichalcogenides. *2d Mater* 2016, **3**(2)**:** 021007.

45. Berkelbach TC, Hybertsen MS, Reichman DR. Theory of neutral and charged excitons in monolayer transition metal dichalcogenides. *Phys Rev B* 2013, **88**(4)**:** 045318.

46. Zeng H, Cui X. An optical spectroscopic study on two-dimensional group-VI transition metal dichalcogenides. *Chemical Society Reviews* 2015, **44**(9)**:** 2629-2642.

47. Salehzadeh O, Tran NH, Liu X, Shih I, Mi Z. Exciton Kinetics, Quantum Efficiency, and Efficiency Droop of Monolayer MoS2 Light-Emitting Devices. *Nano letters* 2014, **14**(7)**:** 4125-4130.

48. Amani M, Lien D-H, Kiriya D, Xiao J, Azcatl A, Noh J*, et al.* Near-unity photoluminescence quantum yield in MoS2. *Science* 2015, **350**(6264)**:** 1065-1068.

49. Zhang X-X, You Y, Zhao SYF, Heinz TF. Experimental Evidence for Dark Excitons in Monolayer ${\mathrm{WSe}}_{2}$. *Phys Rev Lett* 2015, **115**(25)**:** 257403.

50. Mak KF, He K, Lee C, Lee GH, Hone J, Heinz TF*, et al.* Tightly bound trions in monolayer MoS2. *Nat Mater* 2013, **12**(3)**:** 207-211.

51. Ross JS, Wu S, Yu H, Ghimire NJ, Jones AM, Aivazian G*, et al.* Electrical control of neutral and charged excitons in a monolayer semiconductor. *Nat Commun* 2013, **4:** 1474.

52. Tsai M-L, Su S-H, Chang J-K, Tsai D-S, Chen C-H, Wu C-I*, et al.* Monolayer MoS2 Heterojunction Solar Cells. *Acs Nano* 2014, **8**(8)**:** 8317-8322.

53. Hao LZ, Gao W, Liu YJ, Han ZD, Xue QZ, Guo WY*, et al.* High-performance n-MoS2/i-SiO2/p-Si heterojunction solar cells. *Nanoscale* 2015, **7**(18)**:** 8304-8308.

54. Kang J, Tongay S, Zhou J, Li J, Wu J. Band offsets and heterostructures of two-dimensional semiconductors. *Appl Phys Lett* 2013, **102**(1)**:** 012111.

55. Chiu M-H, Zhang C, Shiu H-W, Chuu C-P, Chen C-H, Chang C-YS*, et al.* Determination of band alignment in the single-layer MoS2/WSe2 heterojunction. *Nat Commun* 2015, **6**.

56. Tongay S, Fan W, Kang J, Park J, Koldemir U, Suh J*, et al.* Tuning Interlayer Coupling in Large-Area Heterostructures with CVD-Grown MoS2 and WS2 Monolayers. *Nano letters* 2014, **14**(6)**:** 3185-3190.

57. Hong X, Kim J, Shi S-F, Zhang Y, Jin C, Sun Y*, et al.* Ultrafast charge transfer in atomically thin MoS2/WS2 heterostructures. *Nat Nano* 2014, **9**(9)**:** 682-686.

58. Fang H, Battaglia C, Carraro C, Nemsak S, Ozdol B, Kang JS*, et al.* Strong interlayer coupling in van der Waals heterostructures built from single-layer chalcogenides. *Proceedings of the National Academy of Sciences* 2014, **111**(17)**:** 6198-6202.

59. Ceballos F, Bellus MZ, Chiu H-Y, Zhao H. Ultrafast Charge Separation and Indirect Exciton Formation in a MoS2–MoSe2 van der Waals Heterostructure. *Acs Nano* 2014, **8**(12)**:** 12717-12724.

60. Lee C-H, Lee G-H, van der Zande AM, Chen W, Li Y, Han M*, et al.* Atomically thin p–n junctions with van der Waals heterointerfaces. *Nat Nano* 2014, **9**(9)**:** 676-681.

61. Furchi MM, Pospischil A, Libisch F, Burgdörfer J, Mueller T. Photovoltaic Effect in an Electrically Tunable van der Waals Heterojunction. *Nano letters* 2014, **14**(8)**:** 4785-4791.

62. Cheng R, Li D, Zhou H, Wang C, Yin A, Jiang S*, et al.* Electroluminescence and Photocurrent Generation from Atomically Sharp WSe2/MoS2 Heterojunction p–n Diodes. *Nano letters* 2014, **14**(10)**:** 5590-5597.

63. Roy T, Tosun M, Cao X, Fang H, Lien D-H, Zhao P*, et al.* Dual-Gated MoS2/WSe2 van der Waals Tunnel Diodes and Transistors. *Acs Nano* 2015, **9**(2)**:** 2071-2079.

64. Roy T, Tosun M, Kang JS, Sachid AB, Desai SB, Hettick M*, et al.* Field-Effect Transistors Built from All Two-Dimensional Material Components. *Acs Nano* 2014, **8**(6)**:** 6259-6264.

65. Lee G-H, Yu Y-J, Cui X, Petrone N, Lee C-H, Choi MS*, et al.* Flexible and Transparent MoS2 Field-Effect Transistors on Hexagonal Boron Nitride-Graphene Heterostructures. *Acs Nano* 2013, **7**(9)**:** 7931-7936.

66. Sundaram RS, Engel M, Lombardo A, Krupke R, Ferrari AC, Avouris P*, et al.* Electroluminescence in Single Layer MoS2. *Nano letters* 2013, **13**(4)**:** 1416-1421.

67. Avouris P, Freitag M, Perebeinos V. Carbon-nanotube photonics and optoelectronics. *Nat Photon* 2008, **2**(6)**:** 341-350.

68. Lopez-Sanchez O, Alarcon Llado E, Koman V, Fontcuberta i Morral A, Radenovic A, Kis A. Light Generation and Harvesting in a van der Waals Heterostructure. *Acs Nano* 2014, **8**(3)**:** 3042-3048.

69. Ovchinnikov D, Allain A, Huang Y-S, Dumcenco D, Kis A. Electrical Transport Properties of Single-Layer WS2. *Acs Nano* 2014, **8**(8)**:** 8174-8181.

70. Chuang H-J, Tan X, Ghimire NJ, Perera MM, Chamlagain B, Cheng MM-C*, et al.* High Mobility WSe2 p- and n-Type Field-Effect Transistors Contacted by Highly Doped Graphene for Low-Resistance Contacts. *Nano letters* 2014, **14**(6)**:** 3594-3601.

71. Jo S, Ubrig N, Berger H, Kuzmenko AB, Morpurgo AF. Mono- and Bilayer WS2 Light-Emitting Transistors. *Nano letters* 2014, **14**(4)**:** 2019-2025.

72. Ross JS, Klement P, Jones AM, Ghimire NJ, Yan J, Mandrus DG*, et al.* Electrically tunable excitonic light-emitting diodes based on monolayer WSe2 p-n junctions. *Nat Nano* 2014, **9**(4)**:** 268-272.

73. Withers F, Del Pozo-Zamudio O, Mishchenko A, Rooney AP, Gholinia A, Watanabe K*, et al.* Light-emitting diodes by band-structure engineering in van der Waals heterostructures. *Nat Mater* 2015, **14**(3)**:** 301-306.

74. Baugher BW, Churchill HO, Yang Y, Jarillo-Herrero P. Intrinsic electronic transport properties of high-quality monolayer and bilayer MoS2. *Nano letters* 2013, **13**(9)**:** 4212-4216.

75. Fang H, Chuang S, Chang TC, Takei K, Takahashi T, Javey A. High-Performance Single Layered WSe2 p-FETs with Chemically Doped Contacts. *Nano letters* 2012, **12**(7)**:** 3788-3792.

76. Liu W, Kang J, Sarkar D, Khatami Y, Jena D, Banerjee K. Role of metal contacts in designing high-performance monolayer n-type WSe2 field effect transistors. *Nano letters* 2013, **13**(5)**:** 1983-1990.

77. Li SS, Wang SF, Tang DM, Zhao WJ, Xu HL, Chu LQ*, et al.* Halide-Assisted Atmospheric Pressure Growth of Large WSe2 and WS2 Monolayer Crystals. *Appl Mater Today* 2015, **1**(1)**:** 60-66.

78. Liu H, Neal AT, Ye PDD. Channel Length Scaling of MoS2 MOSFETs. *Acs Nano* 2012, **6**(10)**:** 8563-8569.

79. Pu J, Yomogida Y, Liu KK, Li LJ, Iwasa Y, Takenobu T. Highly Flexible MoS2 Thin-Film Transistors with Ion Gel Dielectrics. *Nano letters* 2012, **12**(8)**:** 4013-4017.

80. Dolui K, Rungger I, Das Pemmaraju C, Sanvito S. Possible doping strategies for MoS2 monolayers: An ab initio study. *Phys Rev B* 2013, **88**(7).

81. Suh J, Park TE, Lin DY, Fu DY, Park J, Jung HJ*, et al.* Doping against the Native Propensity of MoS2: Degenerate Hole Doping by Cation Substitution. *Nano letters* 2014, **14**(12)**:** 6976-6982.

82. Zhao PD, Kiriya D, Azcatl A, Zhang CX, Tosun M, Liu YS*, et al.* Air Stable p-Doping of WSe2 by Covalent Functionalization. *Acs Nano* 2014, **8**(10)**:** 10808-10814.

83. Schmidt H, Giustiniano F, Eda G. Electronic transport properties of transition metal dichalcogenide field-effect devices: surface and interface effects. *Chemical Society Reviews* 2015.

84. Liu B, Chen L, Liu G, Abbas AN, Fathi M, Zhou C. High-performance chemical sensing using Schottky-contacted chemical vapor deposition grown monolayer MoS2 transistors. *Acs Nano* 2014, **8**(5)**:** 5304-5314.

85. Cho B, Hahm MG, Choi M, Yoon J, Kim AR, Lee YJ*, et al.* Charge-transfer-based Gas Sensing Using Atomic-layer MoS2. *Sci Rep-Uk* 2015, **5**.

86. Chuang S, Battaglia C, Azcatl A, McDonnell S, Kang JS, Yin XT*, et al.* MoS2 P-type Transistors and Diodes Enabled by High Work Function MoOx Contacts. *Nano letters* 2014, **14**(3)**:** 1337-1342.

87. Han C, Lin JD, Xiang D, Wang CC, Wang L, Chen W. Improving chemical vapor deposition graphene conductivity using molybdenum trioxide: An in-situ field effect transistor study. *Appl Phys Lett* 2013, **103**(26).

88. Levesque PL, Sabri SS, Aguirre CM, Guillemette J, Siaj M, Desjardins P*, et al.* Probing Charge Transfer at Surfaces Using Graphene Transistors. *Nano letters* 2011, **11**(1)**:** 132-137.

89. Aguirre CM, Levesque PL, Paillet M, Lapointe F, St-Antoine BC, Desjardins P*, et al.* The Role of the Oxygen/Water Redox Couple in Suppressing Electron Conduction in Field-Effect Transistors. *Adv Mater* 2009, **21**(30)**:** 3087-+.

90. Jones AM, Yu HY, Ghimire NJ, Wu SF, Aivazian G, Ross JS*, et al.* Optical generation of excitonic valley coherence in monolayer WSe2. *Nat Nanotechnol* 2013, **8**(9)**:** 634-638.

91. Schmidt H, Wang SF, Chu LQ, Toh M, Kumar R, Zhao WJ*, et al.* Transport Properties of Monolayer MoS2 Grown by Chemical Vapor Deposition. *Nano letters* 2014, **14**(4)**:** 1909-1913.

92. Das S, Chen HY, Penumatcha AV, Appenzeller J. High Performance Multilayer MoS2 Transistors with Scandium Contacts. *Nano letters* 2013, **13**(1)**:** 100-105.

93. Hu C. *Modern semiconductor devices for integrated circuits*. Prentice Hall: Upper Saddle River, N.J., 2010.

94. Yamamoto M, Dutta S, Aikawa S, Nakaharai S, Wakabayashi K, Fuhrer MS*, et al.* Self-Limiting Layer-by-Layer Oxidation of Atomically Thin WSe2. *Nano letters* 2015, **15**(3)**:** 2067-2073.

95. Qiu H, Pan LJ, Yao ZN, Li JJ, Shi Y, Wang XR. Electrical characterization of back-gated bi-layer MoS2 field-effect transistors and the effect of ambient on their performances. *Appl Phys Lett* 2012, **100**(12).

96. Kang J, Tongay S, Zhou J, Li JB, Wu JQ. Band offsets and heterostructures of two-dimensional semiconductors. *Appl Phys Lett* 2013, **102**(1).

97. Lopez-Sanchez O, Lembke D, Kayci M, Radenovic A, Kis A. Ultrasensitive photodetectors based on monolayer MoS2. *Nat Nano* 2013, **8**(7)**:** 497-501.

98. Yin Z, Li H, Li H, Jiang L, Shi Y, Sun Y*, et al.* Single-Layer MoS2 Phototransistors. *Acs Nano* 2012, **6**(1)**:** 74-80.

99. Choi W, Cho MY, Konar A, Lee JH, Cha G-B, Hong SC*, et al.* High-Detectivity Multilayer MoS2 Phototransistors with Spectral Response from Ultraviolet to Infrared. *Adv Mater* 2012, **24**(43)**:** 5832-5836.

100. Zhang W, Huang J-K, Chen C-H, Chang Y-H, Cheng Y-J, Li L-J. High-Gain Phototransistors Based on a CVD MoS2 Monolayer. *Adv Mater* 2013, **25**(25)**:** 3456-3461.

101. Pospischil A, Furchi MM, Mueller T. Solar-energy conversion and light emission in an atomic monolayer p-n diode. *Nat Nano* 2014, **9**(4)**:** 257-261.

102. Chegaar M, Azzouzi G, Mialhe P. Simple parameter extraction method for illuminated solar cells. *Solid-State Electronics* 2006, **50**(7–8)**:** 1234-1237.

103. Singh A, Moody G, Wu S, Wu Y, Ghimire NJ, Yan J*, et al.* Coherent Electronic Coupling in Atomically Thin MoSe2. *Phys Rev Lett* 2014, **112**(21)**:** 216804.

104. Jones AM, Yu H, Ghimire NJ, Wu S, Aivazian G, Ross JS*, et al.* Optical generation of excitonic valley coherence in monolayer WSe_2. *Nat Nano* 2013, **8**(9)**:** 634-638.

105. Mak KF, He K, Lee C, Lee GH, Hone J, Heinz TF*, et al.* Tightly bound trions in monolayer MoS_2. *Nat Mater* 2013, **12**(3)**:** 207-211.

106. He K, Kumar N, Zhao L, Wang Z, Mak KF, Zhao H*, et al.* Tightly bound excitons in monolayer WSe2. *Phys Rev Lett* 2014, **113**(2)**:** 026803.

107. Ugeda MM, Bradley AJ, Shi SF, da Jornada FH, Zhang Y, Qiu DY*, et al.* Giant bandgap renormalization and excitonic effects in a monolayer transition metal dichalcogenide semiconductor. *Nat Mater* 2014, **13**(12)**:** 1091-1095.

108. Liu X, Galfsky T, Sun Z, Xia F, Lin E-c, Lee Y-H*, et al.* Strong light–matter coupling in two-dimensional atomic crystals. *Nat Photon* 2015, **9**(1)**:** 30-34.

109. Dufferwiel S, Schwarz S, Withers F, Trichet AAP, Li F, Sich M*, et al.* Exciton-polaritons in van der Waals heterostructures embedded in tunable microcavities. *Nat Commun* 2015, **6**.

110. Fogler MM, Butov LV, Novoselov KS. High-temperature superfluidity with indirect excitons in van der Waals heterostructures. *Nat Commun* 2014, **5**.

111. Jo S, Ubrig N, Berger H, Kuzmenko AB, Morpurgo AF. Mono- and bilayer WS_2 light-emitting transistors. *Nano letters* 2014, **14**(4)**:** 2019-2025.

112. Ye Y, Xiao J, Wang H, Ye Z, Zhu H, Zhao M*, et al.* Electrical generation and control of the valley carriers in a monolayer transition metal dichalcogenide. *Nat Nano* 2016, **advance online publication**.

113. Sundaram RS, Engel M, Lombardo A, Krupke R, Ferrari AC, Avouris P*, et al.* Electroluminescence in single layer MoS_2. *Nano letters* 2013, **13**(4)**:** 1416-1421.

114. Cheng R, Li D, Zhou H, Wang C, Yin A, Jiang S*, et al.* Electroluminescence and photocurrent generation from atomically sharp WSe_2/MoS_2 heterojunction p-n diodes. *Nano letters* 2014, **14**(10)**:** 5590-5597.

115. Zhang YJ, Oka T, Suzuki R, Ye JT, Iwasa Y. Electrically switchable chiral light-emitting transistor. *Science* 2014, **344**(6185)**:** 725-728.

116. Huang C, Wu S, Sanchez AM, Peters JJP, Beanland R, Ross JS*, et al.* Lateral heterojunctions within monolayer $MoSe_2$–WSe_2 semiconductors. *Nat Mater* 2014, **13**(12)**:** 1096-1101.

117. Mak KF, Lee C, Hone J, Shan J, Heinz TF. Atomically thin MoS2: a new direct-gap semiconductor. *Phys Rev Lett* 2010, **105**(13)**:** 136805.

118. Wang L, Meric I, Huang PY, Gao Q, Gao Y, Tran H*, et al.* One-dimensional electrical contact to a two-dimensional material. *Science* 2013, **342**(6158)**:** 614-617.

119. Withers F, Del Pozo-Zamudio O, Schwarz S, Dufferwiel S, Walker P, Godde T, *et al.* WSe_2 light-emitting tunneling transistors with enhanced brightness at room temperature. *Nano letters* 2015, **15**(12)**:** 8223-8228.

120. Kubin RF, Fletcher AN. Fluorescence quantum yields of some rhodamine dyes. *Journal of Luminescence* 1983, **27**(4)**:** 455-462.

121. Wakamiya A, Mori K, Yamaguchi S. 3-Boryl-2, 2′-bithiophene as a Versatile Core Skeleton for Full-Color Highly Emissive Organic Solids. *Angewandte Chemie International Edition* 2007, **46**(23)**:** 4273-4276.

122. Amani M, Taheri P, Addou R, Ahn GH, Kiriya D, Lien D-H*, et al.* Recombination Kinetics and Effects of Superacid Treatment in Sulfur- and Selenium-Based Transition Metal Dichalcogenides. *Nano letters* 2016, **16**(4)**:** 2786-2791.

123. Lien D-H, Kang JS, Amani M, Chen K, Tosun M, Wang H-P*, et al.* Engineering Light Outcoupling in 2D Materials. *Nano letters* 2015, **15**(2)**:** 1356-1361.

124. Wang H, Zhang C, Rana F. Ultrafast dynamics of defect-assisted electron-hole recombination in monolayer MoS_2. *Nano letters* 2015, **15**(1)**:** 339-345.

125. Kozawa D, Kumar R, Carvalho A, Kumar Amara K, Zhao W, Wang S, *et al.* Photocarrier relaxation pathway in two-dimensional semiconducting transition metal dichalcogenides. *Nat Commun* 2014, **5:** 4543.

126. Fowler RH, Nordheim L. Electron emission in intense electric fields. Proceedings of the Royal Society of London A: Mathematical, Physical and Engineering Sciences; 1928: The Royal Society; 1928. p. 173-181.

127. Chernikov A, Berkelbach TC, Hill HM, Rigosi A, Li Y, Aslan OB*, et al.* Exciton binding energy and nonhydrogenic Rydberg series in monolayer WS2. *Phys Rev Lett* 2014, **113**(7)**:** 076802.

128. Snow ES, Kirchoefer SW, Campbell PM, Glembocki OJ. Efficient light emission by impact ionization in single-barrier tunneling devices. *Appl Phys Lett* 1989, **54**(21)**:** 2124-2126.

129. Jaklevic RC, Donald DK, Lambe J, Vassell WC. Injection electroluminescence in CdS by tunneling films. *Appl Phys Lett* 1963, **2**(1)**:** 7-9.

130. Nozik AJ, Beard MC, Luther JM, Law M, Ellingson RJ, Johnson JC. Semiconductor Quantum Dots and Quantum Dot Arrays and Applications of Multiple Exciton Generation to Third-Generation Photovoltaic Solar Cells. *Chemical Reviews* 2010, **110**(11)**:** 6873-6890.